

International Journal of Antennas and Propagation

New Electromagnetic Methods and Applications of Antennas in Biomedicine

Guest Editors: Tamer S. Ibrahim, Stuart Crozier, and Elise Fear





New Electromagnetic Methods and Applications of Antennas in Biomedicine

International Journal of Antennas and Propagation

**New Electromagnetic Methods
and Applications of Antennas in
Biomedicine**

Guest Editors: Tamer S. Ibrahim, Stuart Crozier,
and Elise Fear



Copyright © 2008 Hindawi Publishing Corporation. All rights reserved.

This is a special issue published in volume 2008 of “International Journal of Antennas and Propagation.” All articles are open access articles distributed under the Creative Commons Attribution License, which permits unrestricted use, distribution, and reproduction in any medium, provided the original work is properly cited.

Editor-in-Chief

Cynthia Furse, University of Utah, USA

Advisory Editors

Constantine A. Balanis, USA
Magdy Iskander, USA

Tatsuo Itoh, USA

Raj Mittra, USA

Associate Editors

Makoto Ando, Japan
James Becker, USA
Charles Bunting, USA
Deb Chatterjee, USA
You Chung Chung, Korea
Karu Esselle, Australia
Miguel Ferrando, Spain
Dejan Filipovic, USA
Lance Griffiths, USA

Tamer S. Ibrahim, USA
Randy Jost, USA
Branko Kolundzija, Serbia
Joshua Le-Wei Li, Singapore
J. S. Mandeep, Malaysia
Hisashi Morishita, Japan
J. Nadobny, Germany
Pavel Nikitin, USA
A. Panagopoulos, Greece

Magdalena Salazar-Palma, Spain
Hans G. Schantz, USA
Stefano Selleri, Italy
Krishnasamy T. Selvan, Malaysia
Levent Sevgi, Turkey
Seong-Youp Suh, USA
Manos M. Tentzeris, USA
Vasundara V. Varadan, USA
Parveen Wahid, USA

Contents

New Electromagnetic Methods and Applications of Antennas in Biomedicine,

Tamer Ibrahim, Elise Fear, and Stuart Crozier

Volume 2008, Article ID 170242, 1 page

Microwave Tomography for Brain Imaging: Feasibility Assessment for Stroke Detection,

Serguei Y. Semenov and Douglas R. Corfield

Volume 2008, Article ID 254830, 8 pages

Improved Delay-and-Sum Beamforming Algorithm for Breast Cancer Detection,

M. Klemm, I. J. Craddock, J. A. Leendertz, A. Preece, and R. Benjamin

Volume 2008, Article ID 761402, 9 pages

Determination of Bolus Dielectric Constant for Optimum Coupling of Microwaves through Skin for Breast Cancer Imaging, Carey Rappaport

Volume 2008, Article ID 359582, 5 pages

Characterization of an Implicitly Resistively-Loaded Monopole Antenna in Lossy Liquid Media,

Colleen J. Fox, Paul M. Meaney, Fridon Shubitidze, Lincoln Potwin, and Keith D. Paulsen

Volume 2008, Article ID 580782, 9 pages

Directive Antenna for Ultrawideband Medical Imaging Systems, Amin M. Abbosh

Volume 2008, Article ID 854012, 6 pages

A 31.5 GHz Patch Antenna Design for Medical Implants, Yasir Ahmed, Yang Hao, and Clive Parini

Volume 2008, Article ID 167980, 6 pages

An Antenna-Theory Method for Modeling High-Frequency RF Coils: A Segmented Birdcage Example, Xin Chen, Victor Taracila, Timothy Eagan, Hiroyuki Fujita, Xingxian Shou,

Tanvir Baig, and Robert Brown

Volume 2008, Article ID 456019, 10 pages

Parallel Solvers for Finite-Difference Modeling of Large-Scale, High-Resolution Electromagnetic Problems in MRI, Hua Wang, Adnan Trakic, Feng Liu, Bing Keong Li, Ewald Weber, and Stuart Crozier

Volume 2008, Article ID 259703, 12 pages

Assessment of a PML Boundary Condition for Simulating an MRI Radio Frequency Coil,

Yunsuo Duan, Tamer S. Ibrahim, Bradley S. Peterson, Feng Liu, and Alayar Kangarlu

Volume 2008, Article ID 563196, 10 pages

Editorial

New Electromagnetic Methods and Applications of Antennas in Biomedicine

Tamer Ibrahim,¹ Elise Fear,² and Stuart Crozier³

¹ *Departments of Radiology and Bioengineering, University of Pittsburgh, Pittsburgh, PA 15213, USA*

² *Department of Electrical Engineering, Schulich School of Engineering, University of Calgary, AB, Canada T2N1N4*

³ *Department of Mathematics, The University of Queensland, Queensland 4072, Australia*

Correspondence should be addressed to Tamer Ibrahim, tsi2@pitt.edu

Received 16 July 2008; Accepted 16 July 2008

Copyright © 2008 Tamer Ibrahim et al. This is an open access article distributed under the Creative Commons Attribution License, which permits unrestricted use, distribution, and reproduction in any medium, provided the original work is properly cited.

Electromagnetic devices and techniques are of increasing interest and clinical utility in a variety of medical applications. Hyperthermia may be utilized to heat tissues using electromagnetic fields as part of cancer treatment. Many clinically available and emerging imaging techniques have also relied on electromagnetic concepts. Tissue-implanted devices wirelessly communicate information from the interior to the exterior of the body and vice versa. Developing and optimizing use of these technologies involves a sophisticated understanding of the interactions between electromagnetic fields and tissues. This encompasses the theoretical, computational, and experimental challenges. This Special Issue on New Electromagnetic Methods and Applications of Antennas in Biomedicine is devoted to reporting the latest research in this growing interdisciplinary field.

In this issue, the first two papers explore approaches to imaging at microwave frequencies for two different applications: stroke and breast cancer detection. The third paper examines a practical issue for breast imaging, namely, selection of an appropriate medium to immerse the antennas and breast. A study of antenna performance in immersion media is presented in the fourth paper in order to better understand issues such as variations in antenna response with immersion depth. The fifth paper presents a design for ultra-wideband antennas for microwave imaging, and analyzes the performances of these antennas in a realistic scenario. The sixth paper shifts the focus of the issue from imaging to tissue-implanted antennas. In the next three papers, the focus is shifted to magnetic resonance imaging (MRI). Antenna theory is applied to design a radiofrequency

(RF) coil for high-field MRI applications in the seventh paper. The final two papers report on electromagnetic simulation methods used in MRI. Overall, the papers in this issue represent a broad spectrum of work in new electromagnetic methods and applications of antennas in biomedicine.

We would like to thank many people whose efforts made this special issue possible. First, we thank the authors for their response to our initial call for papers. Second, we thank the team at IJAP for their ongoing support. Finally, we would like to acknowledge the significant contributions of the reviewers who provided feedback on multiple versions of the papers.

*Tamer Ibrahim
Elise Fear
Stuart Crozier*

Research Article

Microwave Tomography for Brain Imaging: Feasibility Assessment for Stroke Detection

Serguei Y. Semenov and Douglas R. Corfield

*School of Medicine, Keele University, ISTM, Hartshill Campus, Thornburrow Drive, Hartshill,
Stoke-on-Trent ST4 7QB, UK*

Correspondence should be addressed to Serguei Y. Semenov, s.semenov@pmed.keele.ac.uk

Received 28 September 2007; Accepted 12 March 2008

Recommended by Stuart Crozier

There is a need for a medical imaging technology, that supplements current clinical brain imaging techniques, for the near-patient and mobile assessment of cerebral vascular disease. Microwave tomography (MWT) is a novel imaging modality that has this potential. The aim of the study was to assess the feasibility, and potential performance characteristics, of MWT for brain imaging with particular focus on stroke detection. The study was conducted using MWT computer simulations and 2D head model with stroke. A nonlinear Newton reconstruction approach was used. The MWT imaging of deep brain tissues presents a significant challenge, as the brain is an object of interest that is located inside a high dielectric contrast shield, comprising the skull and CSF. However, high performance, nonlinear MWT inversion methods produced biologically meaningful images of the brain including images of stroke. It is suggested that multifrequency MWT has the potential to significantly improve imaging results.

Copyright © 2008 S. Y. Semenov and D. R. Corfield. This is an open access article distributed under the Creative Commons Attribution License, which permits unrestricted use, distribution, and reproduction in any medium, provided the original work is properly cited.

1. INTRODUCTION

A healthy brain requires an adequate blood supply. A stroke or “brain attack” compromises cerebral blood flow (CBF) leading to brain injury. This brain injury can lead to death or permanent loss of function and disability. Approximately 700 000 people, each year, will experience a stroke in the US; in 2004, stroke accounted for 1 in every 16 US deaths [1].

The brain is particularly vulnerable to disturbances in blood flow as it contains no endogenous stores of energy; it is dependent upon a continuous and sufficient level of blood flow for the constant replenishment of oxygen and glucose and for the removal of waste products. Therefore, CBF is tightly regulated to meet the brain’s metabolic needs; local changes in cerebral metabolism are associated with local changes in CBF. Indeed this close coupling of metabolism and flow is the basis for functional brain imaging techniques such as $H_2^{15}O$ positron emission tomography (PET) and blood oxygen level dependent functional magnetic resonance imaging (fMRI). In addition to the metabolic coupling of CBF to metabolism, an intrinsic autoregulatory mechanism maintains a constant level of blood flow despite fluctua-

tions in arterial blood pressure across a wide physiological ranges; this protects the cerebral circulation from potentially harmful changes in perfusion pressure. Thus, the normal regulation of cerebral perfusion depends on a complex interaction of metabolism, circulation, and respiration which is perturbed by pathologies such as stroke.

Acute ischemic strokes account for about 85% of all strokes; each begins with a blood clot (thrombus) forming in the circulation at a site distant from the brain. The clot breaks away from this distant site forming an embolus which then travels through the circulation; on reaching the brain, the embolus lodges in the small vessels interrupting blood flow to a portion of brain tissue. With this reduction in blood flow, tissue damage quickly ensues. Clinical management of stroke has been enhanced by the use of thrombolytics (clot busters) combined with the application of brain imaging techniques that reveal the pathophysiological changes in brain tissue that result from the stroke. In particular, the clinical decision, to use a thrombolytic, must be made within 3 hours of the onset of symptoms and requires a firm diagnosis of an ischemic stroke [2]. This clinical decision relies on imaging methods such as computed

tomography (CT) and MRI to reliably determine ischemic perfusion changes. Subsequent management of the stroke is enhanced by imaging the extent of the area of brain tissue with compromised blood flow [3]. Current clinical imaging methods, including CT, PET, and MRI each offers useful information on tissue properties related to perfusion, ischemia, and infarction [3]. Whilst each of these methods has its own advantages, none currently offers a rapid or cost effective imaging solution that can be made widely available at the “bedside” in the emergency department or to first response paramedical services. Microwave tomography (MWT) might present a safe, portable, and cost-effective supplement to current imaging modalities for acute and chronic assessment of cerebral vascular diseases including stroke.

With microwave imaging, tissues are imaged based on differences in their dielectric properties. It has been demonstrated that tissue malignancies, blood supply, hypoxia, acute ischemia, and chronic infarction [4–9] change tissue dielectric properties. Therefore, MW imaging offers the potential for the diagnosis of functional and pathological tissue conditions, including perfusion and perfusion-related injuries. MW imaging of breast malignancies has been demonstrated [8, 10–12]. Perfusion-related tissue injuries have been imaged using MWT in excised canine hearts [13] and in simulated extremities [9]. MWT of biological objects possesses very complicated problem of so-called diffraction tomography [14]. A high dielectric contrast between tissues with high water content (e.g., muscle tissue) and low water content (e.g., bone) presents an additional complication for MWT imaging. Various approaches in two-dimensional (2D) and three-dimensional (3D) geometries, using scalar and vector approximations, have been developed recently [15–25]. We have shown that experimental MWT imaging of high dielectric contrast objects is possible using nonlinear Newton and multiplicative regularised contrast source inversion (MR-CSI) methods [24]. MWT imaging of the brain presents a significant challenge, as the brain is an object of interest that is located inside a high dielectric contrast shield, comprising the skull (with low dielectric contrast ($\epsilon \sim 10\text{--}15$) and cerebral spinal fluid (with high $\epsilon \sim 55\text{--}60$). The aims of this project are: (i) to determine the optimal technical characteristics of an MWT brain imaging device and (ii) to assess the feasibility and potential performance characteristics of MWT for brain imaging with a particular focus on stroke detection. The methods and modeling approaches are described in Section 2; the results are presented and discussed in Section 3.

2. METHODS

The aims of the study were accomplished using computer simulations of MWT imaging of a 2D head model. The model is presented in Figure 1. The dielectric properties of the regions of normal head model, taken from published data [26–29], are summarised in Table 1. In further developing this model, to incorporate a region of acutely simulated stroke injury, we used previously obtained tissue perfusion data [4, 5, 9]. The acute stroke injury was simulated as -10

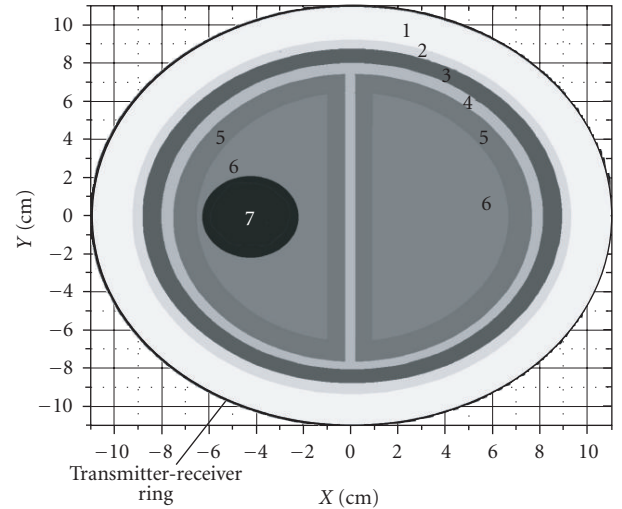


FIGURE 1: Simulated 2D model of a head inside of the MWT imaging chamber with a radius of 11 cm.

contrast (to white matter) circle with diameter 1, 2, or 4 cm. Further simulations were conducted using two 2D models of a head, first, with normal brain blood flow and, second, with compromised blood flow due to simulated stroke (see Figure 1).

Transmitters and receivers (positioned equidistantly) were located on the outer ring of the working chamber with a radius of 11 cm. The overall number of transmitters (N_{tr}) and receivers (N_{rec}) was 32×32 or 64×64 . In general cases, the more sources/receivers that are used, the better quality of reconstructed images is expected. However, an increased number of antennas will add additional technical obstacles, such as an increase of data acquisition time, problem related to the construction of small, efficient antennas for 0.5–2.0 GHz, and so forth. See discussion following Table 3 for further details. To simulate an MWT imaging procedure, the object under the study was irradiated from j th transmitter and scattered electromagnetic (EM) field was measured on $N_{rec}/2$ opposite receivers. This was continued for each transmitter from 1 to N_{tr} . In some series of simulations, a random noise was added to received complex EM signal. The sources of EM radiation were simulated as unlimited strings over the main axis (z -axis) of the 2D model. Of course, this source model together with an overall 2D approach has limited practical application. However, the model does allow assessing the feasibility of the technology. In practical cases, we proved that a dipole model is a good approximation of ceramic loaded waveguide antennas used in our previously built systems [30–32]. The direct problem was solved on a polar grid system with uniform mesh (512 over angle \times 256 over radius) using an approach presented elsewhere [15].

Image reconstruction was performed using the Newton approach, presented elsewhere [15]. Within this approach, we used a polar mesh with 256 (angle) \times 128 (radius) grids for solution of the direct problem and a Cartesian mesh with 64×64 grids for inverse problem, with various regularisation parameters. Regularisation parameters were

TABLE 1: Dielectric properties of the head model at 1 GHz (see Figure 1).

Region Thickness	Matching solution	Skin 5 mm	Skull 7 mm	CSF 3 mm	Grey matter	White matter	Stroke area
No.	1	2	3	4	5	6	7
Dielectric properties	$40 + j13$	$40 + j11$	$13 + j2$	$57 + j26$	$50 + j18$	$40 + j15$	$36 + j13$

TABLE 2: Projected signal attenuation within tomographic imaging procedure of human head.

Frequency [GHz]	0.5	1.0	2.0
Attenuation [dB]	-58	-100	-156

chosen by a trial method. Two reconstruction schemes were used: single frequency and multi (dual)-frequencies. Within single frequency schemes, the image reconstruction was started with a homogeneous background medium of matching solution, therefore, no a priori information taken into account. Within the multifrequency schemes there was a sequential chain of reconstructions at each frequency. An initial reconstruction was started from a homogeneous background medium using scattered EM fields obtained at the 1st frequency, while, at the sequential step(s) we used different frequencies (with corresponding scattered EM fields obtained at that frequencies) and started from the results of reconstruction obtained at previous step(s). This procedure was performed using different frequencies from 0.5 GHz to 2.0 GHz. At this stage, the frequency dispersion of dielectric properties of the various tissues was not taken into account. The potential impact of this assumption is discussed in the next section.

3. RESULTS AND DISCUSSION

The technical performance of MWT brain imaging approach was initially assessed over a frequency range from 0.5 GHz to 2.5 GHz using the model and direct problem solver. The ultimate goal is to develop microwave tomographic technology with the best sensitivity and specificity, and with high temporal and spatial resolution, for the noninvasive assessment of brain tissues. The best spatial resolution can be achieved at high frequencies. However, the attenuation of EM radiation in biological media is in inverse ratio with the frequency, with decreasing signal-to-noise ratio (SNR) at high frequencies. Therefore, the strategy is to find the highest possible frequency at which receivers will still be able to detect signal with reliable SNR and will not compromise temporal resolution. Using our MWT simulation approach, together with the model of the head (see Figure 1), we estimated an overall signal attenuation summarised in Table 2. The results should be taken as a guidance or initial estimation, which does not take into account dispersion of tissue dielectric properties, any particulars of head geometry, and so forth.

As can be seen, the attenuation is very high at frequencies above 1 GHz-2 GHz range. As it is highly desirable: (i) to

achieve a good SNR ratio (within a range of 40–60 dB) for biological detection reasons, such as sensitivity, specificity, and resolution and (ii) to not increase data acquisition time for measuring highly attenuated signals, which compromises an expected very attractive time resolution (within msec range) in order to detect circulated gated tissue changes, we suggest that frequencies within 0.5 to 1.0 GHz might be an optimal for brain imaging. An additional expected advantage, of using this low portion of microwave spectrum, is that acute perfusion related changes in tissue dielectric properties are more pronounced at low frequencies [4, 5]. This choice might unfavorably affect spatial resolution in its classical, far-EM-field sense. However, there is potential to improve spatial resolution, even to obtain a super-resolution in near-EM-field using nonlinear inversion [33, 34].

We further assessed the potential resolution of the technology to detect acute “stroke-like” areas with –10% contrast in dielectric properties. It has to be noted here that this is different from the classical spatial resolution definition, which is defined as a minimal distance (using Raleigh or half-height criteria) at which two small similar inhomogeneities can be distinguished between each other. Previously, we conducted such studies and experimentally achieved a 7–9 mm spatial resolution at 0.9 GHz [35]. In this study, the aim was to understand what was the smallest size of brain inhomogeneity, with a particular dielectric contrast, that could potentially be detected. In our previous MWT imaging studies, we suggested that changes in about 1% in amplitude and about 1 degree in phase of the received EM signal could be confidently detected and corresponding alterations in dielectric properties could be successfully reconstructed. We simulated MWT data acquisition for brain models with and without stroke areas of different size and then averaged differences in received EM signals over all receivers for each of transmitter position. The averaged differences in EM signals at 1 GHz for normal brain, and brain with stroke, were about: 3.8% in amplitude and 5.5° in phase for 4 cm diameter stroke, 1.2% and 2° for 2 cm and 0.3% and 0.2° for 1 cm correspondingly. Therefore, it is suggested that, at this level of the development of MWT imaging technology, the smallest imaginable area of acute stroke is estimated to be about 2 cm in diameter. This resolution might not compare with the one achieved by other imaging modalities, such as MRI or CT. However, all performance factors should be considered together. Excellent temporal resolution will add a novel diagnostic dimension. Cost efficiency, mobility, and safety are other significant factors which suggest potential advantages of MWT for brain imaging.

An MWT imaging cycle was simulated as described in the method section. The results of the first series of

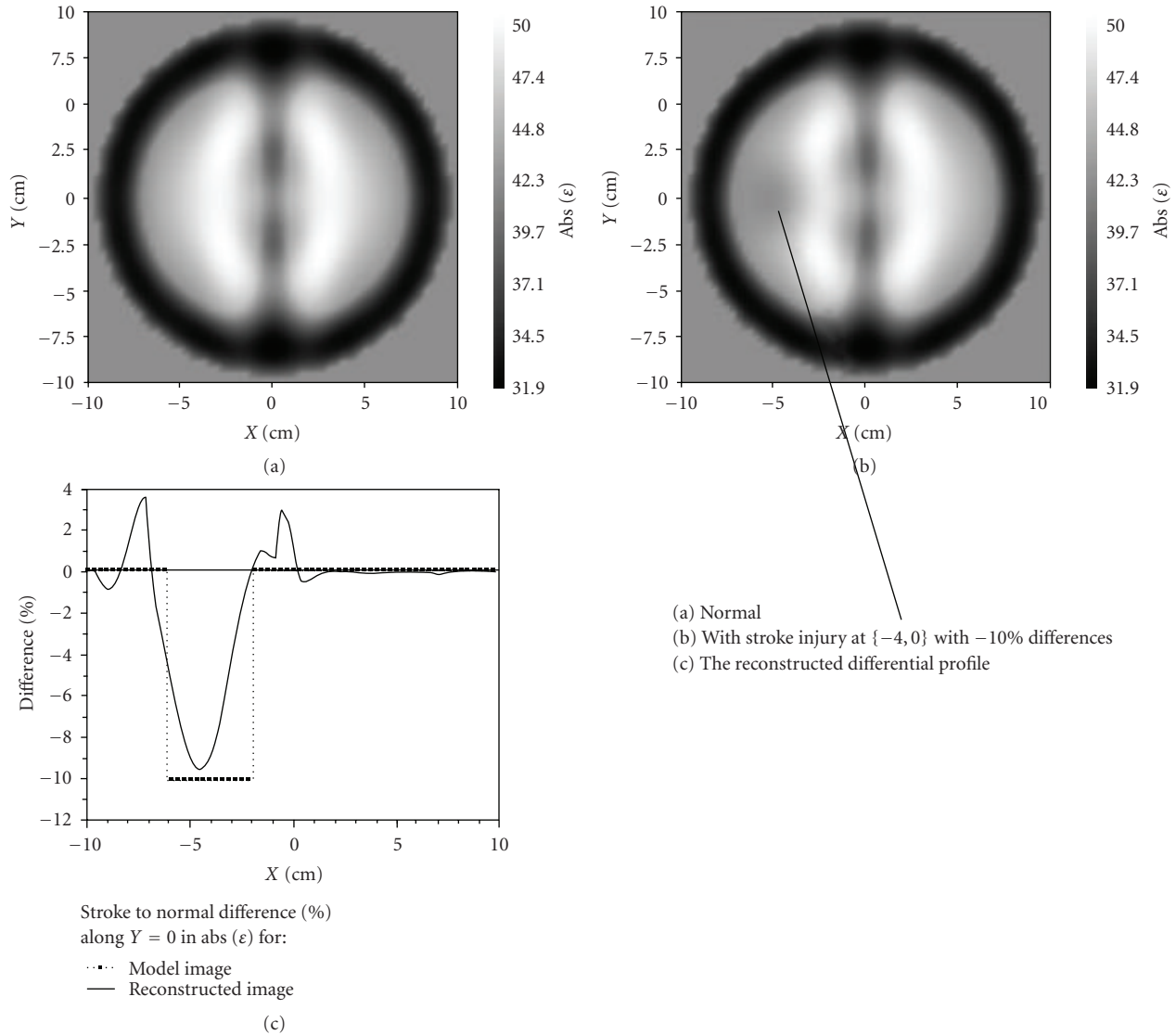


FIGURE 2: Reconstructed MWT images of simulated brain model: (a) normal and (b) with a stroke injury with radius 2 cm centered at $\{-4, 0\}$, (c) the reconstructed differential profile [% difference] through the stroke area. Noiseless case. Frequency 1 GHz.

imaging experiments are presented in Figure 2 for 1 GHz frequency for the 32×32 transmitters \times receivers case. The absolute values of the reconstructed dielectric properties of (a) the normal brain image can be compared with (b) those reconstructed properties for the stroke case. The reconstructed profile through the stroke area of a radius 2 cm located at $X = -4$ cm and $Y = 0$ cm is presented in (c) as % difference in reconstructed values between normal and stroke cases. The shadow of the stroke area can be easily appreciated from the reconstructed image (b). Furthermore, the reconstructed differential profile (c) clearly indicates an area of dielectric inhomogeneity (stroke) in terms of both the geometrical position and the absolute values of the reconstructed dielectric properties, as evidenced by the proximity of the reconstructed profile (line in c) to the expected simulated profile (dots in c).

Next, we focused on the MWT imaging performance at different frequencies with 1% noise. This noise figure does require a good performance of both MWT imaging hardware and the overall MWT imaging reconstruction protocol but is achievable in practice. We used the brain model, with the stroke area of a radius 2 cm located at $\{-4; 0\}$. The imaging results are presented in Figure 3 for frequencies (a) 0.5 GHz, (b) 1.0 GHz, and (c) 2.0 GHz. The area with suspected stroke injury is circled in white. The stroke injury area failed to be reconstructed when a high frequency (2 GHz) is used alone. This unsuccessful imaging result might be attributed to (i) a very high attenuation of EM field at this frequency (see Table 2) and/or to (ii) weaknesses of used imaging approach. However, the used imaging algorithm based on the Newton approach has previously shown a good imaging performance, which is comparable with other powerful,

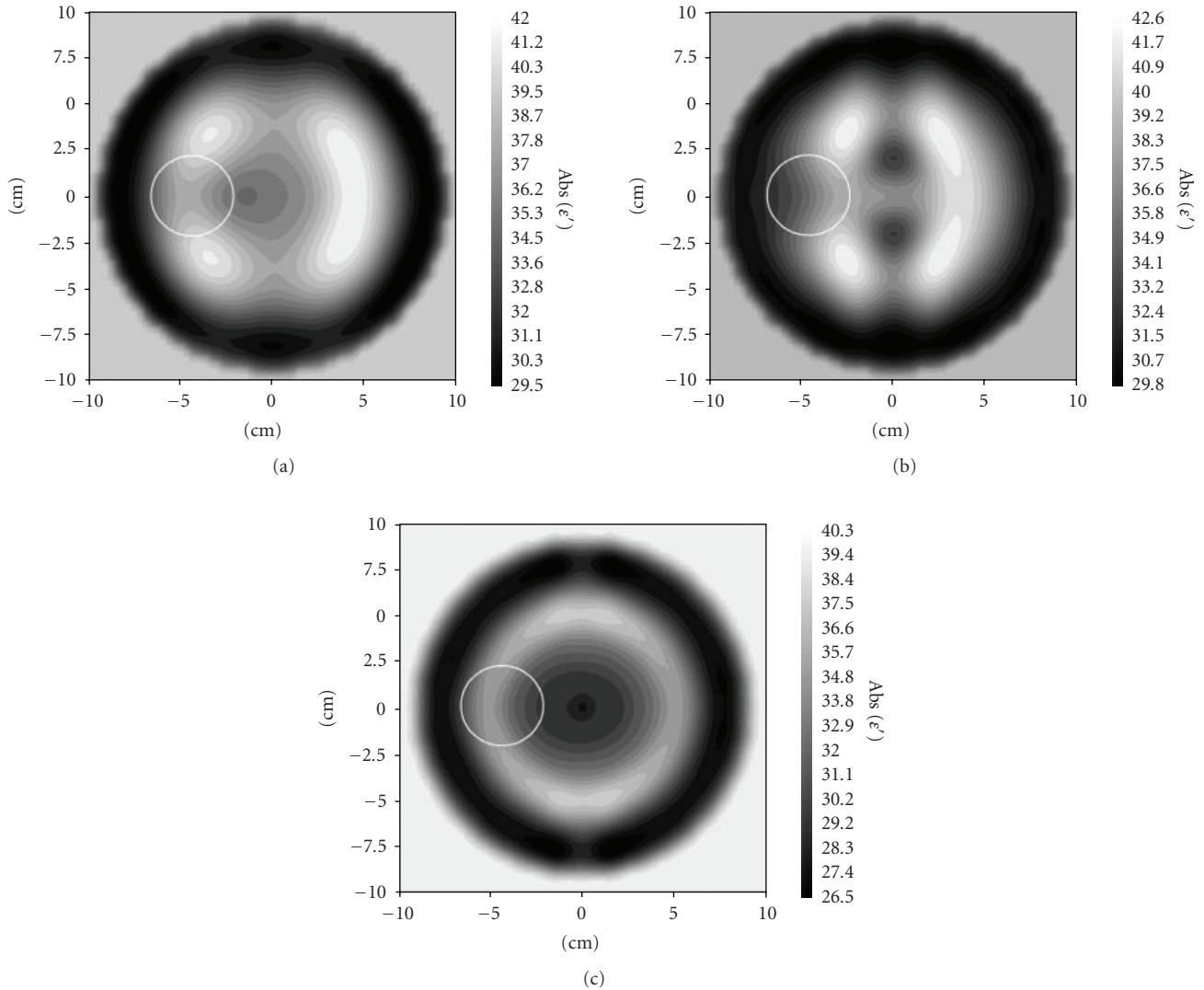


FIGURE 3: Reconstructed MWT images of simulated brain model with a stroke injury with radius 2 cm located at $\{-4, 0\}$ obtained at frequencies (a) 0.5 GHz, (b) 1.0 GHz, and (c) 2.0 GHz. 1% noise. Area with suspected stroke injury is circled in white.

recently developed nonlinear methods of MWT, such as gradient method and contrast source inversion method [15, 24]. An area of stroke injury was reconstructed when MWT imaging was performed at lower frequencies (0.5–1.0 GHz), with more pronouncing detection at 1 GHz (b).

A multifrequency approach further improved the imaging results. Images, obtained at 0.5 GHz and 2.0 GHz, were used as a starting point (initial guess) for further data inversion at 1 GHz. Corresponding scattered EM fields, obtained at individual frequencies, were used. At this stage, the frequency dispersion of dielectric properties of various tissues was not taken into account, that is, we used the same dielectric parameters of the model at 0.5 GHz and 2.0 GHz as we did at 1 GHz (see Table 1). The dielectric properties of biological tissues at this frequency band show significant dispersion. For example, for an averaged brain tissue they vary from $48.5 + j22.7$ at 0.5 GHz to $43.2 + j11.8$ at 2.0 GHz [29]. These variations can be incorporated into

a multifrequency reconstruction approach later on, using well-developed models of tissue dielectric properties, such as the Cole-Cole model or the multicomponent Schwan approach. The aim here was to assess if multifrequency MWT imaging has the potential to improve brain imaging. This is demonstrated in Figure 4, when two multifrequency approaches were used. The first one (a) uses an initial imaging procedure at 0.5 GHz continuing at 1 GHz; the second one uses an initial inversion at 2.0 GHz continuing at 1 GHz. Both approaches demonstrate significant image improvement as compared with the 1st phase of reconstruction (see Figure 3). The area of stroke injury (circled in white) has been reconstructed using both approaches. There is room for improvement and optimisation of multifrequency MWT imaging, which should be a focus of further simulation and experimental studies. The most interesting and technically important question, at the moment, is how distant should frequencies be? If the frequency gap can be narrowed, then

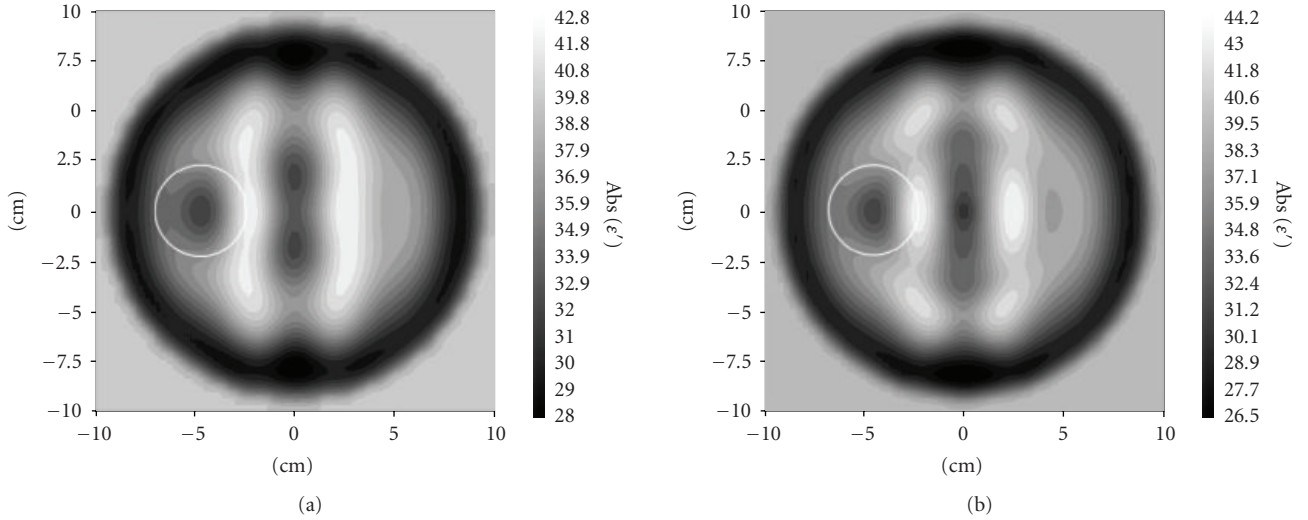


FIGURE 4: Reconstructed MWT images of simulated brain model with a stroke injury with radius 2 cm located at $\{-4, 0\}$ obtained using multifrequency reconstruction: (a) 0.5 GHz and 1.0 GHz and (b) 2.0 GHz and 1.0 GHz. 1% noise. Area with suspected stroke injury is white circled.

TABLE 3: Characteristics and projected performance of an initial MWT system for brain imaging.

MW frequencies	0.7–1.0 GHz
Imaging chamber	3D “Helmet” like, with $R \sim 11$ cm
Number of antennas per a 2D “slice” of an imaging chamber	32–64
Type of antennas	ceramic ($\epsilon \sim 60$ –90) loaded waveguides
Each antenna works as transmitter and receiver	Yes
Measured attenuations [dB]	60–110
S/N ratio [dB]	40–60
IFBW [kHz]	1–10
Output power on antenna	+20 dBm

(i) tissue dispersion might not be taken into account and (ii) narrow band efficient antennas may be used instead of wide band, or a family of narrow bands, antennas.

Presented imaging results are not perfect. However, they indicate that MWT has the potential to determine perfusion related changes in the human brain and that MWT could be developed as a useful new imaging modality for stroke management. There is room for further images improvement at both stages: during reconstruction and at post-processing afterwards.

The projected characteristics of an initial practical MWT system for brain imaging are summarised in Table 3. We intend to use ceramic loaded (with $\epsilon \sim 60$ –90) waveguide antennas as previously successfully used EM sources within MWT imaging chamber [30–32]. The typical dimensions of the antenna tip facing the imaging chamber for frequency of interest are $21 \text{ mm} \times 7 \text{ mm}$. This gives a maximal number of antennas per a 2D “slice” of an imaging chamber of about 32 to 90, depending on an antenna rotation and, consequentially, an imaging approach used (2D, 3D scalar or 3D vector).

4. CONCLUSIONS

(1) The MWT imaging of deep brain tissues and stroke detection presents a significant challenge, being an object of interest located inside of a high dielectric contrast shield, comprising the skull and cerebral spinal fluid.

(2) High performance, nonlinear MWT inversion methods were able to produce biologically meaningful images including images of stroke. At this level of the development of MWT imaging technology, the smallest imaginable area of acute stroke is estimated to be about 2 cm.

(3) Suggested multifrequency MWT has potentials for significant improvement of imaging results.

REFERENCES

- [1] W. Rosamond, K. Flegal, G. Friday, et al., “Heart disease and stroke statistics—2007 update: a report from the American Heart Association Statistics Committee and Stroke Statistics Subcommittee,” *Circulation*, vol. 115, no. 5, pp. e69–e171, 2007.

- [2] H. P. Adams Jr., G. del Zoppo, M. J. Alberts, et al., "Guidelines for the early management of adults with ischemic stroke," *Stroke*, vol. 38, no. 5, pp. 1655–1711, 2007.
- [3] K. W. Muir, A. Buchan, R. von Kummer, J. Rother, and J.-C. Baron, "Imaging of acute stroke," *Lancet Neurology*, vol. 5, no. 9, pp. 755–768, 2006.
- [4] S. Y. Semenov, R. H. Svenson, and G. P. Tatsis, "Microwave spectroscopy of myocardial ischemia and infarction. I. Experimental study," *Annals of Biomedical Engineering*, vol. 28, no. 1, pp. 48–54, 2000.
- [5] S. Y. Semenov, R. H. Svenson, V. G. Posukh, et al., "Dielectrical spectroscopy of canine myocardium during acute ischemia and hypoxia at frequency spectrum from 100 kHz to 6 GHz," *IEEE Transactions on Medical Imaging*, vol. 21, no. 6, pp. 703–707, 2002.
- [6] W. T. Joines, Y. Zhang, C. Li, and R. L. Jirtle, "The measured electrical properties of normal and malignant human tissues from 50 to 900 MHz," *Medical Physics*, vol. 21, no. 4, pp. 547–550, 1994.
- [7] A. J. Surowiec, S. S. Stuchly, J. R. Barr, and A. Swarup, "Dielectric properties of breast carcinoma and the surrounding tissues," *IEEE Transactions on Biomedical Engineering*, vol. 35, no. 4, pp. 257–263, 1988.
- [8] E. C. Fear, S. C. Hagness, P. M. Meaney, M. Okoniewski, and M. A. Stuchly, "Enhancing breast tumor detection with near-field imaging," *IEEE Microwave Magazine*, vol. 3, no. 1, pp. 48–56, 2002.
- [9] S. Y. Semenov, J. Kellam, P. Althausen, et al., "Microwave tomography for functional imaging of extremity soft tissues: feasibility assessment," *Physics in Medicine and Biology*, vol. 52, no. 18, pp. 5705–5719, 2007.
- [10] P. M. Meaney, M. W. Fanning, D. Li, S. P. Poplack, and K. D. Paulsen, "A clinical prototype for active microwave imaging of the breast," *IEEE Transactions on Microwave Theory and Techniques*, vol. 48, no. 11, pp. 1841–1853, 2000.
- [11] E. C. Fear and M. A. Stuchly, "Microwave detection of breast cancer," *IEEE Transactions on Microwave Theory and Techniques*, vol. 48, no. 11, pp. 1854–1863, 2000.
- [12] S. C. Hagness, A. Taflove, and J. E. Bridges, "Three-dimensional FDTD analysis of a pulsed microwave confocal system for breast cancer detection: design of an antenna-array element," *IEEE Transactions on Antennas and Propagation*, vol. 47, no. 5, pp. 783–791, 1999.
- [13] S. Y. Semenov, A. E. Bulyshev, V. G. Posukh, Y. E. Sizov, T. C. Williams, and A. E. Souvorov, "Microwave tomography for detection/imaging of myocardial infarction. I. Excised canine hearts," *Annals of Biomedical Engineering*, vol. 31, no. 3, pp. 262–270, 2003.
- [14] A. J. Devaney, "Current research topics in diffraction tomography," in *Inverse Problems in Scattering and Imaging*, M. Bertero and E. R. Pike, Eds., pp. 47–58, Adam Hilger, New York, NY, USA, 1992.
- [15] A. E. Souvorov, A. E. Bulyshev, S. Y. Semenov, et al., "Microwave tomography: a two-dimensional Newton iterative scheme," *IEEE Transactions on Microwave Theory and Techniques*, vol. 46, no. 11, pp. 1654–1659, 1998.
- [16] R. E. Kleinman and P. M. van den Berg, "Modified gradient method for two-dimensional problems in tomography," *Journal of Computational and Applied Mathematics*, vol. 42, no. 1, pp. 17–35, 1992.
- [17] A. E. Bulyshev, A. E. Souvorov, S. Y. Semenov, et al., "Three-dimensional microwave tomography. Theory and computer experiments in scalar approximation," *Inverse Problems*, vol. 16, no. 3, pp. 863–875, 2000.
- [18] A. Abubakar, P. M. van den Berg, and J. J. Mallorqui, "Imaging of biomedical data using a multiplicative regularized contrast source inversion method," *IEEE Transactions on Microwave Theory and Techniques*, vol. 50, no. 7, pp. 1761–1771, 2002.
- [19] N. Joachimowicz, J. J. Mallorqui, J.-C. Bolomey, and A. Broquetas, "Convergence and stability assessment of Newton-Kantorovich reconstruction algorithms for microwave tomography," *IEEE Transactions on Medical Imaging*, vol. 17, no. 4, pp. 562–570, 1998.
- [20] P. Lobel, R. E. Kleinman, Ch. Pichot, L. Blanc-Féraud, and M. Borlaud, "Conjugate-gradient method for solving inverse scattering with experimental data," *IEEE Antennas and Propagation Magazine*, vol. 38, no. 3, pp. 48–51, 1996.
- [21] W. C. Chew and Y. M. Wang, "Reconstruction of two-dimensional permittivity distribution using the distorted Born iterative method," *IEEE Transactions on Medical Imaging*, vol. 9, no. 2, pp. 218–225, 1990.
- [22] H. Harada, D. J. N. Wall, T. Takenaka, and M. Tanaka, "Conjugate gradient method applied to inverse scattering problem," *IEEE Transactions on Antennas and Propagation*, vol. 43, no. 8, pp. 784–792, 1995.
- [23] P. M. Meaney, K. D. Paulsen, A. Hartov, and R. K. Crane, "Microwave imaging for tissue assessment: initial evaluation in multitarget tissue-equivalent phantoms," *IEEE Transactions on Biomedical Engineering*, vol. 43, no. 9, pp. 878–890, 1996.
- [24] S. Y. Semenov, A. E. Bulyshev, A. Abubakar, et al., "Microwave-tomographic imaging of the high dielectric-contrast objects using different image-reconstruction approaches," *IEEE Transactions on Microwave Theory and Techniques*, vol. 53, no. 7, pp. 2284–2293, 2005.
- [25] A. E. Bulyshev, A. E. Souvorov, S. Y. Semenov, V. G. Posukh, and Y. E. Sizov, "Three-dimensional vector microwave tomography: theory and computational experiments," *Inverse Problems*, vol. 20, no. 4, pp. 1239–1259, 2004.
- [26] A. Peyman, S. J. Holden, S. Watts, R. Perrott, and C. Gabriel, "Dielectric properties of porcine cerebrospinal tissues at microwave frequencies: in vivo, in vitro and systematic variation with age," *Physics in Medicine and Biology*, vol. 52, no. 8, pp. 2229–2245, 2007.
- [27] S. Gabriel, R. W. Lau, and C. Gabriel, "The dielectric properties of biological tissues: II. Measurements in the frequency range 10 Hz to 20 GHz," *Physics in Medicine and Biology*, vol. 41, no. 11, pp. 2251–2269, 1996.
- [28] G. Schmid, G. Neubauer, and P. R. Mazal, "Dielectric properties of human brain tissue measured less than 10 h postmortem at frequencies from 800 to 2450 MHz," *Bioelectromagnetics*, vol. 24, no. 6, pp. 423–430, 2003.
- [29] C. Gabriel, "Compilation of the dielectric properties of body tissues at RF and microwave frequencies," Tech. Rep. AL/OE-TR-1996-0037, Brooks Air Force Base, San Antonio, Tex, USA, 1996, <http://www.fcc.gov/fcc-bin/dielec.sh>.
- [30] S. Y. Semenov, R. H. Svenson, A. E. Bulyshev, et al., "Microwave tomography: two-dimensional system for biological imaging," *IEEE Transactions on Biomedical Engineering*, vol. 43, no. 9, pp. 869–877, 1996.
- [31] S. Y. Semenov, R. H. Svenson, A. E. Bulyshev, et al., "Three-dimensional microwave tomography: experimental prototype of the system and vector Born reconstruction method," *IEEE Transactions on Biomedical Engineering*, vol. 46, no. 8, pp. 937–946, 1999.
- [32] S. Y. Semenov, R. H. Svenson, A. E. Bulyshev, et al., "Three-dimensional microwave tomography: initial experimental imaging of animals," *IEEE Transactions on Biomedical Engineering*, vol. 49, no. 1, pp. 55–63, 2002.

- [33] P. M. Meaney, K. D. Paulsen, A. Hartov, and R. K. Crane, "Microwave imaging for tissue assessment: initial evaluation in multitarget tissue-equivalent phantoms," *IEEE Transactions on Biomedical Engineering*, vol. 43, no. 9, pp. 878–890, 1996.
- [34] F.-C. Chen and W. C. Chew, "Experimental verification of super resolution in nonlinear inverse scattering," *Applied Physics Letters*, vol. 72, no. 23, pp. 3080–3082, 1998.
- [35] S. Y. Semenov, R. H. Svenson, A. E. Bulyshev, et al., "Spatial resolution of microwave tomography for detection of myocardial ischemia and infarction-experimental study on two-dimensional models," *IEEE Transactions on Microwave Theory and Techniques*, vol. 48, no. 4, pp. 538–544, 2000.

Research Article

Improved Delay-and-Sum Beamforming Algorithm for Breast Cancer Detection

M. Klemm, I. J. Craddock, J. A. Leendertz, A. Preece, and R. Benjamin

*Centre for Communications Research, Department of Electrical and Electronic Engineering,
University of Bristol, Woodland Road, Bristol BS8 1UB, UK*

Correspondence should be addressed to M. Klemm, m.klemm@bristol.ac.uk

Received 4 October 2007; Accepted 3 April 2008

Recommended by Elise Fear

We have evaluated a modified delay-and-sum (DAS) beamforming algorithm for breast cancer detection with a microwave radar-based system. The improved DAS algorithm uses an additional weight factor calculated at each focal point to improve image quality. These weights essentially represent the quality of preprocessing and coherent radar operation. Using a multistatic UWB radar system based on a hemispherical antenna array, we present experimental detection of 7 mm and 10 mm phantom tumours. We show that the new proposed DAS algorithm improves signal-to-clutter ratio in focused images by 2.65 dB for 10 mm tumour, and by 4.4 dB for 7 mm tumour.

Copyright © 2008 M. Klemm et al. This is an open access article distributed under the Creative Commons Attribution License, which permits unrestricted use, distribution, and reproduction in any medium, provided the original work is properly cited.

1. INTRODUCTION

X-ray mammography is currently the most common technique used in breast cancer screening. It employs ionising radiation, requires uncomfortable compression of the breast during the examination, and is of limited value for younger women. These limitations of mammography have resulted in research into alternative methods for imaging breast cancer.

Microwave radar-based imaging [1] is one of the more promising candidates and has attracted the interest of a number of research groups around the world.

In radar-based imaging, the goal is to create a map of microwave scattering, arising from the contrast in dielectric properties within the breast. The radar approach originates from military and ground-penetrating applications, and was proposed for breast cancer detection in the late nineties independently by Benjamin in 1996 [2] and Hagness et al. in 1998 [3].

The University of Bristol team is working on multistatic ultrawideband (UWB) radar for breast cancer detection. Our radar system is based on a real (as opposed to synthetic) aperture antenna array. We have also developed a realistic 3D curved breast phantom with appropriate electrical properties. Moreover, our experimental system was built in such

a way that it can be used directly with real breast cancer patients (clinical trials have been recently commenced).

2. MEASUREMENT SETUP

We have developed a microwave radar for breast cancer detection, based on a curved hemispherical antenna array. In this paper, we present results obtained using a second-generation symmetrical antenna array. The new symmetrical antenna array, shown in Figure 1, uses a recently redesigned, smaller, stacked-patch antenna [4]. The array is formed around the lower part of a 78 mm radius sphere, in four rows of four antennas. Antennas are aligned in rows and columns; thus the array has two axes of symmetry.

During laboratory experiments, the array is first filled with a matching medium, the spherical skin phantom (2 mm thick) is placed in the correct position, and then we attach a tank to the top of the antenna array to finally fill it with a breast fat equivalent liquid [5] (the same as the matching medium). This setup represents truly a three-dimensional (3D) breast phantom. The chest wall is not considered in our experiments. The electrical properties of the tissue phantom are based on the published permittivity values for average human breast. At the frequency of 6 GHz, materials have

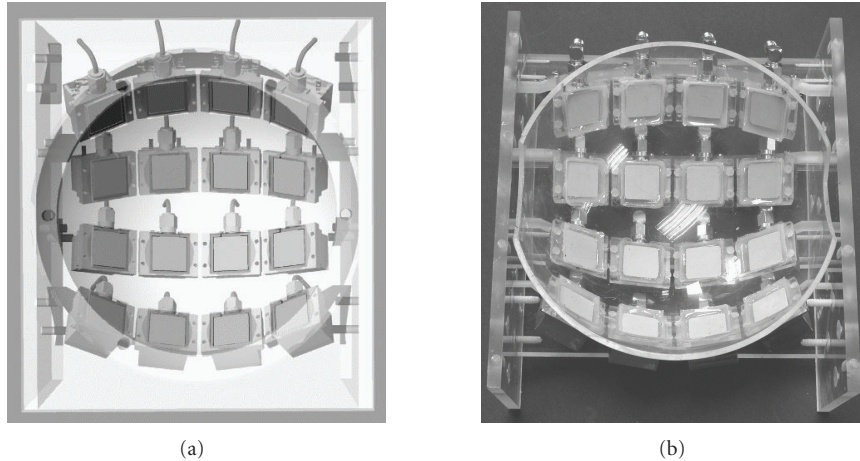


FIGURE 1: Symmetrical curved antenna array used in microwave radar for breast cancer detection: (a) CAD model, (b) photograph of the manufactured array. The array consists of sixteen UWB antennas populated on a section of hemisphere.

the following values. (a) Breast fat/matching medium has permittivity close to 10 and attenuation of 0.8 dB/cm; (b) skin phantom has permittivity of 30 and attenuation of 16 dB/cm; (c) tumour phantom has permittivity close to 50 and conductivity of 7 S/m. More details about our breast phantom can be found in [6].

The contrast between dielectric properties of breast fat and tumour phantom materials is around 1 : 5. Recently published data in [7], based on a large clinical study, suggest that the contrast between healthy and malignant breast tissues might also be lower. The lower contrast obviously poses a more challenging radar detection problem.

Our radar system operates in the multistatic mode. With sixteen antennas in the array, one hundred and twenty (120) independent radar measurements are recorded for processing (the monostatic measurement is not performed). Measurements are performed in the frequency domain between 3 and 10 GHz using a standard vector network analyser (VNA). All recorded radar signals are transformed into the time domain for further signal processing (described in Section 3).

3. FOCUSING ALGORITHM

3.1. Extraction of tumour response from measured radar data

The first step of signal processing deals with the extraction of the tumour response from the raw measured data. This process must be performed before equalisation and beamforming algorithms will be applied. When a monostatic synthetic aperture radar is used for breast cancer detection, tumour extraction aims at removing strong skin reflection from measured data. This is usually performed by simple subtraction from the averaged skin reflection signal (see [8]), or by more sophisticated algorithms as presented in [9].

The approach we use to extract the tumour response is different. In our multistatic real aperture array, the measured

response contains not only strong skin reflections, but also reflections from other mechanical parts of the array as well as antenna coupling signals. All these undesired signals are usually of greater amplitude than that of the tumour response. To subtract all unwanted signals, we physically rotate the antenna array around its center and perform a second radar measurement. This target displacement method is commonly used in radar cross-section measurements [10, 11] to subtract undesired signals.

Rotation gives us two sets of measured data, in which undesired signals such as antenna coupling or skin reflections are almost identical and appear at the same time position; therefore they can be eliminated. In contrast, a tumour response will appear at different time position in these two measured sets (unless it is on the axis of rotation). Applicability of this technique will depend on the homogeneity of the breast within a given angle defined by rotation. We therefore assume that within the angle of array rotation, (a) distance between antennas and skin remains unchanged, (b) skin properties and thickness are the same, and (c) normal breast tissue properties do not change. For more details about the performance of this tumour extraction technique, please refer to [12].

3.2. Preprocessing (equalisation)

Before applying the focusing algorithm, we have to perform a preprocessing step. This process aims at the equalisation of scattered tumour responses for different antenna pairs. Ideal preprocessing would result in all received pulses being of the same shape and amplitude, and perfectly time-aligned. In our preprocessing, the following steps are performed: (1) extraction of the tumour response from measured data (see [12]), (2) equalisation of tissue losses, and (3) equalisation of radial spread of the spherical wavefront. In the work reported herein for simplicity we do not account for the frequency dependence of the tissue losses nor for the frequency-dependent radiation patterns of the antennas.

3.3. Standard delay-and-sum algorithm

Delay-and-sum (DAS) beamforming is a basic and well-known method [13, 14]. First, we perform the preprocessing steps described above. Next, appropriate time-delays T_i for all received signals are computed. The time-delay T_i for a given transmitting and receiving antenna is calculated based on the antenna's position, position of the focal point $r = (x, y, z)$, as well as an estimate of average wave propagation speed, which in our case is simply assumed to be constant across the band.

During the focusing, the focal point moves from one position to another within the breast, resulting in spatial beamforming. At each location, all time-shifted responses are coherently summed and integrated. Integration is performed on the windowed signal, and the length of the integration window is chosen according to the system bandwidth. A three-dimensional (3D) map of scattered energy is formed in this way. The main advantage of the DAS algorithm is its simplicity, robustness, and short computation time.

Essentially, the scattered energy at the given focal point within the breast volume can be expressed as

$$F_e(x, y, z) = \int_0^\tau \left(\sum_{i=1}^M w_i(x, y, z) \cdot y_i(t - T_i(x, y, z)) \right)^2 dt, \quad (1)$$

where $M = N(N - 1)/2$ (N is the number of antennas in the array), w_i is the location-dependent weight calculated during preprocessing, y_i is the measured radar signal, and T_i is the time-delay. τ is the length of the integration window, chosen according to the system bandwidth. Due to the antenna effects and dispersion, the integration window we utilize following coherent summation is 50 percent longer than the duration of the synthetic input pulse and equals 0.55 nanosecond. We have investigated the dependence of the window length on focusing quality, and this value gave the best results.

3.4. Improved delay-and-sum algorithm

The improved DAS algorithm uses an additional weighting factor QF (quality factor), compared to the standard DAS. QF can be interpreted as a quality factor of the coherent focusing algorithm. It is calculated in three steps. Firstly, for each focal point, we plot a curve of energy collection during the coherent signal summation. An example of such a measured curve at a focal point containing a tumour response is presented in Figure 2.

Next, the energy collection curve is rescaled by normalising it to the standard deviation of energy, σ_e , for all radar signals used in the summation. Normalisation is actually performed using multiplication by $1/(1 + \sigma_e)$, since in the ideal case of equal energy in all (equalised) measured radar signals, $\sigma_e = 0$. This may be thought of as a heuristic scaling of the data to give greater weight to those signals that, following equalisation, more closely resemble the desired case of equal energy. The utility of this heuristic weighting is evident from the results presented in the following sections.

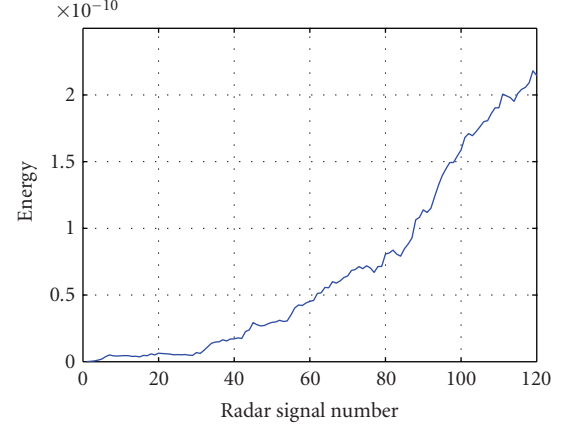


FIGURE 2: Example of the curve of energy collection (measured data).

In a last step, we estimate the coefficients of a second-order polynomial ($y = ax^2 + bx + c$), which is the least-square fit of the normalised curve of coherent energy collection. The choice of the second-order polynomial comes from the fact that a curve of energy collection during a perfect coherent signal summation would follow a quadratic curve. Then, we assume that $QF = a$. An order in which the signals are taken should not change the shape of the curve, assuming the perfect equalisation. In practise, due to a nonideal equalisation, the shape of the curve of energy collection will slightly depend on the order in which signals are summed. However, it has negligible effect on an a value since the final value of summed energy is constant; a is calculated using least-square fitting. Finally, the characteristic equation of the improved DAS algorithm is expressed as

$$F_e(x, y, z) = QF(x, y, z) \cdot \int_0^\tau \left(\sum_{i=1}^M w_i(x, y, z) \cdot y_i(t - T_i(x, y, z)) \right)^2 dt. \quad (2)$$

In the following section, we will present the experimental results of phantom tumours detection, and discuss the new DAS algorithm.

4. EXPERIMENTAL DETECTION RESULTS

This section presents the experimental results of tumour detection using our curved antenna array and 3D breast phantom. Focusing results for standard DAS algorithm are compared to those for the improved DAS, and differences between both algorithms are discussed. Results are presented for tumours of two different sizes located at different positions: (a) 10 mm spherical tumour located at position $P_T(x = 20, y = 20, z = -20)$, (b) 7 mm spherical tumour located at position $P_T(x = 20, y = 10, z = -10)$. All coordinates are quoted in millimeter.

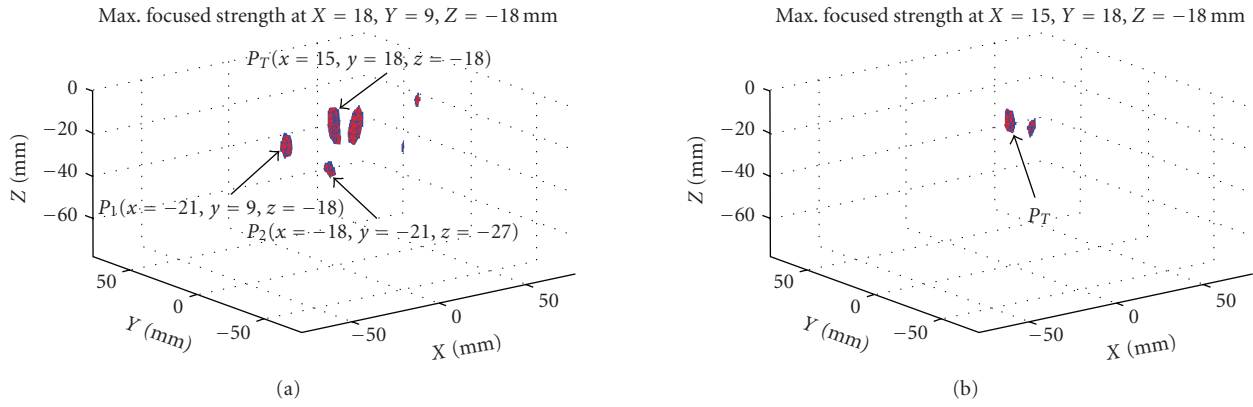


FIGURE 3: Detection results of a 10 mm spherical phantom tumour: (a) standard DAS, (b) improved DAS with $QF = a$. 3D figures present -3 dB contour map of scattered energy.

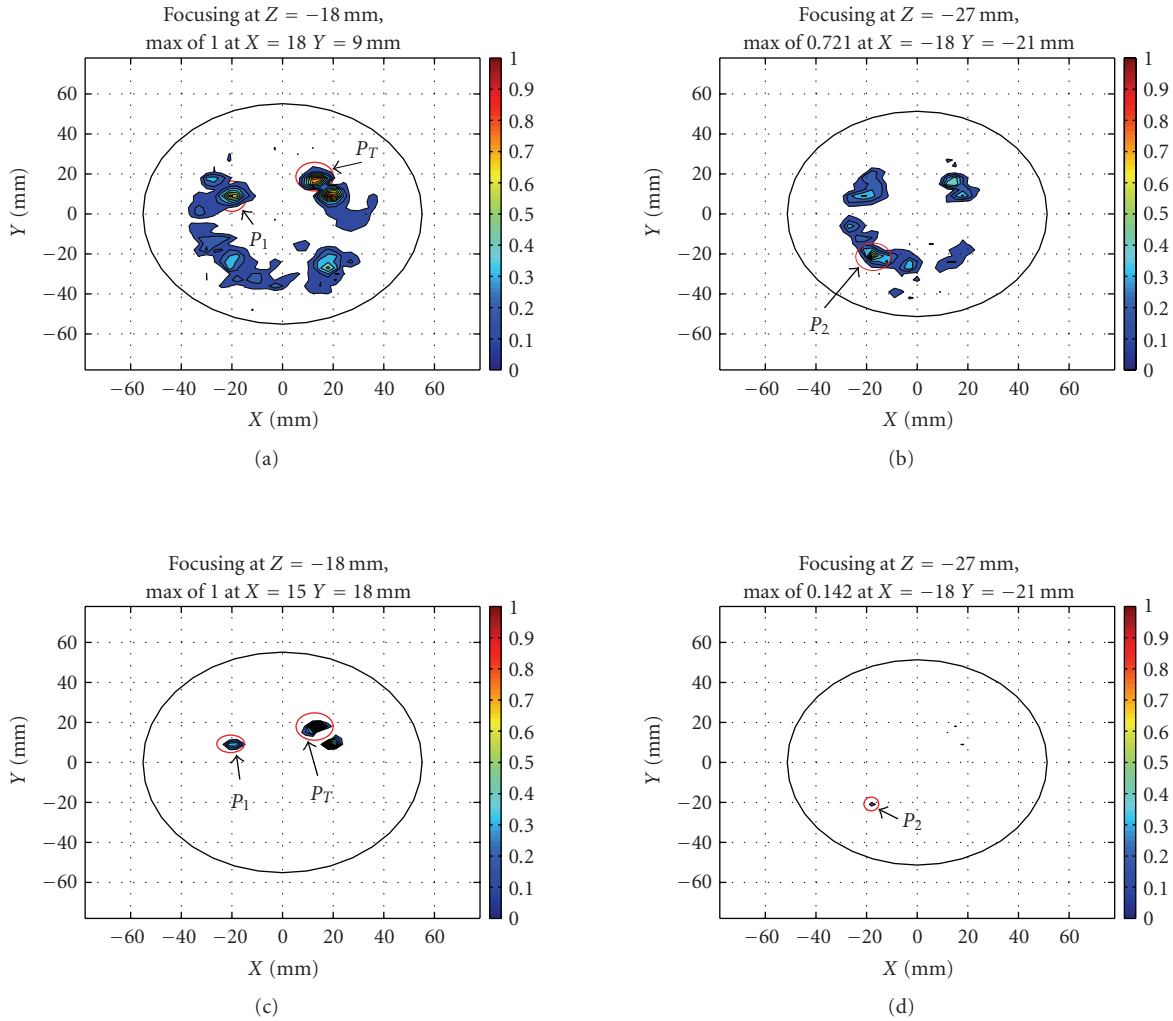


FIGURE 4: 2D focusing results for standard and improved DAS algorithms, for different horizontal planes along the z -axis: (a) standard DAS ($z = -18$), (b) standard DAS ($z = -27$), (c) improved DAS ($z = -18$), (d) improved DAS ($z = -27$). 2D contour plots show signal energy on a linear scale, normalised to the maximum in the 3D volume; values below 0.1 are rendered as white.

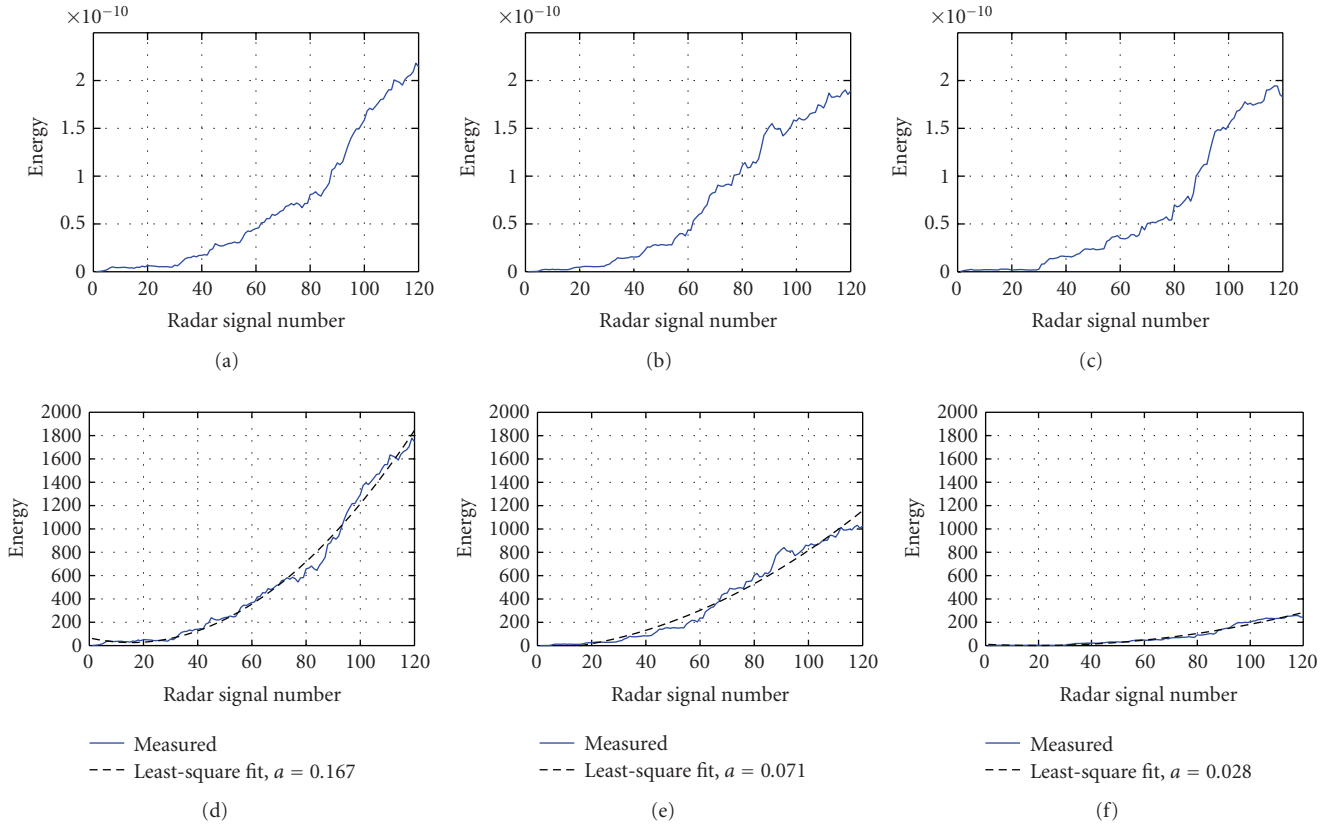


FIGURE 5: Curves of energy collection at focal points P_T , P_1 , and P_2 (see Figure 6(a)): (a) curve for P_T as in standard DAS, (b) curve for P_1 as in standard DAS, (c) curve for P_2 in standard DAS, (d) curve for P_T as in improved DAS together with the fitted polynomial, (e) curve for P_1 in the improved DAS together with the fitted polynomial, (f) curve for P_2 in the improved DAS together with the fitted polynomial.

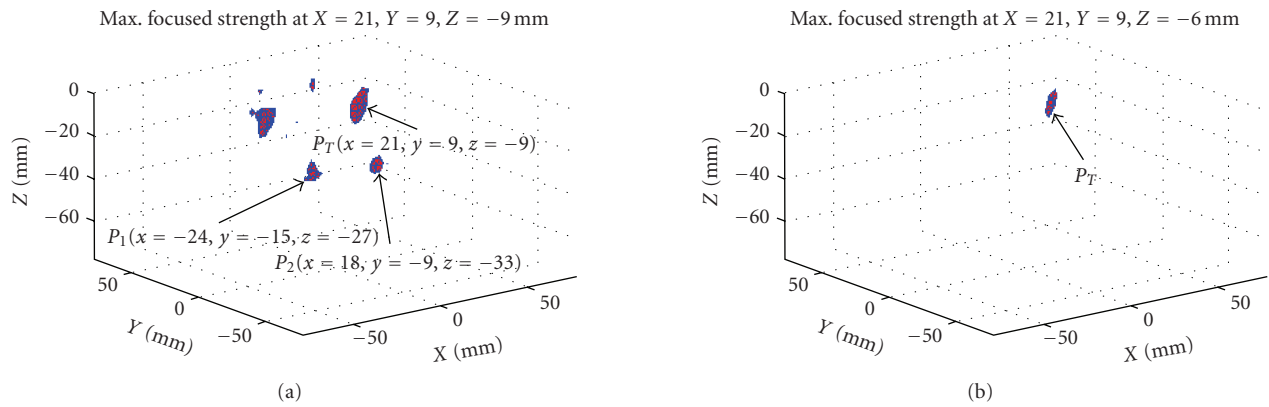


FIGURE 6: Detection results of a 7 mm spherical phantom tumour: (a) standard DAS, (b) improved DAS with $QF = a$. 3D figures present -3 dB contour map of scattered energy.

4.1. 10 mm spherical phantom tumour

In Figure 3, we present 3D focusing results for a 10 mm spherical phantom tumour located at the position $P_T(x = 20, y = 20, z = -20)$. Figures present -3 dB contour maps of scattered energy, when the focusing was performed using the standard DAS algorithm (Figure 3(a)) and the improved DAS algorithm (Figure 3(b)).

As we can see in Figure 3(a), there are several scatterers present in the image when focusing using standard DAS algorithm. The strongest scatterer within the entire 3D volume is located at position $P_T(x = 15, y = 18, z = -18)$, and it is associated with tumour response. In Figure 3, we have also indicated locations of two other strong scatterers located at positions $P_1(x = -21, y = 9, z = -18)$ and $P_2(x = -18, y = -21, z = -27)$. In Figures 4(a) and

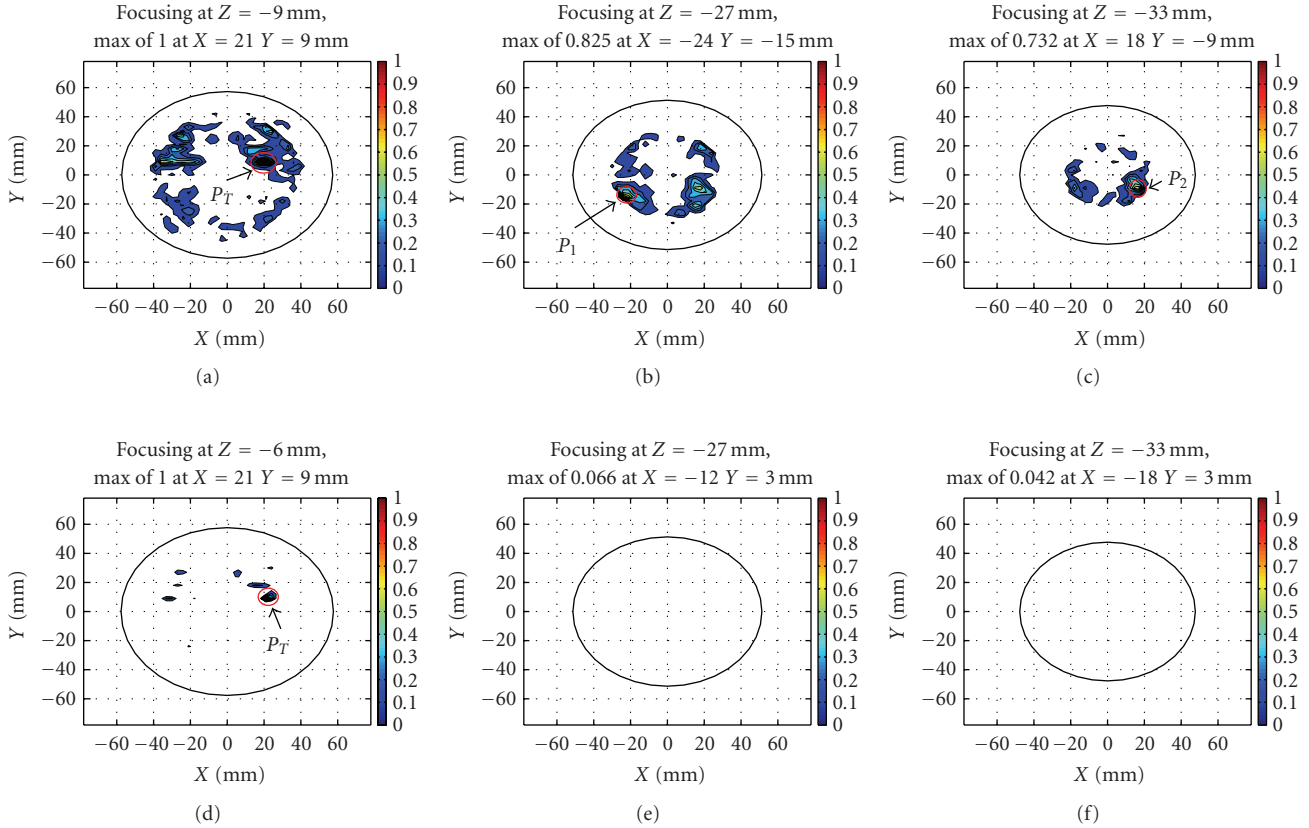


FIGURE 7: 2D focusing results for standard and improved DAS algorithms, for different horizontal planes along the z -axis: (a) standard DAS ($z = -9$), (b) standard DAS ($z = -27$), (c) standard DAS ($z = -33$), (d) improved DAS ($z = -6$), (e) improved DAS ($z = -27$), (f) improved DAS ($z = -33$). 2D contour plots show signal energy on a linear scale, normalised to the maximum in the 3D volume; values below 0.1 are rendered as white.

4(b), we present 2D focusing results for standard DAS on the horizontal planes (z -axis) containing the P_T , P_1 (both at $z = -18$), and P_2 ($z = -27$) signals associated with clutter. The 2D contour plots show signal energy on a linear scale, normalised to the maximum in the entire 3D volume (values below 0.1 are rendered as white). The skin location at each plane is presented as a black circle. From Figure 4(a), for the plane containing tumour we can relatively easily recognise the focused tumour response (P_T) and the nearby *twin* tumour response (at $x = 18$, $y = 9$; the *twin target* response is due to tumour extraction method—mechanical array rotation by 10 degrees). In the same figure, we can also see that the strong clutter at position P_1 and the weaker clutter (blue patches) at other positions arose from imperfect extraction of tumour response. Figure 4(b) presents the 2D focusing result through the plane ($z = -27$) containing strong clutter scatterer at P_2 .

Significantly better detection results were obtained using improved DAS algorithm presented herein. 3D and 2D focusing results for the improved DAS are presented in Figures 3(b) and 4(c)-4(d), respectively. The 3D contour map of scattered energy contains only the tumour response (P_T) and the twin tumour response. Unlike the image obtained using standard DAS, there are no other clutter scatterers visible. Signal-to-clutter ratio, defined as the ratio

between energy of the tumour response and the strongest clutter energy within a single 3D dataset, was improved from 1.25 dB for standard DAS to 3.9 dB for improved DAS (2.65 dB improvement).

The same improved performance is observed in the 2D results shown in Figures 4(c) and 4(d). In the horizontal plane containing P_T , the tumour response clearly stands out, and very little clutter exists in the image. In the plane containing P_2 , clutter is also significantly suppressed.

Results described above (Figures 3 and 4) have shown the improved tumour detection of the new DAS algorithm, which uses additional weight QF, compared to standard DAS. In what follows, we will analyse the improved DAS algorithm and explain why it provides better results. To do so, we will go through all steps of the new algorithm at the three focal points (P_T , P_1 , P_2) mentioned earlier in this section.

After extraction of the tumour response from measured data (by mechanical array rotation), resultant signals are being preprocessed and time-aligned. This initial step is identical for standard and improved DAS algorithms. Then, all pulsed signals (120 signals for our radar) are coherently summed. During this process, the curve of coherent energy collection is obtained, at each focal point within the focusing volume. This curve is presented in Figures 5(a)–5(c) for focal points P_T , P_1 , P_2 , respectively. The final value obtained after

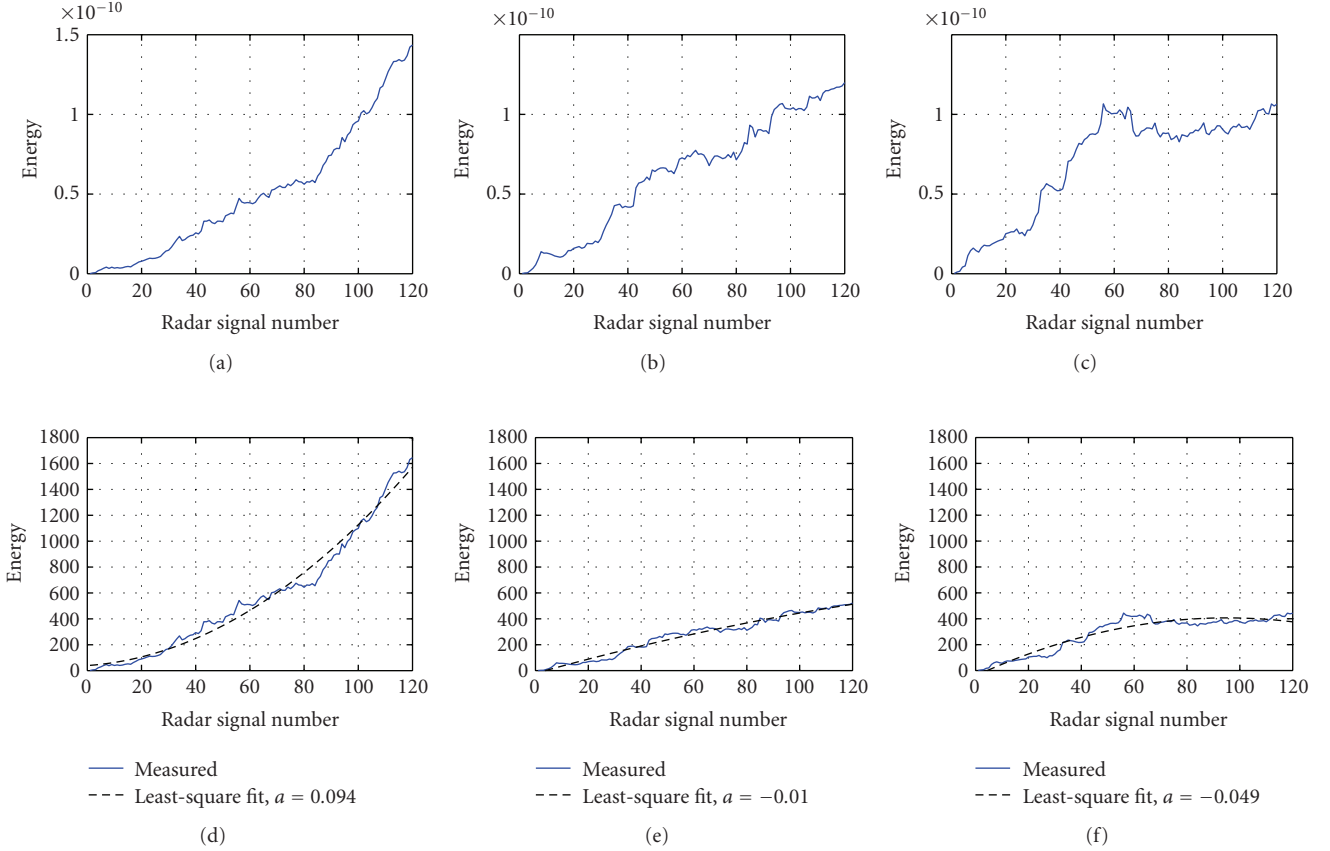


FIGURE 8: Curves of energy collection at focal points P_T , P_1 , and P_2 (see Figure 6(a)): (a) curve for P_T as in standard DAS, (b) curve for P_1 as in standard DAS, (c) curve for P_2 as in standard DAS, (d) curve for P_T as in improved DAS together with the fitted polynomial, (e) curve for P_1 in the improved DAS together with the fitted polynomial, (f) curve for P_2 in the improved DAS together with the fitted polynomial.

summation of all radar signals is equal to the focused energy F_e in standard DAS.

If we assume that the focused energy for tumour location using standard DAS algorithm is equal to unity $F_s(P_T) = 1$, focused energy values at focal points P_1 and P_2 equal $F_s(P_1) = 0.88$ and $F_s(P_2) = 0.85$. Next, in the improved DAS algorithm, we calculate the standard deviation of energy σ_e for all radar signals, and recalculate energy collection curves by normalising them to σ_e . The rationale to do so is based on the fact that after the initial preprocessing equalisation step, all radar signals should have similar energy.

We can see the rescaled (normalised) curves in Figures 5(d)–5(f) (solid blue curves) for locations P_T , P_1 , P_2 , respectively. We observe that after this normalisation the results have improved since the curves for P_1 , P_2 have significantly smaller amplitudes than for P_T . Since clutter signals cannot be thought of as being totally uncorrelated, we do not however simply use σ_e as the weight factor, but we apply additional criteria related to the coherent summation of radar signals as follows.

As known in the ideal coherent summation of scattered pulses, the energy collection curve should follow a parabola ($y = x^2$). Therefore, to check the “quality” of coherent addition of radar signals in our system, we perform a second-order polynomial ($y = ax^2 + bx + c$) fitting (in the least-

square sense) to the measured energy collection curves. This process is performed on the normalised curves. Results of polynomial fitting are shown in Figures 5(d)–5(f) (dashed black curves), and the constant a associated with x^2 equals $a = 0.167$ for P_T , $a = 0.071$ for P_1 , and $a = 0.028$ for P_2 . Then, assuming that $QF = a$ (see (2)), focused energy using improved DAS at our example points of interest is $F_s(P_T) = 1$, $F_s(P_1) = 0.38$, and $F_s(P_2) = 0.14$. The result of applying this process throughout the entire volume is shown in 3D and 2D by Figures 3 and 4, respectively.

4.2. 7 mm spherical phantom tumour

This example presents the detection of a smaller 7 mm spherical tumour phantom. In Figure 6, we present 3D focusing results for the 6 mm spherical phantom tumour located at the position $P_T(x = 20, y = 10, z = -10)$. Figures present -3 dB contour maps of scattered energy, when focusing was performed using the standard DAS algorithm (Figure 6(a)) and the improved DAS algorithm (Figure 6(b)).

As we can see in Figure 6(a), by using standard DAS algorithm there are multiple scatterers present in the image. As we did previously for the 10 mm tumour, again this time we concentrate the attention on three focal points: spherical

phantom tumour located at $P_T(x = 21, y = 9, z = -6)$, the strongest clutter scatterer at $P_1(x = -24, y = -15, z = -27)$, and another strong clutter at $P_2(x = 18, y = -9, z = -33)$. A significantly better image, with clearly visible tumour scatterer at P_T and no other clutter targets, is presented in Figure 6(b) for the improved DAS algorithm. Signal-to-clutter ratio was improved from 0.8 dB for standard DAS to 5.2 dB for improved DAS, providing 4.4 dB better performance using a proposed algorithm.

Looking at all 2D focused images (Figure 7) for standard DAS, we can observe that clutter strength generally increases closer to skin. This observation is confirmed when looking at locations of focal points investigated above. In our 3D breast phantom, the 2 mm skin layer has a radius $r_{\text{skin}} = 59$ mm. The true tumour response at P_T is located 35 mm away from the skin ($r_{P_T} = 24$ mm), the strongest clutter signal at P_1 is 20 mm away from the skin ($r_{P_1} = 39$ mm), and another strong clutter at P_2 is also 20 mm away from the skin ($r_{P_2} = 39$ mm). As we can see, all the strong clutter signals are located closer to skin than to the tumour.

In Figure 8, curves of coherent energy collection are presented for focal points P_T, P_1, P_2 . Plots associated with standard DAS algorithm are shown in Figures 8(a)–8(c) for focal points P_T, P_1, P_2 , respectively. The value obtained after summation of all radar signals is equal to the focused energy F_e in standard DAS. Next, in the improved DAS algorithm we calculate the standard deviation of energy σ_e for all radar signals, and recalculate energy collection curves by normalising them to σ_e . Resultant normalised curves for locations P_T, P_1 , and P_2 are depicted in Figures 8(d)–8(f) (solid blue curves), respectively.

We observe that, after normalisation, the curves for P_1, P_2 have significantly dropped compared to P_T , due to the higher values of standard deviation of the energy content of the radar signals. Next, we performed the second-order polynomial fitting on the normalised energy collection curves to obtain the weight factor $\text{QF} = a$. Results of polynomial fitting are shown as dashed black curve in Figures 8(d)–8(f). The constant a associated with x^2 equals $a = 0.094$ for P_T , $a = -0.01$ for P_1 , and $a = -0.049$ for P_2 . Interestingly, due to a noncoherent signal summation for focal points P_1 and P_2 , a has not only lower absolute value than for P_T , but has also negative sign. The focused energy F_e using improved DAS algorithm (as in (2)) will become negative for focal points, where $\text{QF} = a < 0$, additionally improving imaging results.

5. CONCLUSIONS

In this paper, we have presented a modified delay-and-sum (DAS) beamforming algorithm for breast cancer detection. The improved DAS algorithm uses an additional weight factor calculated at each focal point, to improve image quality. These weights essentially represent the quality of the preprocessing step and the coherent radar operation. Using measured data from a multistatic UWB radar system, we have presented experimental detection of 7 mm and 10 mm tumours in a phantom. We have shown that the proposed new DAS algorithm improves signal-to-clutter

ratio in focused images by 2.65 dB for 10 mm tumour, and by 4.4 dB for 7 mm tumour.

Further, it may be noted that this improvement in signal-to-clutter ratio is comparable to that achieved [12] by a much more complex data-adaptive algorithm based on robust Capon beamforming. Importantly, however, it requires significantly less (order-of-magnitude) computation time.

REFERENCES

- [1] E. C. Fear, P. M. Meaney, and M. A. Stuchly, "Microwaves for breast cancer detection?" *IEEE Potentials*, vol. 22, no. 1, pp. 12–18, 2003.
- [2] R. Bejnamin, "Synthetic, post-reception focusing in near-field radar," in *Proceedings of the EUREL International Conference on the Detection of Abandoned Land Mines: A Humanitarian Imperative Seeking a Technical Solution*, pp. 133–137, Edinburgh, UK, October 1996.
- [3] S. C. Hagness, A. Taflove, and J. E. Bridges, "Two-dimensional FDTD analysis of a pulsed microwave confocal system for breast cancer detection: fixed-focus and antenna-array sensors," *IEEE Transactions on Biomedical Engineering*, vol. 45, no. 12, pp. 1470–1479, 1998.
- [4] I. J. Craddock, M. Klemm, J. Leendertz, A. W. Preece, and R. Benjamin, "An improved hemispherical antenna array design for breast imaging," in *Proceedings of the 2nd European Conference on Antennas and Propagation (EuCAP '07)*, Edinburgh, UK, November 2007.
- [5] J. Leendertz, A. Preece, R. Nilavalan, I. J. Craddock, and R. Benjamin, "A liquid phantom medium for microwave breast imaging," in *Proceedings of the 6th International Congress of the European Bioelectromagnetics Association*, Budapest, Hungary, November 2003.
- [6] M. Klemm, I. J. Craddock, J. Leendertz, A. W. Preece, and R. Benjamin, "Breast cancer detection using symmetrical antenna array," in *Proceedings of the 2nd European Conference on Antennas and Propagation (EuCAP '07)*, pp. 1–5, Edinburgh, UK, November 2007.
- [7] M. Lazebnik, L. McCartney, D. Popovic, et al., "A large-scale study of the ultrawideband microwave dielectric properties of normal breast tissue obtained from reduction surgeries," *Physics in Medicine and Biology*, vol. 52, no. 10, pp. 2637–2656, 2007.
- [8] E. C. Fear, X. Li, S. C. Hagness, and M. A. Stuchly, "Confocal microwave imaging for breast cancer detection: localization of tumors in three dimensions," *IEEE Transactions on Biomedical Engineering*, vol. 49, no. 8, pp. 812–822, 2002.
- [9] E. J. Bond, X. Li, S. C. Hagness, and B. D. Van Veen, "Microwave imaging via space-time beamforming for early detection of breast cancer," *IEEE Transactions on Antennas and Propagation*, vol. 51, no. 8, pp. 1690–1705, 2003.
- [10] R. A. Marr, U. H. W. Lammers, T. B. Hansen, T. J. Tanigawa, and R. V. McGahan, "Bistatic RCS calculations from cylindrical near-field measurements—part II: experiments," *IEEE Transactions on Antennas and Propagation*, vol. 54, no. 12, pp. 3857–3864, 2006.
- [11] I. J. LaHaie and M. A. Blischke, "Mitigation of multipath and ground interactions in RCS measurements using a single target translation," in *Proceedings of the 23rd Annual Meeting of the Antenna Measurement Techniques Association (AMTA '01)*, pp. 411–416, Denver, Colo, USA, October 2001.
- [12] M. Klemm, I. J. Craddock, J. A. Leendertz, A. Preece, and R. Benjamin, "Breast cancer detection using a hemi-spherical

antenna array—experimental results,” submitted to *IEEE Transactions on Antennas and Propagation*.

- [13] W. Shao, B. Zhou, Z. Zheng, and G. Wang, “UWB microwave imaging for breast tumor detection in inhomogeneous tissue,” in *Proceedings of the 27th IEEE Annual International Conference of the Engineering in Medicine and Biology Society (EMBS '05)*, pp. 1496–1499, Shanghai, China, September 2005.
- [14] Z. Wang, J. Li, and R. Wu, “Time-delay- and time-reversal-based robust Capon beamformers for ultrasound imaging,” *IEEE Transactions on Medical Imaging*, vol. 24, no. 10, pp. 1308–1322, 2005.

Research Article

Determination of Bolus Dielectric Constant for Optimum Coupling of Microwaves through Skin for Breast Cancer Imaging

Carey Rappaport

*The Gordon Center for Subsurface Sensing and Imaging Systems (Gordon-CenSSIS),
Northeastern University, Boston, MA 02115, USA*

Correspondence should be addressed to Carey Rappaport, rappaport@neu.edu

Received 2 August 2007; Revised 7 November 2007; Accepted 4 February 2008

Recommended by Elise Fear

We find the complex dielectric constant of the bolus liquid with the best microwave impedance match to skin-covered fatty breast tissue. The real dielectric constant and conductivity of the ideal medium are determined by minimizing the magnitude of the reflection coefficient from the two-interface frequency-dependent system, using published measured skin and breast fat dielectric characteristics in the 400 MHz to 10 GHz frequency range. Error bounds are provided to indicate the coupling degradation when using real, nonideal media for the bolus liquid. Two frequency regimes are identified. Below 6.45 GHz, conventional liquid mixtures can approach the optimal coupling permittivity, but the reflection magnitudes for these best cases are high. Above 6.45 GHz, perfect coupling is possible, but only for impractically high values of bolus dielectric constant and loss.

Copyright © 2008 Carey Rappaport. This is an open access article distributed under the Creative Commons Attribution License, which permits unrestricted use, distribution, and reproduction in any medium, provided the original work is properly cited.

1. INTRODUCTION

In cases where breast tumors occur in fatty healthy breast tissue, microwaves can be used to take advantage of the large dielectric contrast difference between the tumor scatterer and its surrounding background to detect the cancer. Several breast cancer detection systems have been proposed [1–9], each indicating great potential for discriminating the high-water-content tumor volume from the low-water-content fatty surrounding tissue.

One open question is the choice of coupling fluid, often referred to as bolus liquid, which allows the greatest transfer of waves from the antennas through the skin and into the breast tissue. Published work investigating empirically enhancing the coupling with suitable mixtures of glycerin and water [10, 11], indicates that proper choice makes a significant difference in sensing performance.

Although the skin layer is thin (on average, 1.6 mm [12]), it is a high-water-content biological tissue and thus has a significant effect on the coupling into breast tissue. The problem is additionally complicated since all biological tissue is frequency dependent. This paper uses a simple one dimensional impedance model to determine the best bolus complex

dielectric constant necessary to minimize reflection from skin-covered fatty breast tissue and hence transfer the maximum percentage of microwave sensing signal into the breast.

In practice, it may not be possible to obtain a real bolus liquid with the desired dielectric properties across the intended frequency range. However, having the information about the desired complex permittivity characteristics across large frequency ranges provides potential guidance in the selection of bolus liquid.

2. ONE DIMENSIONAL IMPEDANCE MODEL

Since the skin layer covering the internal breast tissue is very thin compared to all other length scales of the problem geometry, it is reasonable to model the wave interaction as a three-layer one-dimensional model. A further simplification considers only normally incident plane waves. While in reality sensing waves are almost never uniform and normally incident on tissue boundaries, this assumption selects the most important of the great number of possible illumination cases.

Following the standard method [13], assume that the bolus with complex permittivity $\epsilon = \epsilon_b \epsilon_0$ fills space to the left

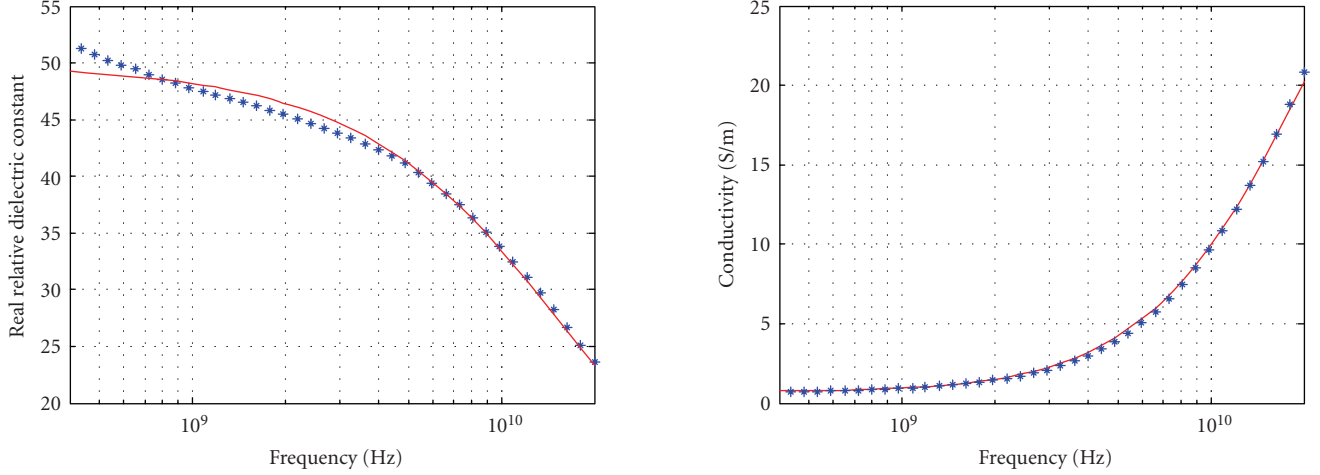


FIGURE 1: Measured (points) [14] and Cole-Cole model fitted (solid curve) dielectric values for wet skin in the microwave frequency range.

TABLE 1: Coefficients for Cole-Cole models of tissues for 400 MHz–20 GHz.

Tissue	ϵ_∞	$\Delta\epsilon_1$	τ_1 (ps)	α_1	σ_s (S/m)
Breast fat	3.145	1.701	14.68	0.05826	0.03605
Wet skin	2.0	48	9.5	0.19	0.710

of the origin, $z < 0$, that fatty breast tissue with $\epsilon = \epsilon_f \epsilon_0$ fills the space to the right of plane at $z = \Delta z$, and that skin with $\epsilon = \epsilon_s \epsilon_0$ occupies the space of thickness Δz between the two. The incident and reflected, right-going and left-going, and transmitted waves in the three layers can be represented as

$$\begin{aligned} E_0 e^{-jk_b z} + \Gamma E_0 e^{+jk_b z}, \\ A E_0 e^{-jk_s z} + B E_0 e^{+jk_s z}, \\ T E_0 e^{-jk_f z}, \end{aligned} \quad (1)$$

where the reflection and transmission coefficients are given by Γ and T , A and B are unknown skin layer coefficients, and $k_b = \omega \sqrt{\mu_0 \epsilon_b \epsilon_0} = k_0 \sqrt{\epsilon_b}$ is the complex wave number for the bolus layer, given in terms of the radian frequency and permeability and permittivity of free space and complex dielectric constant. Similar expressions hold for the wave numbers in the skin and fat layers. Continuity of transverse impedance at the two interfaces results in

$$\begin{aligned} \frac{1 + \Gamma}{1 - \Gamma} \frac{\omega \mu_0}{k_b} &= \frac{A + B}{A - B} \frac{\omega \mu_0}{k_s}, \\ \frac{A e^{-jk_s \Delta z} + B e^{+jk_s \Delta z}}{A e^{-jk_s \Delta z} - B e^{+jk_s \Delta z}} \frac{\omega \mu_0}{k_s} &= \frac{\omega \mu_0}{k_f}. \end{aligned} \quad (2)$$

Solving first for B in the latter equation, substituting it into the former, cancelling the common factor of A , and then solving for the three-layer reflection coefficient yield

$$\Gamma = \frac{e^{jk_s \Delta z} (k_b - k_s) (k_f + k_s) - e^{-jk_s \Delta z} (k_b + k_s) (k_f - k_s)}{e^{jk_s \Delta z} (k_b + k_s) (k_f + k_s) - e^{-jk_s \Delta z} (k_b - k_s) (k_f - k_s)}. \quad (3)$$

The matched case, $\Gamma = 0$, occurs when

$$k_b^{\text{opt}} = k_s \frac{(e^{jk_s \Delta z} - e^{-jk_s \Delta z}) k_s + (e^{jk_s \Delta z} + e^{-jk_s \Delta z}) k_f}{(e^{jk_s \Delta z} + e^{-jk_s \Delta z}) k_s + (e^{jk_s \Delta z} - e^{-jk_s \Delta z}) k_f}. \quad (4)$$

Equation (4) identifies the best bolus dielectric constant, as long as its imaginary part is negative. If it becomes positive, the coupling medium must have gain rather than conductive loss and hence is impractical.

The next step in the modeling process is to specify the wave numbers for the skin and breast fat as functions of frequency. Accurate measurements of these types of tissues have been conducted [14, 15]. The Cole-Cole dispersive medium relation, given by

$$\frac{\epsilon_{f,s}(\omega)}{\epsilon_0} = \epsilon_\infty + \frac{\Delta\epsilon_1}{1 + (j\omega\tau_1)^{-\alpha_1}} + \frac{\sigma_s}{j\omega\epsilon_0}, \quad (5)$$

accurately and compactly matches both the real dielectric constant and the conductivity of a frequency-dependent medium. For breast tissue with 85–100% fat in the 400 MHz to 20 GHz, frequency range [15] has determined coefficients for (5), while for wet skin, one possible model is plotted in Figure 1. Table 1 gives the coefficients for these two models.

3. OPTIMAL DIELECTRIC CONSTANT RESULTS

Inserting the Cole-Cole dielectric models for skin and breast fat into the formulas for the wave numbers and then into (4) and choosing $\Delta z = 1.6$ mm [12] yield optimal values for k_b^{opt} , which can be squared and divided by $\omega^2 \mu_0 \epsilon_0$ to give the complex dielectric constant:

$$\epsilon_b^{\text{opt}}(\omega) = \epsilon'_b(\omega) - j \frac{\sigma(\omega)}{\omega \epsilon_0}. \quad (6)$$

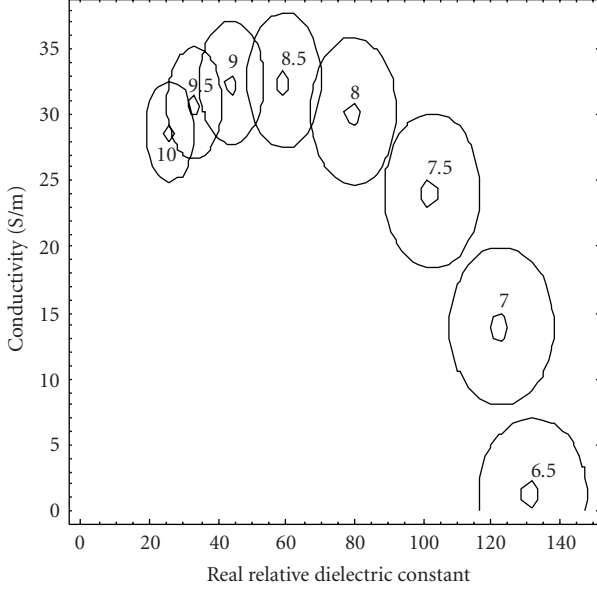


FIGURE 2: Exact complex dielectric values for bolus liquid with perfect match, $|\Gamma| = 0$, and contours of constant reflection magnitude $|\Gamma| = 0.03$ for 6.5 to 10 GHz, in steps of 0.5 GHz.

The values for real relative dielectric constant ϵ'_b and conductivity σ , as a function of frequency, are plotted in Figure 2. For 10, 9.5, 9, 8.5, 8, 7.5, 7, and 6.5 GHz, the points corresponding to the ordered pair (ϵ'_b, σ) for zero reflection, as well as the elliptical contours corresponding to $|\Gamma| = 0.03$ (arbitrarily chosen for graphical clarity) are indicated. The contours give an error bound showing the tolerance about the ideal complex values for liquids with close—but not exact—dielectric matching characteristics. Figure 2 also provides a sense of impedance variation of this three-layer geometry for wideband microwave systems. A bolus liquid which is perfect for one frequency may be considerably mismatched at another.

While the optimal complex permittivity values of Figure 2 provide perfect coupling, they are impractically high, both in real part and in conductivity. Even if such bolus fluids could be found, the propagation loss from antenna to skin would eliminate any coupling advantages. Extending the reflection magnitude contours to larger values and into the more physically realizable permittivity parameter space requires separate plots for each frequency. This set is shown in Figure 3, for reflection magnitudes of 0.1, 0.15, and 0.2, for 6.5 to 10 GHz. Also indicated in Figure 3 are the asymptotes that define the limits of reflection magnitude. For different frequencies, there are bolus fluids with ϵ'_b and σ combinations that result in greater reflection, but for ϵ'_b and σ combinations to the left and below a given asymptote, no frequency choice will couple with lower reflection than that asymptote value. Observing the plots of Figure 3 leads to simple rules for improving coupling to breast tissue.

- (1) For frequencies above 9.5 GHz, increase σ and reduce ϵ'_b .
- (2) Between about 8 and 9.5 GHz, just increase σ .

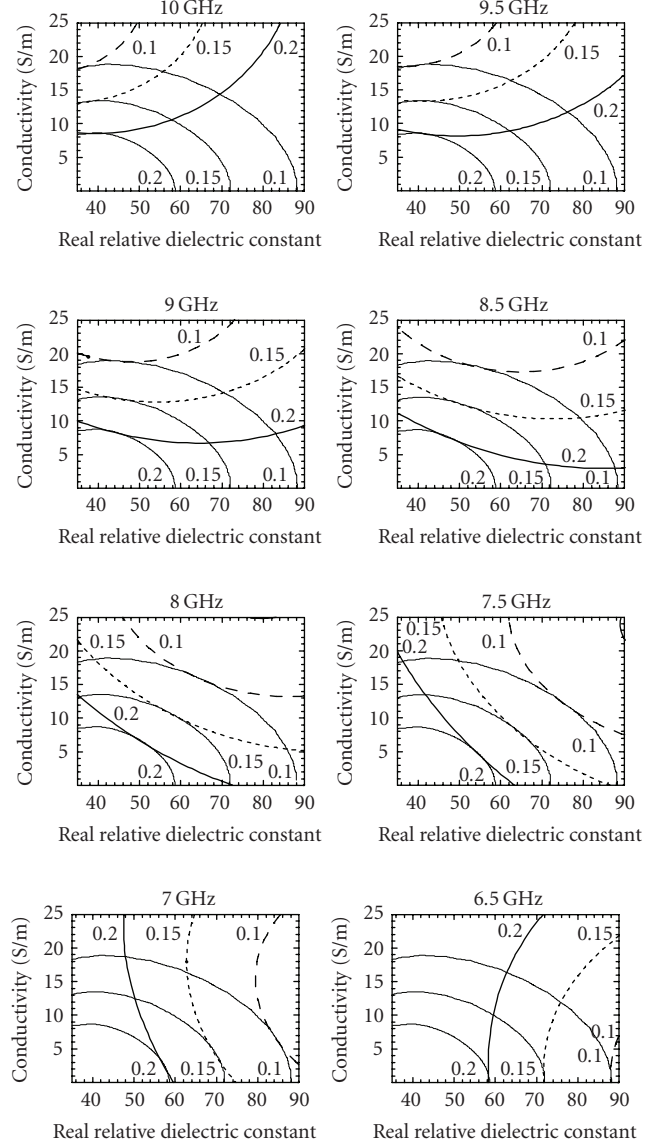


FIGURE 3: Contours of constant reflection magnitude $|\Gamma| = 0.1$ (dashed curves), 0.15 (dotted curves), and 0.2 (solid curves) as indicated, for frequencies: 10.0, 9.5, 9.0, 8.5, 8.0, 7.5, 7.0, and 6.5 GHz, as well as the common asymptotes for $|\Gamma| = 0.1, 0.15,$ and 0.2, for practical values of bolus complex permittivity. The curve contours are extended from the centers shown in Figure 2.

- (3) Between 7 and 8 GHz, increase ϵ'_b and σ .
- (4) Between 6.5 and 7 GHz, increase ϵ'_b and reduce σ .

Just below 6.5 GHz, the imaginary part of the optimal wave number (4) becomes positive, which makes the conductivity given by (6) negative. For these cases, the best bolus liquid is a pure dielectric with zero conductivity. Contours of constant reflection magnitude, given by (3) with k_b kept purely real, are plotted in Figure 4. The best dielectric constant for any particular frequency is found by picking the darkest contour (the lowest reflection magnitude level) crossed by the vertical line through that frequency and associating the dielectric constant at the crossing. The white

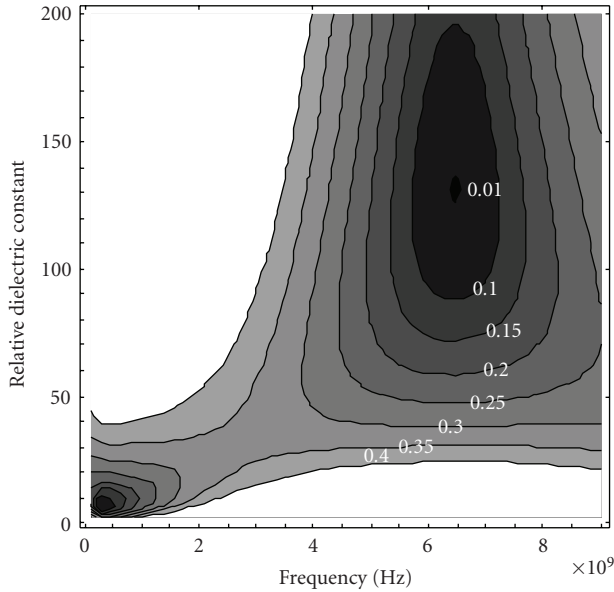


FIGURE 4: Contours of constant reflection magnitude for lossless bolus matching to skin-covered fatty breast tissue. A perfect match occurs at 6.45 GHz for a pure dielectric bolus with dielectric constant of 135. The worst coupling occurs at 2.67 GHz, with reflection coefficient of 0.34 for the best choice dielectric constant $\epsilon' = 30.4$.

regions of Figure 4 correspond to $|\Gamma| > 0.4$. Both the minimum reflection magnitudes and their variation with dielectric constant are much greater than those for frequencies above the critical value, found numerically to be 6.45 GHz.

For frequencies below 1 GHz or above 5 GHz, the optimal reflection magnitude is below 0.2 for bolus dielectric constants of about 10 and 100, respectively. However, in the diagnostically useful frequency range of 2–4.5 GHz, the reflection magnitude cannot be reduced below 0.3 for *any* choice of matching fluid.

For real liquids with nonzero conductivity, Figure 5 indicates the error bounds about the ideal dielectric choice. Each contour indicates the region of possible combinations of real dielectric constant and conductivity which would result in reflection magnitudes not more than 30% above the ideal value for that frequency. The horizontal maximum widths of the contours correspond to the vertical elongation of the contours of Figure 4. Note that while there is considerable tolerance for dielectric characteristics for 5.0 GHz, this is due to the reflection magnitude contour of Figure 4 being quite long in the vertical direction.

The lowest frequency range is examined in detail in Figure 6, which shows several common reflection magnitude contours for 400 MHz (solid curves), 900 MHz (dotted curves), and 1.3 GHz (dashed curves) reflection magnitude contours of 0.25, 0.4, and 0.55. Labeled points indicate particular bolus fluids: W1: water at 300 MHz, W2: water at 3 GHz, S1: 0.1 molal saline at 300 MHz, S2: 0.1 molal saline at 3 GHz, S3: 0.3 molal saline at 300 MHz [16], S4: 0.15 molal (0.9%) saline at 900 MHz, G1: 10 : 30 glycerin/water at 900 MHz, G2: 80 : 20 glycerin/water at 900 MHz, G3: 87 : 13 glycerin/water at 900 MHz, G4: 79 : 21 glycerin/water at 1.3 GHz, and G5: 87 : 13 glycerin/water at 1.3 GHz [11].

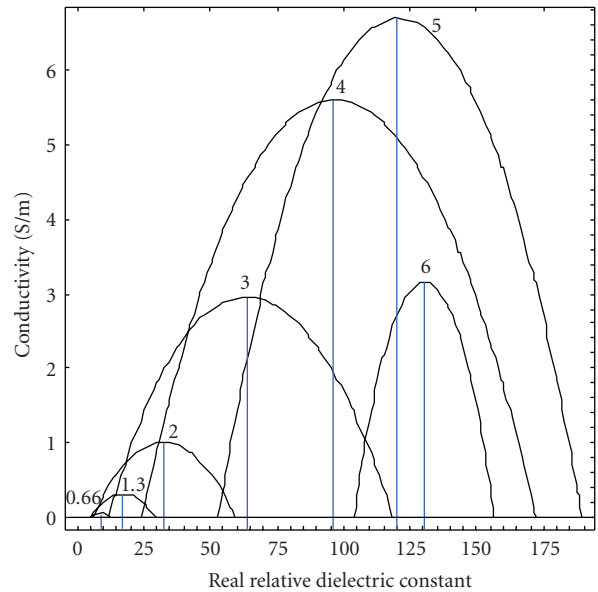


FIGURE 5: Contours of constant reflection magnitude at levels 30% above the best level determined for pure dielectric with no loss, for frequencies: 0.667, 1.33, 2.0, 3.0, 4.0, 5.0, and 6.0 GHz, as indicated on each curve on the figure. The 30% increased reflection contours have values: 0.17, 0.34, 0.42, 0.435, 0.37, 0.246, and 0.08, respectively. The optimal match dielectric constant for each frequency is indicated by the vertical line from the contour peak to the horizontal axis.

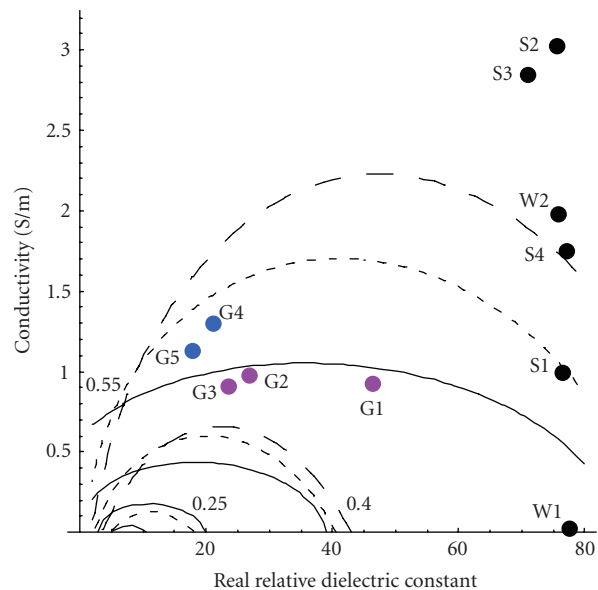


FIGURE 6: Low-frequency detail of Figure 5, for 400 MHz (solid curves), 900 MHz (dotted curves), and 1.3 GHz (dashed curves) reflection magnitude contours of 0.25, 0.4, and 0.55. Labeled points indicate particular bolus fluids: W1: water at 300 MHz, W2: water at 3 GHz, S1: 0.1 molal saline at 300 MHz, S2: 0.1 molal saline at 3 GHz, S3: 0.3 molal saline at 300 MHz [16], S4: 0.15 molal (0.9%) saline at 900 MHz, G1: 10 : 30 glycerin/water at 900 MHz, G2: 80 : 20 glycerin/water at 900 MHz, G3: 87 : 13 glycerin/water at 900 MHz, G4: 79 : 21 glycerin/water at 1.3 GHz, and G5: 87 : 13 glycerin/water at 1.3 GHz [11].

4. CONCLUSION

This analysis has determined the best dielectric constant and conductivity characteristics for a bolus liquid to match to skin-covered fatty breast tissue for microwave in the 400 MHz to 10 GHz frequency range. The results are based on a simple 1D plane-wave model, using accurate frequency dependent measurements of dielectric characteristic of skin and breast fat.

Above 6.45 GHz, specific bolus dielectric values can match exactly to the skin/breast layers, although their dielectric constants and conductivities must be very high, in the 5–30 S/m range. About 10% variation in real dielectric constant and 15% in conductivity result in reflection magnitudes of only 0.03. Although the optimal values are impractical for typical liquids, they indicate the directions in complex permittivity space that bolus fluids should approach to increase coupling efficiency. The contours for larger reflection magnitudes of 0.1, 0.15, and 0.2 extend into permittivity values typical of water-mixture bolus fluids.

Below 6.45 GHz, the best bolus dielectric constants are purely real, and the lowest possible reflections magnitudes are as high as 0.34 for 2.67 GHz. For practical liquids with moderate conductivity, the reflection magnitude increases slowly, with only 30% reflection increase for liquids with 6.5 S/m at 5 GHz, or 0.17 S/m at 1.33 GHz. Thus, there is much greater tolerance for variation of real dielectric constant and conductivity from the optimal values for bolus fluids below 6.45 GHz, but the reflection magnitudes are considerably higher than for frequencies above 6.45 GHz.

ACKNOWLEDGMENTS

This work is supported by CenSSIS, the Gordon Center for Subsurface Sensing and Imaging Systems, under the ERC Program of the NSF (Award no. EEC-9986821). The author is indebted to Ann Morgenthaler for helpful discussions.

REFERENCES

- [1] P. M. Meaney, M. W. Fanning, D. Li, S. P. Poplack, and K. D. Paulsen, "A clinical prototype for active microwave imaging of the breast," *IEEE Transactions on Microwave Theory and Techniques*, vol. 48, no. 11, pp. 1841–1853, 2000.
- [2] K. Paulsen, P. Meaney, and L. Gilman, *Alternative Breast Imaging*, vol. 778 of *Kluwer International Series in Engineering and Computer Science*, Springer, Dordrecht, The Netherlands, 2005.
- [3] E. C. Fear, X. Li, S. C. Hagness, and M. A. Stuchly, "Confocal microwave imaging for breast cancer detection: localization of tumors in three dimensions," *IEEE Transactions on Biomedical Engineering*, vol. 49, no. 8, pp. 812–822, 2002.
- [4] T. C. Williams, E. C. Fear, and D. T. Westwick, "Tissue sensing adaptive radar for breast cancer detection—investigations of an improved skin-sensing method," *IEEE Transactions on Microwave Theory and Techniques*, vol. 54, no. 4, pp. 1308–1313, 2006.
- [5] F. Qianqian, P. M. Meaney, and K. D. Paulsen, "Microwave image reconstruction of tissue property dispersion characteristics utilizing multiple-frequency information," *IEEE Transactions on Microwave Theory and Techniques*, vol. 52, no. 8, pp. 1866–1875, 2004.
- [6] X. Li, S. K. Davis, S. C. Hagness, D. W. van der Weide, and B. D. Van Veen, "Microwave imaging via space-time beamforming: experimental investigation of tumor detection in multi-layer breast phantoms," *IEEE Transactions on Microwave Theory and Techniques*, vol. 52, no. 8, pp. 1856–1865, 2004.
- [7] Z. Q. Zhang, Q. H. Liu, C. Xiao, E. Ward, G. Ybarra, and W. T. Joines, "Microwave breast imaging: 3-D forward scattering simulation," *IEEE Transactions on Biomedical Engineering*, vol. 50, no. 10, pp. 1180–1189, 2003.
- [8] P. Kosmas, C. M. Rappaport, and E. Bishop, "Modeling with the FDTD method for microwave breast cancer detection," *IEEE Transactions on Microwave Theory and Techniques*, vol. 52, no. 8, pp. 1890–1897, 2004.
- [9] P. Kosmas and C. M. Rappaport, "FDTD-based time reversal for microwave breast cancer detection-localization in three dimensions," *IEEE Transactions on Microwave Theory and Techniques*, vol. 54, no. 4, pp. 1921–1923, 2006.
- [10] P. M. Meaney, S. A. Pendergrass, M. W. Fanning, and K. D. Paulsen, "Importance of using a reduced contrast coupling medium in 2D microwave breast imaging," *Journal of Electromagnetic Waves and Applications*, vol. 17, no. 2, pp. 333–355, 2003.
- [11] P. M. Meaney, M. W. Fanning, T. Reynolds, et al., "Initial clinical experience with microwave breast imaging in women with normal mammography," *Academic Radiology*, vol. 14, no. 2, pp. 207–218, 2007.
- [12] R. Moore and D. Kopans, "Private communication, based on x-ray tomosynthesis measurements," July 2007.
- [13] D. Staelin, A. Morgenthaler, and A. Kong, *Electromagnetic Waves*, Prentice-Hall, Englewood Cliffs, NJ, USA, 1994.
- [14] S. Gabriel, R. W. Lau, and C. Gabriel, "The dielectric properties of biological tissues: II. Measurements in the frequency range 10 Hz to 20 GHz," *Physics in Medicine and Biology*, vol. 41, no. 11, pp. 2251–2269, 1996.
- [15] M. Lazebnik, L. McCartney, D. Popovic, et al., "A large-scale study of the ultrawideband microwave dielectric properties of normal breast tissue obtained from reduction surgeries," *Physics in Medicine and Biology*, vol. 52, no. 10, pp. 2637–2656, 2007.
- [16] A. von Hippel, *Dielectric Materials and Applications*, Artech House, Boston, Mass, USA, 1953.

Research Article

Characterization of an Implicitly Resistively-Loaded Monopole Antenna in Lossy Liquid Media

Colleen J. Fox, Paul M. Meaney, Fridon Shubitidze, Lincoln Potwin, and Keith D. Paulsen

Thayer School of Engineering, Dartmouth College, Hanover, NH 03755, USA

Correspondence should be addressed to Paul M. Meaney, paul.meaney@dartmouth.edu

Received 7 September 2007; Accepted 18 January 2008

Recommended by Elise Fear

Microwave tomographic imaging of the breast for cancer detection is a topic of considerable interest because of the potential to exploit the apparent high-dielectric property contrast between normal and malignant tissue. An important component in the realization of an imaging system is the antenna array to be used for signal transmission/detection. The monopole antenna has proven to be useful in our implementation because it can be easily and accurately modeled and can be positioned in close proximity to the imaging target with high-element density when configured in an imaging array. Its frequency response is broadened considerably when radiating in the liquid medium that is used to couple the signals into the breast making it suitable for broadband spectral imaging. However, at higher frequencies, the beam patterns steer further away from the desired horizontal plane and can cause unwanted multipath contributions when located in close proximity to the liquid/air interface. In this paper, we have studied the behavior of these antennas and devised strategies for their effective use at higher frequencies, especially when positioned near the surface of the coupling fluid which is used. The results show that frequencies in excess of 2 GHz can be used when the antenna centers are located as close as 2 cm from the liquid surface.

Copyright © 2008 Colleen J. Fox et al. This is an open access article distributed under the Creative Commons Attribution License, which permits unrestricted use, distribution, and reproduction in any medium, provided the original work is properly cited.

1. INTRODUCTION

Microwave imaging techniques have been investigated for biomedical applications for nearly three decades, but have received renewed interest because of their potential in breast imaging based on data which have shown significant property contrast between normal and malignant tissue [1–3]. Their exploration is particularly timely given the well documented limitations of X-ray mammography which is the standard of care for breast cancer screening in most developed countries [4]. While there have been several early reports on microwave radiometry as a detection scheme that exploits the elevated temperatures of tumors [5–7], more recent investigations have focused on tomographic and ultra-wideband (UWB) radar approaches [8–17].

The UWB radar methods are intriguing because they may be able to capitalize on the considerable advances in microwave technology for UWB communications. Indeed, simulations have shown that detection of tumors as small as 2-3 mm in diameter may be possible [10, 18]. In practice, implementation may prove to be more challenging because wideband antennas are typically large (i.e., spiral antennas

or resistively loaded in which case they often have very low efficiency that limits signal penetration depth for tumor detection [19–21], although novel antenna designs that are not resistively loaded but offer good efficiency over a narrower frequency band have been identified [19].

In terms of tomographic approaches, while there has been a considerable amount of numerical modeling [9, 14, 16, 17, 22, 23], only a few systems have been developed for phantom experiments [24–26] and for actual breast imaging [13, 15]. Similarly to the radar methods, one of the important considerations is the antenna design. Some systems (e.g., Semenov et al. [26]) have utilized waveguide radiators positioned on a large diameter whereas others have implemented monopole antennas [13, 15]. These antennas are submerged in lossy liquids (either saline or glycerin-water mixtures) and subsequently are resistively loaded and also have the associated efficiency degradation, although experience has shown that transmitted signals can still be detected down to roughly -140 dBm with well-designed, low-noise receivers [27].

The coaxial monopole antenna is attractive for microwave breast imaging because its size and shape allow it to be densely packed around an imaging target. The design,

constructed by removing a length of the outer conductor at one end of a rigid coaxial cable, is simple and low cost. In general, the monopole has a relatively narrow bandwidth and excites surface currents along its outer conductor [28, 29] in air where it closely resembles a dipole when baluns and/or notched outer conductors are applied [30]. However, when placed in a lossy medium the behavior changes dramatically, and its bandwidth increases significantly with the associated resistive loading. Additionally, we have found that the rigid coaxial cable interfaces well with an imaging configuration where liquid coupling and vertical positioning are required.

The goal of this investigation is to assess monopole antenna performance. Of particular concern has been the measurement behavior when the antennas approach the liquid surface. Images near the surface correspond to planes closest to the chest wall for breast exams and are important given the relatively high-cancer incidence in the axilla region which is adjacent to the chest wall. When the antennas are fully submerged in a homogeneous coupling bath, the measurement magnitudes generally decrease monotonically as a function of the distance between transmit and receive antennas [27]. However, this pattern degrades progressively as the antennas approach the liquid surface and is most pronounced for the higher end of our operating frequency range (generally above 1500 MHz). As a result, we have investigated the characteristics of these antennas with respect to the most readily available parameters—composition of the coupling bath and antenna length—in order to devise strategies for improving overall performance. In general, we have found strong correlations between the return loss, the effective beam width, and beam steering angle as a function of antenna electrical length which is consistent over multiple bath compositions (i.e., with significantly different permittivity and conductivity). In addition, these measurements are consistent with trends observed in associated simulation results. Based on these studies, we have optimized the antenna design to allow operation relatively close to the liquid surface over the upper end of our operating frequency range.

2. METHODS

Our breast imaging system operates in a range of liquid coupling solutions with varying electrical permittivities to improve the dielectric property match to specific breast density types. Previous results have demonstrated significant variations in permittivity and conductivity as a function of breast density [31] primarily due to the overall higher-water content of the fibroglandular tissue compared with fat [32–34]. Breast types vary over a continuum from fatty (mostly adipose tissue) to extremely dense (mostly fibroglandular tissue) [35]. In light of the variations in breast parenchymal density, we present data for multiple bath compositions in order to illustrate the consistency of our techniques. We refer the interested reader to previous publications for a detailed description of our clinical breast imaging system [13, 27].

2.1. Data calibration

As part of the calibration procedure for our breast imaging system, a set of measurement data is acquired for the ho-

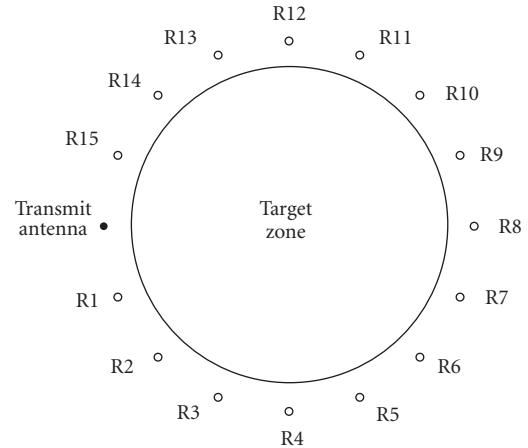


FIGURE 1: 2D schematic diagram of the 16 monopole antennas arranged in a 15.2 cm diameter circular array surrounding the imaging zone.

mogeneous bath for all operating frequencies and all possible permutations of transmit and receive antennas. Figure 1 shows the circular antenna array configuration used during breast imaging exams. Beyond minor interreceiver channel gain variations, the magnitudes exhibit a predictable behavior for a given transmitter where power levels decrease monotonically with distance. Figures 2(a) and 2(b) show the amplitude measurements with respect to receiver antenna number for a single transmitter over a range of frequencies for the cases of the array: (a) at its maximum depth below the 87 : 13 glycerin-water bath surface (position 7), and (b) with the antenna centers just 2 cm below the liquid surface (position 1). Note that all 16 antennas in the array are positioned on a 15.2 cm diameter circle with an orientation such that relative receivers 1 and 15 are adjacent to the transmitter while receiver 8 is furthest away. The plots for frequencies from 500 to 1700 MHz in Figure 2(a) suggest a monotonic signal decrease with respect to transmitter/receiver separation distance. However, the corresponding curves in Figure 2(b) exhibit significant variations primarily at the higher frequencies and for the larger antenna separations. Given that the only difference between the two cases is the depth of the antennas below the liquid surface, the most likely explanation is that unwanted multipath signals (related to coupling at the bath/air interface) are causing the perturbations.

2.2. Beam characterization

The horizontal beam pattern of a monopole antenna is isotropic due to its radial symmetry; however, the vertical pattern in a lossy solution is considerably more complex. The goal of the first set of experiments was to characterize the vertical plane beam width and beam center with respect to wavelength. This was accomplished by transmitting from a single, vertically oriented, monopole antenna and recording the amplitudes measured by a receiving waveguide antenna at different vertical positions. A waveguide antenna was useful in this

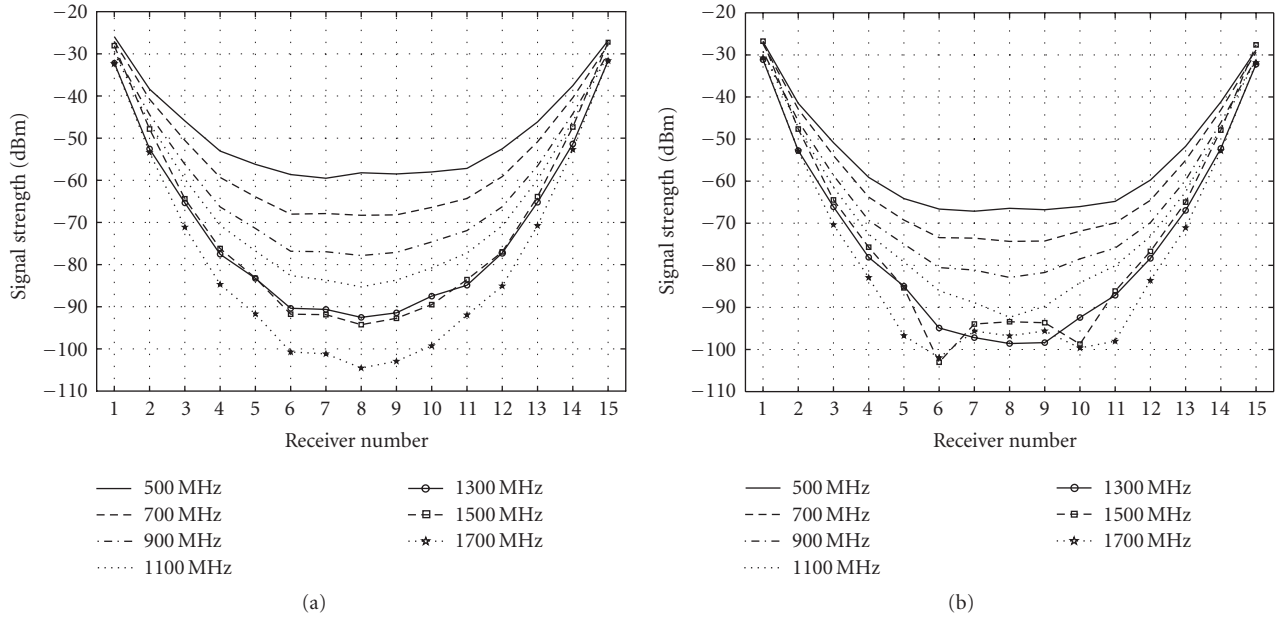


FIGURE 2: Signal amplitude versus relative receiver number associated with a single transmitting, 3.4 cm long antenna for a range of frequencies when the antenna center is submerged (a) 10 cm and (b) 2 cm below the 87% glycerin coupling liquid surface, respectively.

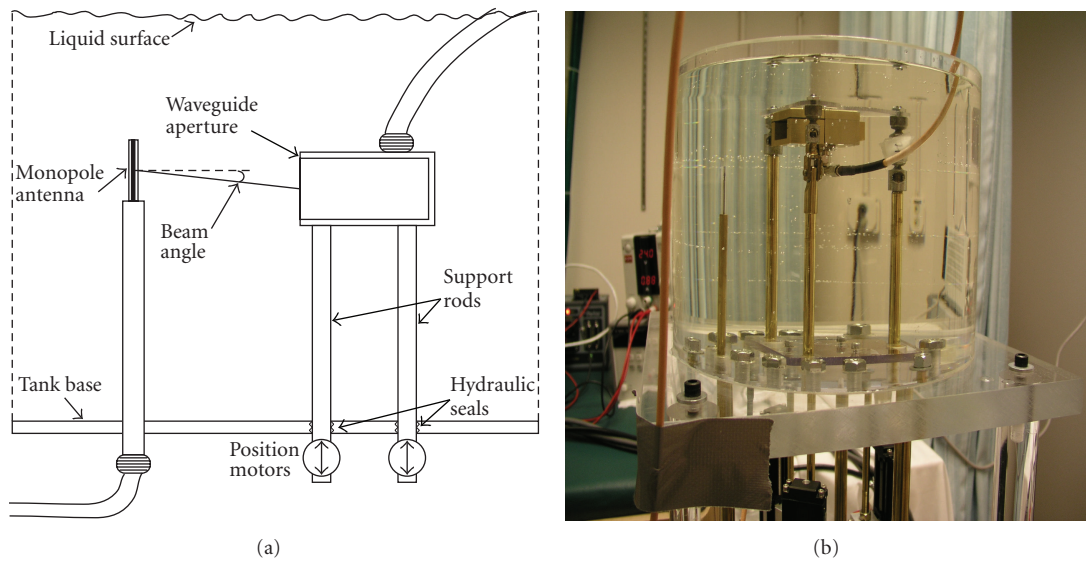


FIGURE 3: (a) Schematic diagram and (b) photograph of the setup for beam pattern measurement involving a 3-point support (3PS) mechanical steering system with the aperture reference waveguide antenna positioned approximately 6 cm from the monopole transmitter.

role because of its beam symmetry in the E-plane. The main variables in the investigation were the signal wavelength in the medium and the relative vertical position of the reference (waveguide) antenna. Secondary variables included the coupling medium and the length of the transmitting (monopole) antenna.

A 3-point support (3PS) mechanical steering system, developed by Meaney et al. [36], was used to position the reference antenna during these studies. Figures 3(a) and 3(b) show a schematic diagram and photograph of the 3PS system configured for the experiments. The waveguide was oriented

perpendicularly to the axis of the monopole and was translated in vertical steps of 2.5 mm under computer control. We did not rotate the reference waveguide about the antenna under test as would be the case in more traditional beam characterization measurements because of the symmetry of the experiments and the logistical challenges of acquiring data in the lossy liquid bath.

The cylindrical testing tank was filled with a lossy glycerin and water solution similar to that used in clinical breast imaging. Measurements were taken in a 90% glycerin, 10% water solution and a 40% glycerin, 60% water solution to

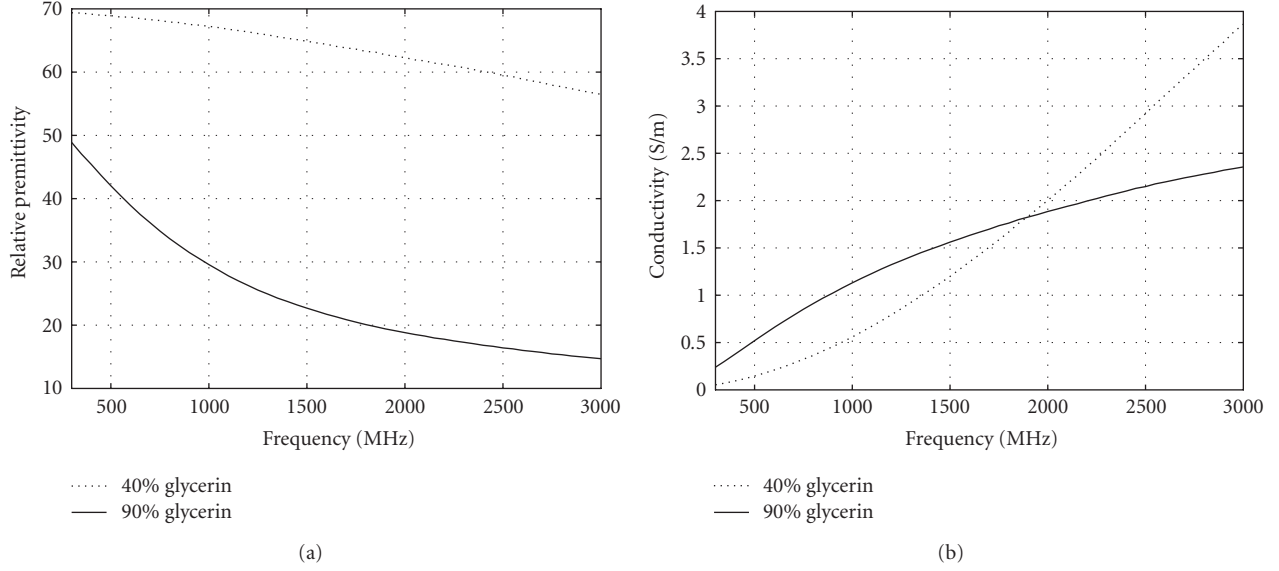


FIGURE 4: The measured (a) relative permittivity and (b) conductivity of the 90% and 40% glycerin: water baths used in these experiments.

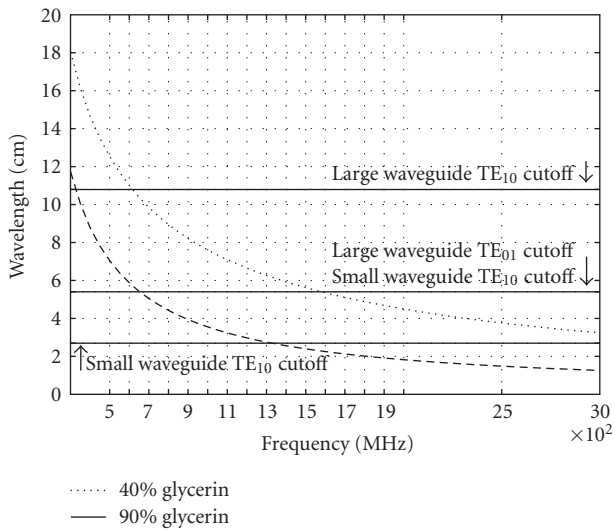


FIGURE 5: Plot of wavelength versus frequency for the 90% and 40% glycerin solutions along with the TE₁₀ cutoff wavelengths for the receiving waveguides.

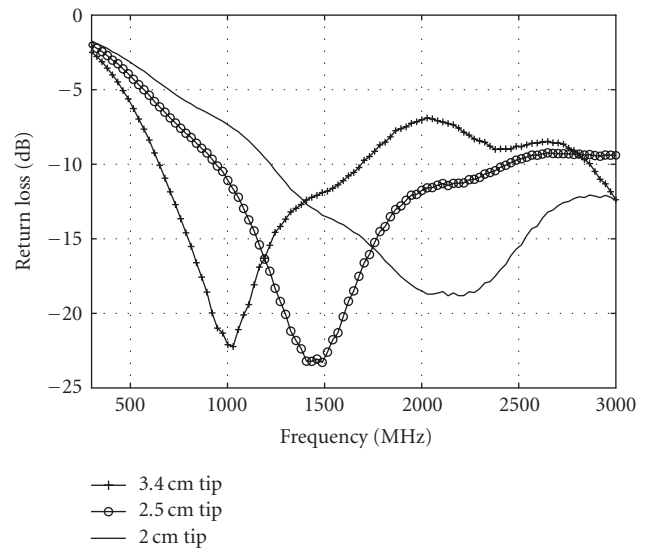


FIGURE 6: Measured return loss of the 2.0, 2.5, and 3.4 cm length monopole antennas in the 90% glycerin: water bath as a function of frequency.

provide a range of complex permittivity values and resulting wavelengths similar to those observed in biological tissue. All measurements were collected using an Agilent 8753C network analyzer in sweep mode with a frequency range of 300 MHz to 3 GHz.

Two complementary waveguide apertures were required to span the full frequency range of the monopole antennas under test. The operational wavelength cutoff for the waveguides was calculated using 1 [29, 37]:

$$\lambda_c = \frac{2}{\sqrt{(m/a)^2 + (n/b)^2}} \text{TE}_{10} \cdot 2a, \quad (1)$$

where m and n are the mode indices, and a and b are the larger and smaller inner dimensions of the front face of the waveguide, respectively. The TE₁₀ mode results in the lowest cutoff frequency and determines the lower operational limit of the waveguide. In this situation, the wavelength for a TE₁₀ mode wave decreases to two times the width. Table 1 shows the dimensions of both receiving waveguide apertures along with their corresponding cutoff wavelengths. The dielectric properties for the 90% and 40% glycerin-water baths are shown in Figure 4. Given that these waveguide antennas were filled with the surrounding liquid, and that the complex permittivity of the glycerin-water solutions varied with frequency, it is instructive to plot the propagation wavelengths

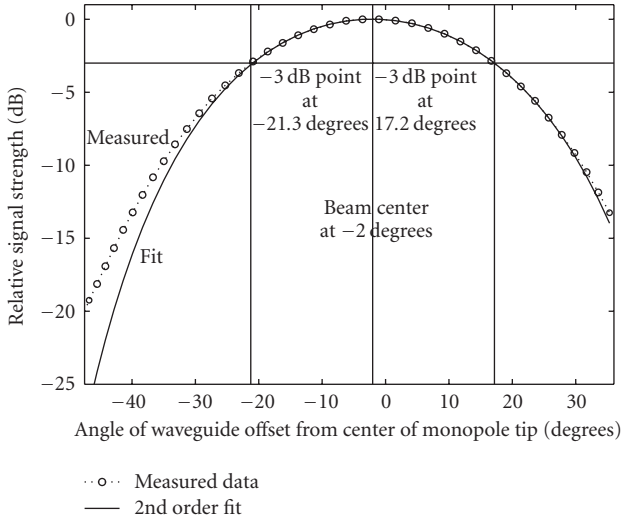


FIGURE 7: Vertical beam pattern for the 3.4 cm length monopole antenna at 1596 MHz in a 90% glycerin: water bath. A 15-point 2nd order polynomial was used to estimate the beam center location and is also shown along with the points 3 dB below the peak value.

TABLE 1: Reference waveguide antenna dimensions and cutoff wavelengths.

Waveguide	Width, a (cm)	Height, b (cm)	Cutoff λ , $2a$ (cm)
Large	5.4	2.7	10.8
Small	2.7	1.4	5.4

for both solutions versus frequency along with horizontal lines corresponding to the cutoff wavelengths of the waveguides (Figure 5). The points where the curves intersect indicate the TE_{10} and TE_{01} mode cutoff frequencies as the lower and upper operating frequency bounds, respectively. From this graph, it is evident that the large and small waveguides can be used from 610 to 1580 MHz and from 1580 to greater than 3000 MHz, respectively, in the 90 : 10 glycerin-water bath. Likewise, for the 40 : 60 glycerin-water bath, the large and small waveguides can be used from 330 to 660 MHz and from 660 to 1270 MHz, respectively.

2.3. Antenna modeling

In addition to the measurements used to characterize these antennas, we have also performed a series of numerical simulations that exhibited comparable behavior. For this modeling, we utilized a finite difference time domain (FDTD) approach in a cylindrical coordinate system which incorporated a rigid 50Ω coaxial feed line along with the geometry of the antenna radiating a lossy, semi-infinite medium [38]. The source was setup to excite only a transverse magnetic field in the coaxial line. The inner and outer conductors of the coaxial cable were represented through perfect electrical conducting (PEC) boundary conditions. The coaxial line dielectric was assumed to be lossless with a relative permittivity of 2.0, and the spatial resolution of the grid was estab-

lished to represent accurately the vertical and radial components of the electric field within the coaxial cable. The dielectric properties of the surrounding bath were the same as those of the medium used in the measurements with the simulations being performed individually at each frequency due to the property dispersion over this range. Eight layers of a perfectly matching layer (PML) were used to minimize backscattered signals from the finite termination of the computational mesh [39]. The simulations were run until the solution had stabilized, after which a Fourier transform was performed at each of the measurement sites to recover the steady-state field values. Similarly to the actual measurements, the z -component of the electric field values was computed at a series of points along a vertical line parallel to the center of the monopole antenna in 3 mm increments.

3. RESULTS AND DISCUSSION

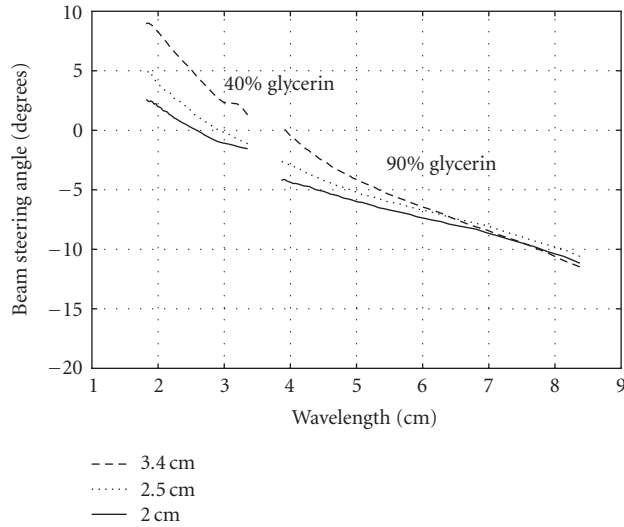
In this section, we first report on the general characteristics of the monopole antennas in terms of their return loss and beam characteristics (steering angle and beamwidth). We then illustrate deviations in the transmit data for antenna positions near the liquid surface for different tip lengths which demonstrate how the overall antenna performance can be improved.

3.1. Return loss

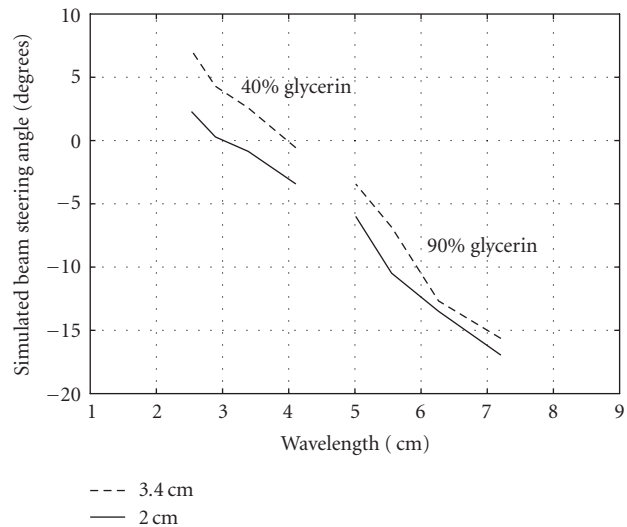
The basic monopole antenna consisted of a 50Ω rigid coaxial cable with the outer conductor stripped from the transmitting zone. Tip lengths of 2.0, 2.5, and 3.4 cm were tested with each having broad operating bandwidths associated with return losses nominally of less than -10 dB across the band for both the 90% and 40% liquid coupling mixtures (plots of the return losses for the 90% glycerin bath are shown in Figure 6). As expected, the dominant null in the return loss associated with the resonant frequency shifts upwards as the length of the transmitting tip decreases—3.4 cm length at 1 GHz, 2.5 cm length at 1.45 GHz, and the 2.0 cm length at 2.15 GHz. The lower-frequency limit also shifts upwards with antenna length. At the higher end of this frequency span, the resistive loading of the antennas generally suppresses the return loss to -10 dB or less.

3.2. Beam characterization

Figure 7 shows a plot of the beam pattern for the 3.4 cm length monopole antenna in the 90% bath at 1596 MHz as a function of the angle between the monopole antenna and the reference waveguide antenna (0 degree was the horizontal plane cutting through the center of the monopole antenna) with the 3 dB points indicated on either side of the beam peak. A second-order polynomial fit to the beam pattern was superimposed to estimate the beam center location—only the 15 points near the beam center were used in the



(a) Beam steering angles for the 2.0, 2.5, and 3.4 cm length monopole antennas as a function of the medium wavelength for the 90% and 40% glycerin: water baths



(b) Same as Figure 8(a) for simulation results of beam steering angles for the 2.0 and 3.4 cm length monopole antennas operating in the 90% and 40% glycerin: water baths

FIGURE 8

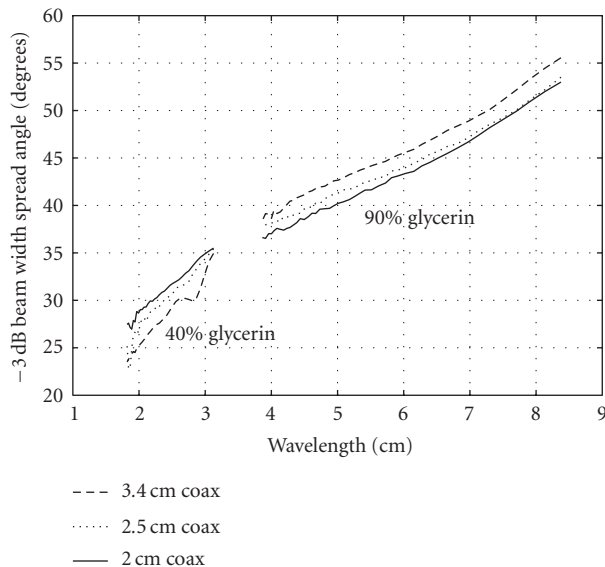


FIGURE 9: Beam widths for the 2.0, 2.5, and 3.4 cm length monopole antennas as a function of the medium wavelength for the 90% and 40% glycerin: water baths.

least squares fitting process. The beam center was readily extracted from the equation of the fitted curve. In terms of the 3 dB beam width, measurement points were selected which straddled the 3 dB-power level below the peak in the beam pattern. From these two points, an interpolation was used to determine the closest position that would be exactly 3 dB below the peak.

Figure 8(a) shows plots of the beam center angle as a function of wavelength in the medium for the three antenna lengths in the two glycerin-water baths (90% and 40%). (The vertical positions of the beam centers have been converted to

beam angles.) The trends in these cases are clear. The beam steers increasingly upwards with decreasing operating wavelength (or increasing frequency). From these curves, it is evident that the beam steering is a function of antenna electrical length in the medium—longer lengths correspond to higher beam steering angles. These trends are echoed in the simulation results for the longest and shortest antenna lengths in the two electrically distinct baths shown in Figure 8(b). The computed behavior matches the measurement observations best at the higher frequencies of concern (i.e., where the beam steers upwards) and supports the validity of the measured behavior. Although the overall response with respect to the antenna lengths and bath properties is consistent between the experimental and simulated data at the longer wavelengths (lower frequencies), the simulated results suggest a more rapid downward steering effect as the wavelength lengthens than was found to occur with the actual measurement data.

Figure 9 shows the corresponding 3 dB beamwidths for the three different length monopole antennas in both the 90% and 40% glycerin-water baths as a function of medium wavelength. In general, the beamwidths increase significantly with wavelength and with different coupling baths (which also directly affects the bath wavelength). To a lesser degree, the beamwidth also appears to be a function of the antenna length. For the 90% bath, the beamwidth increase from the 2.0 to 3.4 cm length antenna is 2.5 degrees across the range of medium wavelengths. Interestingly, the effect for the 40% glycerin-water bath appears to be reversed with the beamwidths for the 2.0 cm monopole being broader than its 3.4 cm length counterpart. Given that the baths we typically use for breast imaging range from 79% to 90%, the results from the 90% bath are more relevant. While beams steer higher with increasing frequency (potentially exacerbating the problem of the fields coupling to the liquid-air

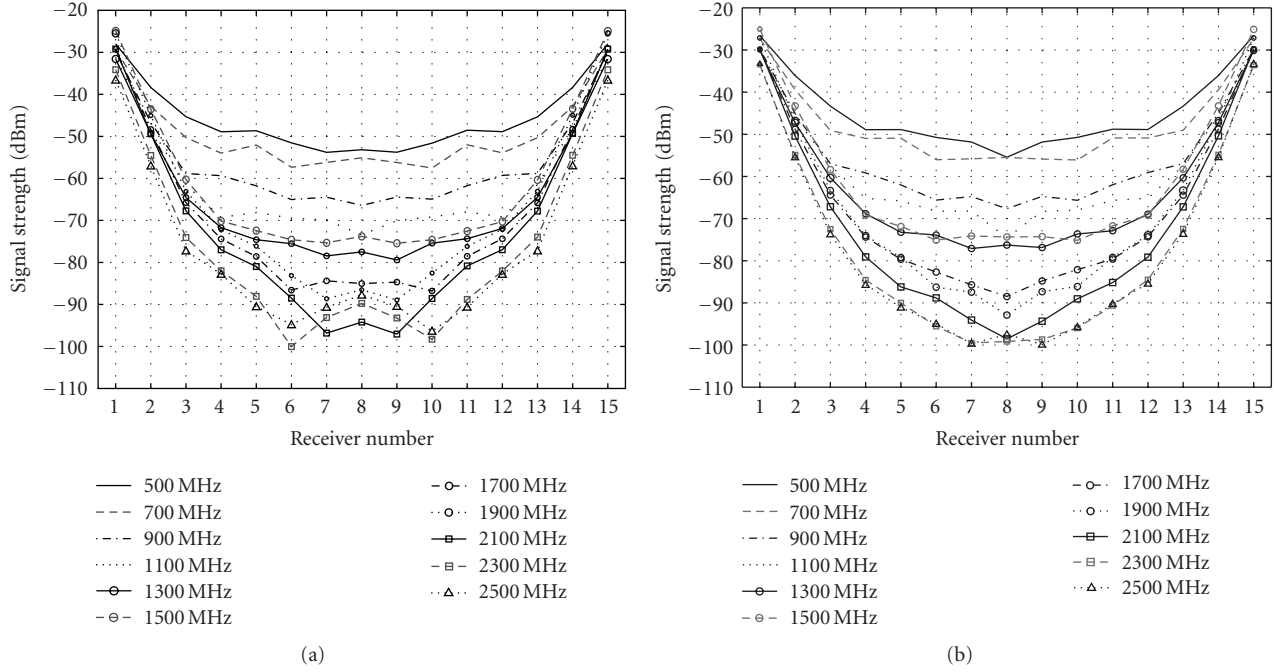


FIGURE 10: Plots of the transmitted signal strength as a function of receiver number over the frequency range of 500–2500 MHz for the 3.4 cm length antennas with their centers submerged (a) 2.0 cm and (b) 6.5 cm below the 90% glycerin coupling liquid surface, respectively.

interface), the beamwidth narrows some with a shorter antenna length which counteracts the coupling effects at the liquid interface. Thus, it appears that a reduced antenna length causes the beam to steer lower while also slightly reducing the beamwidth.

3.3. Multifrequency transmission characteristics

Figure 10 shows transmission data from a single 3.4 cm length monopole to the corresponding receiver monopole antennas in the 90% glycerin bath for frequencies ranging from 500 to 2500 MHz at antenna center depths of (a) 2.0 and (b) 6.5 cm below the liquid surface, respectively. For the deeper position, the shapes of the curves are nearly parabolic with the greater transmission loss corresponding to the greater propagation lengths (especially receiver antennas 7, 8, and 9). (Note that the array has 16 antennas evenly spaced in a circular arrangement). However, in the shallower case, the near-parabolic patterns are noticeably perturbed for the furthest receivers at frequencies above 1900 MHz. These aberrations are due to signals coupling to the liquid surface and propagating along an undesired, low loss surface path.

Figures 11(a) and 11(b) show the corresponding plots for the 2.0 cm length antennas. In this situation there appears to be a minor perturbation in the 2300 MHz case and a more pronounced effect at 2500 MHz. These results are important because they suggest that we can operate at higher frequencies with reduced surface coupling effects using the shorter antennas. They also confirm the beam behavior exhibited in the previous section where the shorter length an-

tennas steered towards lower positions minimizing the surface coupling. In addition, we plotted the average absolute-valued differences in the signal strength at the two antenna depths for the three furthest receivers as a function of frequency for the 3.4 and 2.0 cm antenna lengths (Figure 12). The deviation for the longer antenna appears to increase noticeably (i.e., nominally above 2 dB) above 1900 MHz while that for the 2.0 cm antenna only increases significantly at 2500 MHz.

4. CONCLUSIONS

We have assessed the antenna design to extend the usable operating frequency range of our clinical microwave breast imaging system. The primary difficulties have occurred in the imaging planes closest to the liquid surface where we have observed significant perturbations in the transmitted signals in the homogeneous case (which serves as the calibration data [27]). The planes near the liquid surface correspond to those closest to the chest wall in clinical breast exams which are important because of the high prevalence of cancer in the axilla zone. We have performed several experiments to determine the parameters of the monopole antennas which govern their overall performance. We have been able to alter the beam steering angle and beam width by modifying the antenna length while still maintaining our nominal operating frequency bandwidth.

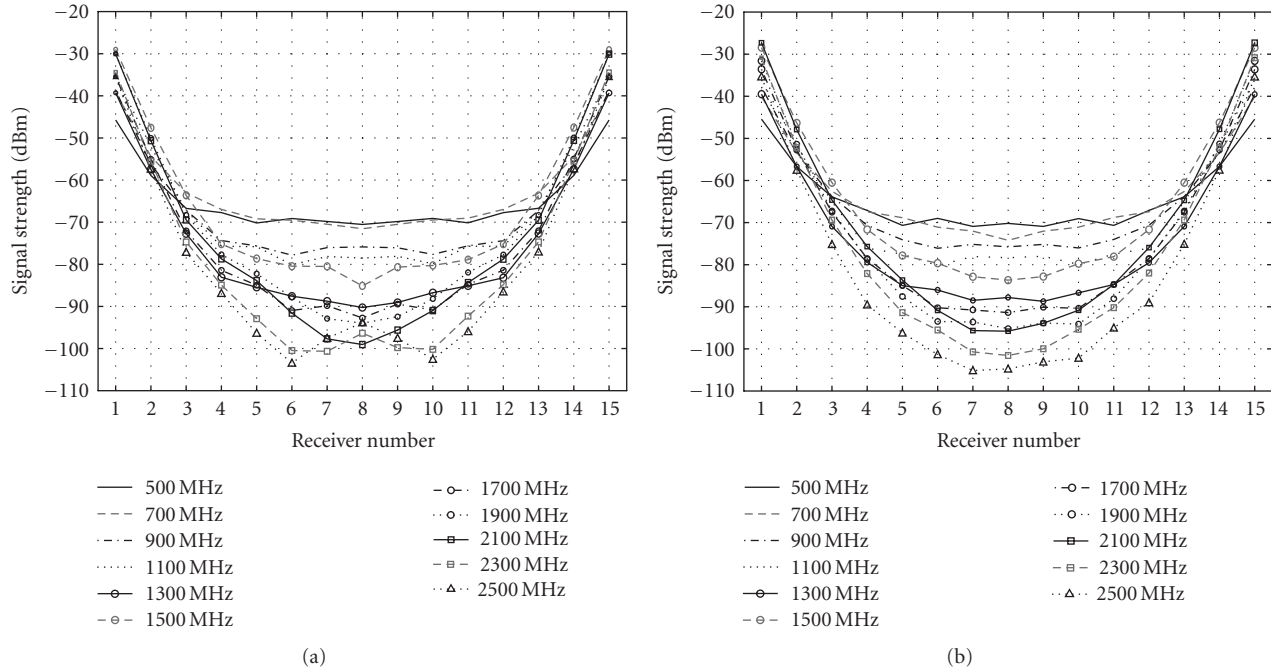


FIGURE 11: Plots of the transmitted signal strength as a function of receiver number over the frequency range of 500–2500 MHz for the 2.0 cm length antennas with their centers submerged (a) 2.0 cm and (b) 6.5 cm below the 90% glycerin coupling liquid surface, respectively.

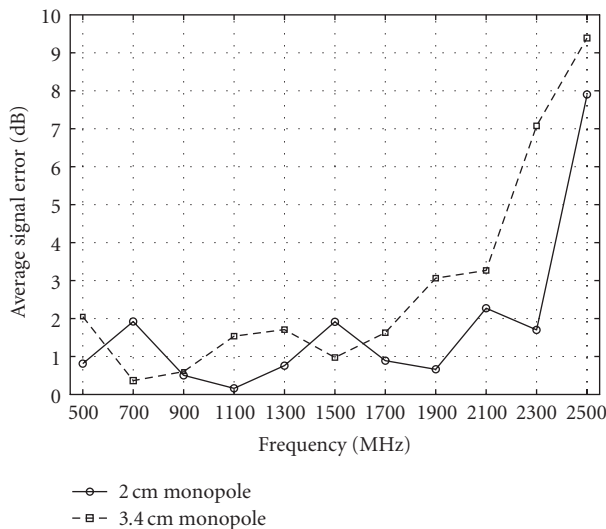


FIGURE 12: Plots of the average differences in signal strengths (utilizing only values for receivers 7, 8, and 9) between the shallow (2.0 cm) and deep (6.5 cm) measurement cases as a function of frequency for the 3.4 and 2.0 cm antenna lengths in the 90% glycerin coupling liquid.

The results comparing the transmission plots for the longer and shorter antennas clearly show that the shorter antennas can operate at higher frequencies for a given imaging plane close to the liquid surface. These improvements were achieved with minimal reduction in overall signal strength (less than 3 dB difference at the higher frequencies).

ACKNOWLEDGMENT

This work was supported by NIH/NCI Grant no. PO1-CA80139.

REFERENCES

- [1] S. S. Chaudhary, R. K. Mishra, A. Swarup, and J. M. Thomas, "Dielectric properties of normal and malignant human breast tissues at radiowave and microwave frequencies," *Indian Journal of Biochemistry and Biophysics*, vol. 21, no. 1, pp. 76–79, 1984.
- [2] W. T. Joines, Y. Zhang, C. Li, and R. L. Jirtle, "The measured electrical properties of normal and malignant human tissues from 50 to 900 MHz," *Medical Physics*, vol. 21, no. 4, pp. 547–550, 1994.
- [3] A. J. Surowiec, S. S. Stuchly, J. R. Barr, and A. Swarup, "Dielectric properties of breast carcinoma and the surrounding tissues," *IEEE Transactions on Biomedical Engineering*, vol. 35, no. 4, pp. 257–263, 1988.
- [4] J. E. Joy, E. E. Penhoet, and D. B. Petitti, *Saving Women's Lives: Strategies for Improving Breast Cancer Detection and Diagnosis*, The National Academy Press, Washington, DC, USA, 2005.
- [5] P. C. Myers, A. H. Barrett, and N. L. Sadowsky, "Microwave thermography of normal and cancerous breast tissue," *Annals of the New York Academy of Sciences*, vol. 335, pp. 443–455, 1980.
- [6] Y. Leroy, A. Mamouni, J. C. Van de Velde, B. Bocquet, and B. Dujardin, "Microwave radiometry for non-invasive thermometry," *Automedica*, vol. 8, pp. 181–202, 1987.
- [7] K. L. Carr, P. Cevalco, P. Dunlea, and J. Shaeffer, "Radiometric sensing: an adjuvant to mammography to determine

- breast biopsy,” in *Proceedings of IEEE MTT-S International Microwave Symposium Digest*, vol. 2, pp. 929–932, Boston, Mass, USA, June 2000.
- [8] S. K. Davis, H. Tandradinata, S. C. Hagness, and B. D. Van Veen, “Ultrawideband microwave breast cancer detection: a detection-theoretic approach using the generalized likelihood ratio test,” *IEEE Transactions on Biomedical Engineering*, vol. 52, no. 7, pp. 1237–1250, 2005.
- [9] S. Caorsi, A. Massa, and M. Pastorino, “A computational technique based on a real-coded genetic algorithm for microwave imaging purposes,” *IEEE Transactions on Geoscience and Remote Sensing*, vol. 38, no. 4, pp. 1697–1708, 2000.
- [10] E. C. Fear and M. A. Stuchly, “Microwave detection of breast cancer,” *IEEE Transactions on Microwave Theory and Techniques*, vol. 48, no. 11, pp. 1854–1863, 2000.
- [11] R. Benjamin, I. J. Craddock, G. S. Hilton, et al., “Microwave detection of buried mines using non-contact, synthetic near-field focusing,” *IEEE Proceedings: Radar, Sonar and Navigation*, vol. 148, no. 4, pp. 233–240, 2001.
- [12] S. P. Poplack, T. D. Tosteson, W. A. Wells, et al., “Electromagnetic breast imaging: results of a pilot study in women with abnormal mammograms,” *Radiology*, vol. 243, no. 2, pp. 350–359, 2007.
- [13] P. M. Meaney, M. W. Fanning, T. Raynolds, et al., “Initial clinical experience with microwave breast imaging in women with normal mammography,” *Academic Radiology*, vol. 14, no. 2, pp. 207–218, 2007.
- [14] A. E. Souvorov, A. E. Bulyshev, S. Y. Semenov, R. H. Svenson, and G. P. Tatsis, “Two-dimensional computer analysis of a microwave flat antenna array for breast cancer tomography,” *IEEE Transactions on Microwave Theory and Techniques*, vol. 48, no. 8, pp. 1413–1415, 2000.
- [15] H. Jiang, C. Li, D. Pearlstone, and L. L. Fajardo, “Ultrasound-guided microwave imaging of breast cancer: tissue phantom and pilot clinical experiments,” *Medical Physics*, vol. 32, no. 8, pp. 2528–2535, 2005.
- [16] A. Massa, D. Franceschini, G. Franceschini, M. Pastorino, M. Raffetto, and M. Donelli, “Parallel GA-based approach for microwave imaging applications,” *IEEE Transactions on Antennas and Propagation*, vol. 53, no. 10, pp. 3118–3127, 2005.
- [17] S. Liewei, L. W. Nolte, Q. Z. Zhong, and Q. H. Liu, “Performance analysis for Bayesian microwave imaging in decision aided breast tumor diagnosis,” in *Proceedings of IEEE International Symposium on Biomedical Imaging (ISBI '02)*, pp. 1039–1042, Washington, DC, USA, July 2002.
- [18] S. C. Hagness, A. Taflove, and J. E. Bridges, “Two-dimensional FDTD analysis of a pulsed microwave confocal system for breast cancer detection: fixed-focus and antenna-array sensors,” *IEEE Transactions on Biomedical Engineering*, vol. 45, no. 12, pp. 1470–1479, 1998.
- [19] X. Yun, E. C. Fear, and R. H. Johnston, “Compact antenna for radar-based breast cancer detection,” *IEEE Transactions on Antennas and Propagation*, vol. 53, no. 8, pp. 2374–2380, 2005.
- [20] R. G. Martin, C. M. de Jong van Coevorden, M. F. Pantoja, S. G. Garcia, and A. R. Bretones, “Ultra-broadband antenna design and characterization,” in *Proceedings of the 2nd International Conference on Electromagnetic Near-Field Characterization & Imaging (ICONIC '05)*, pp. 41–46, Barcelona, Spain, June 2005.
- [21] A. Karlsson, “Physical limitations of antennas in a lossy medium,” *IEEE Transactions on Antennas and Propagation*, vol. 52, no. 8, pp. 2027–2033, 2004.
- [22] P. Kosmas and C. M. Rappaport, “FDTD-based time reversal for microwave breast cancer detection-localization in three dimensions,” *IEEE Transactions on Microwave Theory and Techniques*, vol. 54, no. 4, pp. 1921–1927, 2006.
- [23] T. Takenaka, H. Zhou, and T. Tanaka, “Inverse scattering for a three-dimensional object in the time domain,” *Journal of the Optical Society of America A*, vol. 20, no. 10, pp. 1867–1874, 2003.
- [24] A. Abubakar, P. M. van den Berg, and J. J. Mallorqui, “Imaging of biomedical data using a multiplicative regularized contrast source inversion method,” *IEEE Transactions on Microwave Theory and Techniques*, vol. 50, no. 7, pp. 1761–1771, 2002.
- [25] A. Fhager, P. Hashemzadeh, and M. Persson, “Reconstruction quality and spectral content of an electromagnetic time-domain inversion algorithm,” *IEEE Transactions on Biomedical Engineering*, vol. 53, no. 8, pp. 1594–1604, 2006.
- [26] S. Y. Semenov, A. E. Bulyshev, A. Abubakar, et al., “Microwave-tomographic imaging of the high dielectric-contrast objects using different image-reconstruction approaches,” *IEEE Transactions on Microwave Theory and Techniques*, vol. 53, no. 7, pp. 2284–2294, 2005.
- [27] D. Li, P. M. Meaney, T. Raynolds, S. A. Pendergrass, M. W. Fanning, and K. D. Paulsen, “Parallel-detection microwave spectroscopy system for breast imaging,” *Review of Scientific Instruments*, vol. 75, no. 7, pp. 2305–2313, 2004.
- [28] R. M. Sega, “Infrared detection of microwave induced surface currents on flat plates,” Final Technical Report Air Force Academy, 1982.
- [29] C. A. Balanis, *Antenna Theory Analysis and Design*, John Wiley & Sons, New York, NY, USA, 2nd edition, 1997.
- [30] B. Drozd and W. T. Joines, “Comparison of coaxial dipole antennas for applications in the near-field and far-field regions,” *Microwave Journal*, vol. 47, no. 5, pp. 160–176, 2004.
- [31] S. P. Poplack, K. D. Paulsen, A. Hartov, et al., “Electromagnetic breast imaging: average tissue property values in women with negative clinical findings,” *Radiology*, vol. 231, no. 2, pp. 571–580, 2004.
- [32] H. Q. Woodard and D. R. White, “The composition of body tissues,” *British Journal of Radiology*, vol. 59, no. 708, pp. 1209–1218, 1986.
- [33] K. R. Foster and J. L. Schepps, “Dielectric properties of tumor and normal tissues at radio through microwave frequencies,” *Journal of Microwave Power*, vol. 16, no. 2, pp. 107–119, 1981.
- [34] B. Brooksby, S. Srinivasan, B. W. Pogue, et al., “Quantifying adipose and fibroglandular breast tissue properties using MRI-guided NIR tomography,” in *Optical Tomography and Spectroscopy of Tissue VI*, vol. 5693 of *Proceedings of SPIE*, pp. 255–264, San Jose, Calif, USA, January 2005.
- [35] D. B. Kopans, *Breast Imaging*, Lippincott Williams & Wilkins, Philadelphia, Pa, USA, 2nd edition, 1997.
- [36] P. M. Meaney, T. Raynolds, L. Potwin, and K. D. Paulsen, “3-point support mechanical steering system for high intensity focused ultrasound,” *Physics in Medicine and Biology*, vol. 52, no. 11, pp. 3045–3056, 2007.
- [37] R. E. Collin, *Foundations for Microwave Engineering*, McGraw-Hill, New York, NY, USA, 1966.
- [38] A. Taflove and S. C. Hagness, *Computational Electrodynamics: The Finite-Difference Time-Domain Method*, Atech House, Norwood, Mass, USA, 2nd edition, 2000.
- [39] J.-P. Berenger, “A perfectly matched layer for the absorption of electromagnetic waves,” *Journal of Computational Physics*, vol. 114, no. 2, pp. 185–200, 1994.

Research Article

Directive Antenna for Ultrawideband Medical Imaging Systems

Amin M. Abbosh

School of Information Technology and Electrical Engineering, The University of Queensland, St. Lucia, Qld 4072, Australia

Correspondence should be addressed to Amin M. Abbosh, abbosh@itee.uq.edu.au

Received 19 July 2007; Revised 10 October 2007; Accepted 22 January 2008

Recommended by Elise Fear

A compact and directive ultrawideband antenna is presented in this paper. The antenna is in the form of an antipodal tapered slot with resistive layers to improve its directivity and to reduce its backward radiation. The antenna operates over the frequency band from 3.1 GHz to more than 10.6 GHz. It features a directive radiation with a peak gain which is between 4 dBi and 11 dBi in the specified band. The time domain performance of the antenna shows negligible distortion. This makes it suitable for the imaging systems which require a very short pulse for transmission/reception. The effect of the multilayer human body on the performance of the antenna is also studied. The breast model is used for this purpose. It is shown that the antenna has more than 90% fidelity factor when it works in free space, whereas the fidelity factor decreases as the signal propagates inside the human body. However, even inside the human body, the fidelity factor is still larger than 70% revealing the possibility of using the proposed antenna in biomedical imaging systems.

Copyright © 2008 Amin M. Abbosh. This is an open access article distributed under the Creative Commons Attribution License, which permits unrestricted use, distribution, and reproduction in any medium, provided the original work is properly cited.

1. INTRODUCTION

Ultrawideband (UWB) (3.1–10.6 GHz) microwave imaging is a promising method for biomedical applications such as cancer detection because of their good penetration and resolution characteristics. The underlying principle of UWB cancer detection is a significant contrast in dielectric properties, which is estimated to be greater than 2 : 1 between normal and cancerous tissue. UWB imaging systems have shown encouraging results in the detection of tumors for early breast-cancer detection [1].

In the UWB imaging systems, a very narrow pulse is transmitted from a UWB antenna to penetrate the body. As the pulse propagates through the various tissues, reflections and scattering occur at the interfaces. A particular interest is in the scattered signal from a small size-tissue representing a tumor. The reflected and scattered signals can be received using an UWB antenna, or array of antennas, and used to map different layers of the body. For an accurate imaging system with high resolution and dynamic range, the transmitting/receiving UWB antenna should be planar, compact in size, and directive with high-radiation efficiency and distortionless pulse transmission/reception.

The majority of the compact UWB antennas presented in the literature exhibit omnidirectional radiation patterns with relatively low gain and an impulse response with observable distortion [2]. These types of UWB antennas are suitable for the short-range indoor and outdoor communication. However, for radar systems, such as an UWB microwave imaging system for detection of tumor in woman's breast, a moderate gain directional antenna is advantageous. In addition to an UWB impedance bandwidth, as defined by the minimum return loss of the 10 dB, the UWB antenna is required to support a very short pulse transmission with negligible distortion. This is necessary to achieve precision imaging without ghost targets. The unipolar and antipodal Vivaldi antennas presented in the literature [3–5] satisfy the requirements for imaging systems in terms of bandwidth, gain, and impulse response. However, the achieved performance is at the expense of a significant size, which has a length of several wavelengths. Therefore, the challenge is to reduce their physical dimensions such that it can be incorporated in a compact microwave imaging detection system, while maintaining its broadband, high-gain, and distortionless performance.

Several UWB antenna designs with compact size and low distortion have been proposed for the use in the medical

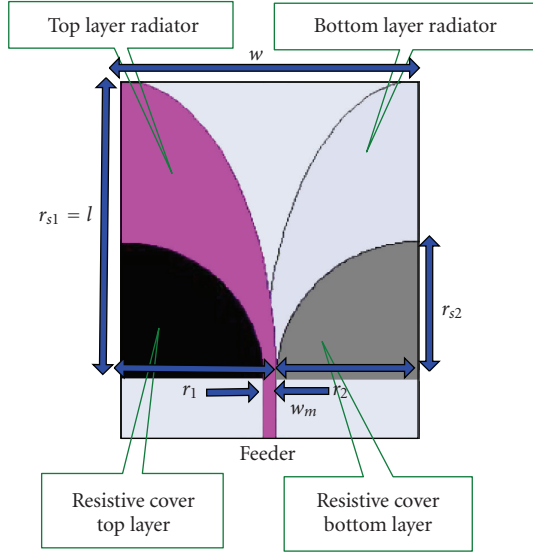


FIGURE 1: Configuration of the proposed antenna.

imaging systems [6–8]. Each has its own merits and drawbacks. Some of the proposed antennas have a nonplanar structure, whereas others have low-gain and/or low-radiation efficiency. The low-radiation efficiency is a major impairment that limits the dynamic range of the imaging system, whose major objective is to detect a weak backscatter from a tumor.

In the presented work, a compact (5 cm × 5 cm) elliptical tapered slot UWB antenna is described. A clear design guideline is given in order to show how to calculate values of the different design parameters of the antenna. Resistive layers were incorporated with the radiating elements of the antenna to improve its directivity and reduce any backward radiation which may affect the accuracy of the imaging system. The measured and simulated results of the proposed antenna show an ultrawideband behavior with a moderate gain and distortionless pulse transmission/reception.

2. DESIGN

The antenna presented in this paper is to be used in a microwave imaging for breast-cancer detection. The imaging system includes a circular array of the proposed ultrawideband antenna. In this system, one of the antennas is used to transmit a microwave signal while the rest of the antennas in the array receive the scattered signal. The measured data is collected and then the measurement procedure is repeated with the second transmitting the signal while the remaining are used for receiving the scattered signal. This process is repeated until all antennas in the array perform the transmitting role. The antenna array can be moved up and down automatically via a computer-controlled high-precision linear actuator. This facilitates the collection of multiple planar data for 3D object imaging.

The proposed ultrawideband antenna for inclusions in the UWB microwave imaging system is shown in Figure 1. It resembles an antipodal tapered slot antenna fed by a parallel strip line.

The radiating element is in the form of an antipodal planar tapered slot with an elliptical curvature. Rogers RO4003 with 3.38 dielectric constant and 0.508 mm thickness was used as a substrate. A resistive layer of $50 \Omega/\square$ was sprayed at the designated areas at the lower end of the radiating structure in the top and bottom layers to improve the front-to-back ratio, and thus the detection capabilities of the UWB imaging system.

The design objective is to obtain a directive antenna with a compact size, while maintaining the bandwidth requirement of 3.1 to 10.6 GHz. The following design procedure is proposed and utilized in developing the proposed antipodal antenna.

Step 1. Given the lowest frequency of operation (f_l), thickness of the substrate (h) and its dielectric constant (ϵ_r), the width (w) and length (l) of the antenna structure, excluding the feeder, can be calculated using the following equation [9]:

$$w = l = \frac{c}{f_l} \sqrt{\frac{2}{\epsilon_r + 1}}, \quad (1)$$

where c is the speed of light in free space.

It is worthwhile to mention that (1) indicates that the antenna's length and width is chosen to be equal to the effective wavelength calculated at the lowest frequency of operation.

Step 2. The radiating structure of the antenna is formed from the intersection of quarters of two ellipses. The major radii (r_1 and r_2) and the secondary radii (r_{s1} and r_{s2}) of the two ellipses are chosen according to the following equation:

$$\begin{aligned} r_1 &= \frac{w}{2} + \frac{w_m}{2}, \\ r_2 &= \frac{w}{2} - \frac{w_m}{2}, \\ r_{s1} &= l, \\ r_{s2} &= 0.5r_2. \end{aligned} \quad (2)$$

According to (2), dimensions of the radiating element are chosen such that the far-end distance between the top and bottom radiators is equal to the effective wavelength at the lowest frequency of operation. Length of each of the radiators at the left and the right end of the antenna's structure shown in Figure 1 is equal to half of the effective wavelength calculated at the lowest frequency of operation.

Step 3. The width of the microstrip transmission feeder (w_m) to give the characteristic impedance, Z_0 equal to 50Ω , can be calculated using the following equations [10]:

$$w_m = \frac{120\pi}{\sqrt{\epsilon_r}} \frac{h}{Z_0}. \quad (3)$$

Step 4. A metallization layer, with a $50 \Omega/\square$ surface resistivity, is added to the top and bottom radiating parts. Shape of the resistive layers is chosen to be a quarter of an ellipse with major and secondary diameters equal to r_2 and r_{s2} , respectively.

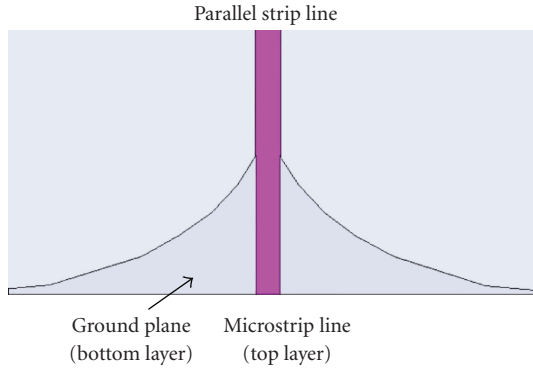


FIGURE 2: Configuration of the parallel strip line to microstrip transition.

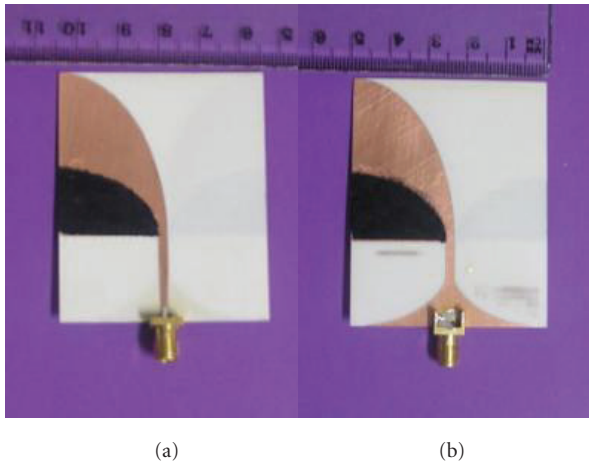


FIGURE 3: Photo of the developed antenna: (a) top view, and (b) bottom view.

Step 5. A transition is added to the structure of the antenna. This is required because the antenna's radiating element shown in Figure 1 is connected to a parallel strip line, which is a balanced transmission line, whereas the antenna is to be connected to the other devices of the imaging system using a suitable coaxial cable, which is an unbalanced transmission line. The transition from the parallel strip line to the microstrip line is shown in Figure 2, which is adopted from the transitions presented in [11]. The strip line, which is located at the top layer, is connected using a tapered transmission line to the microstrip line, while width of the strip line at the bottom layer is gradually increased to form the ground plane required for the microstrip feeder.

3. RESULTS

The ultrawideband antenna designed according to the above mentioned procedure was manufactured using Rogers RO4003C ($\epsilon_r = 3.38$, $h = 0.506$ mm) as a substrate. Values of the design parameters w , l , r_1 , r_2 , r_{s1} , r_{s2} , and w_m (shown in Figure 1) are 50 mm, 50 mm, 26 mm, 24 mm, 50 mm, 12 mm, and 2 mm, respectively. A photo for the developed antenna is shown in Figure 3.

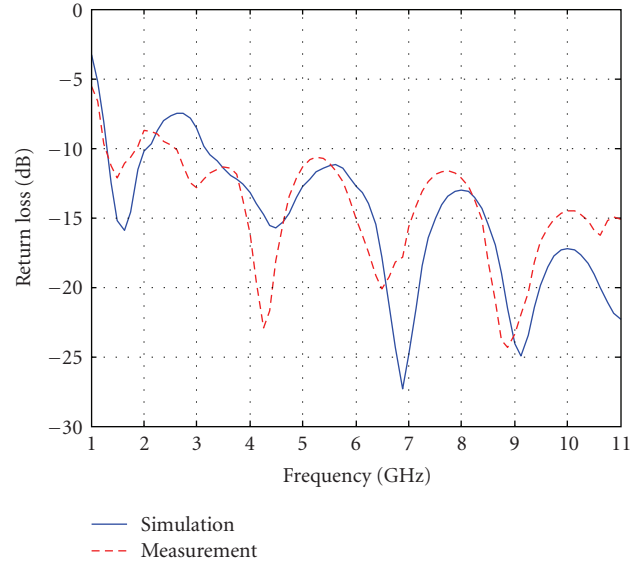


FIGURE 4: The measured and simulated return loss.

Concerning the resistive layers, a parametric analysis using the software Ansoft HFSSv10 indicated that the best performance concerning the bandwidth and the front-to-back ratio can be achieved when the resistivity of the added resistive layer is in the range from $50 \text{ } \Omega/\square$ to $100 \text{ } \Omega/\square$. The lower value was used because of the availability of the $50 \text{ } \Omega/\square$ chemical mixture to the author.

The validity of the proposed design methodology is verified using the commercial software package, Ansoft HFSSv10, and experimental tests by using a vector network analyzer.

Figure 4 shows the simulated and measured return loss of the manufactured antenna. As can be seen from Figure 3, the 10 dB return loss bandwidth extends from 3.1 GHz to more than 11 GHz covering the required UWB band of 3.1 GHz–10.6 GHz. The simulated result closely resembles the measured result validating the design procedure of the antenna.

The far-field radiation patterns of the antenna were calculated using the software HFSS. They are shown in Figure 5 for the frequencies 4 GHz, 6 GHz, 9 GHz, and 11 GHz. The antenna shows directive properties with an average front-to-back ratio which is greater than 13 dB across the whole band, making it a good candidate for microwave imaging applications. It is worthwhile to mention that without the use of the resistive layers, the front-to-back ratio is around 10 dB.

The measured gain of the antenna is shown in Figure 6, which reveals a moderate gain antenna. The gain is equal to 4.3 dBi at 3 GHz and it increases with frequency till it becomes 10.8 dBi at 10.6 GHz. It is to be noted that the gain measurements were done in comparison with a reference-gain antenna which is the corrugated horn antenna in this case.

As the use of the resistive layer can be responsible for the reduction in the radiation efficiency, suitable calculations with the help of the software HFSS were performed with respect to this parameter. From Figure 6, it is apparent that despite the use of the resistive layers to minimize the backward

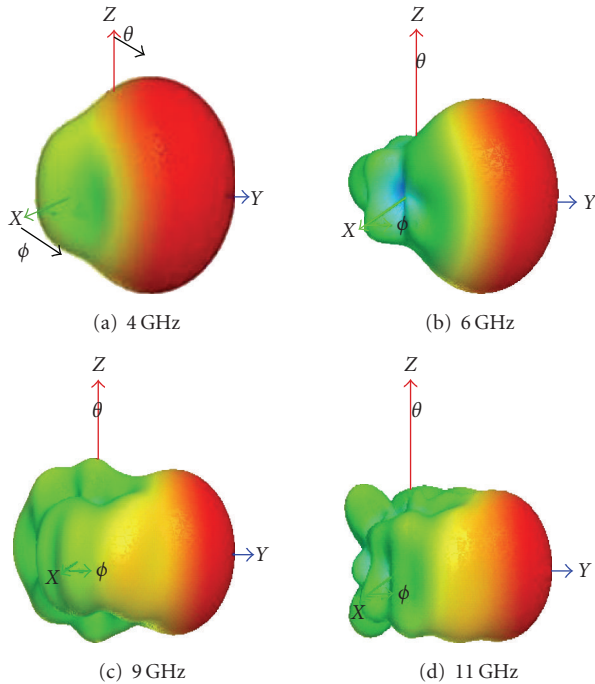


FIGURE 5: The simulated three-dimensional radiation pattern.

radiation (and hence enhance the front-to-back ratio), the proposed antenna has a good efficiency, which is more than 80% across the whole band. This performance is superior in comparison with the antennas reported for use in a microwave imaging system, where 47% efficiency was noted [8].

The time-domain performance of the proposed antenna was also measured. A narrow pulse was synthesized in the network analyzer using the discrete Fourier transform module of the device. The pulse was synthesized after assuming that its frequency spectrum is a rectangular function that extends from 3.1 to 10.6 GHz. Shape of the resulted synthesized pulse is shown in Figure 7. Two copolarized antennas were separated by a distance of 50 cm and the results of the measurement are shown in Figure 7. Note that the excited pulse and the received pulse are normalized with respect to their peak values. The figure reveals that the pulse duration of the antenna is 0.6 nanoseconds. The pulse distortion occurs at the 0.15 level with respect to the peak level of 1, and thus it is almost negligible. The observed results indicate that the developed antenna supports distortionless narrow pulse which makes it an excellent radiator for the purpose of a microwave imaging with high resolution.

As the antenna is to be put on or near the human body, specifically the breast for the case of breast-cancer detection, a study of the effect of the distance from the skin to the antenna on its return loss is investigated. The electromagnetic model used to simulate the breast contains two layers: the first layer is the skin layer with thickness = 2 mm, dielectric constant = 36, and conductivity = 4 S/m. The second layer is the breast tissue, which extends to a width of 10 cm, with a dielectric constant = 9 and conductivity = 0.4 S/m [12]. Results of simulation using the software HFSS are shown in Figure 8 for two different distances between the antenna and

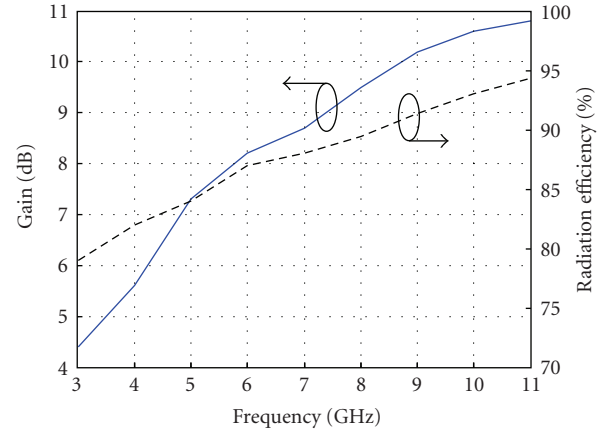


FIGURE 6: The measured gain and calculated radiation efficiency of the antenna.

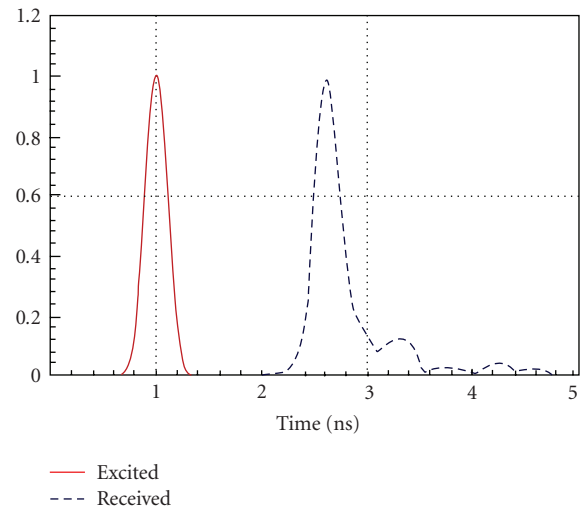


FIGURE 7: The measured impulse response of the antenna.

the human body. Figure 8 indicates clearly that the antenna maintains its ultrawideband performance in spite of being very close to the human body.

The imaging system in which the antenna is to be used contains an array of antennas. Hence, it is important to investigate the value of the mutual coupling between these antennas. The mutual coupling between two identical antennas at different frequencies was calculated using the software HFSS. In the calculations, two antennas were assumed to be parallel to each other and the distance between them was changed. The mutual coupling was calculated at each distance and the results are shown in Figure 9. These results show that the coupling decreases as the distance between the two antennas increases. For a certain distance between the two antennas, the mutual coupling is less for a higher frequency. This is because increasing the frequency means a lower wavelength. Therefore, the distance between the coupled antennas relative to the wavelength is larger. The results depicted in Figure 9 reveal that the mutual coupling between the neighboring antennas at any frequency within the ultrawideband range is less than -20 dB when the distance between the antennas is more than half a wavelength.

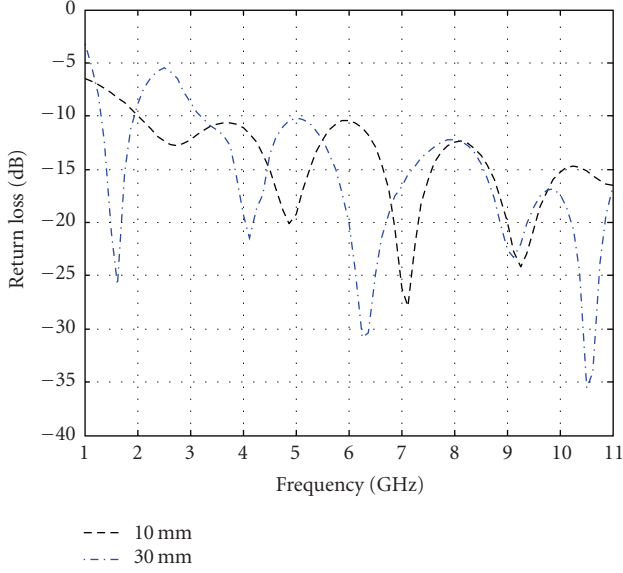


FIGURE 8: The simulated return loss of the antenna for different distances from the human body.

It is also important to study the distortion when the radiated pulse propagates through the human body, that is, the skin and the breast tissue in the case of the breast-cancer-detection system. The antenna fidelity is used as an indication of that distortion. The fidelity factor is the maximum magnitude of the cross correlation between the observed pulse at a certain distance and the excitation pulse [13]. The finite difference time-domain method was used for this purpose [14]. In order to reduce the computation domain, Berenger’s perfectly matched layer (PML) is applied as an absorbing boundary condition [15]. To include the frequency dependence of the dielectric constant ϵ_i and the conductivity σ_i of the breast tissue over the UWB, the first-order Debye dispersion model was applied [12]:

$$\epsilon_i - \frac{j\sigma_i}{2\pi f\epsilon_o} = \epsilon_\infty + \frac{\epsilon_\Delta - \epsilon_\infty}{1 + j2\pi f\tau} - \frac{j\sigma_\Delta}{2\pi f\epsilon_o}, \quad (4)$$

where τ is the relaxation time, and ϵ_Δ , ϵ_∞ , and σ_Δ are the Debye model parameters which were selected according to the published data for the breast tissues [12]: normal tissue: $\epsilon_\Delta = 10$, $\epsilon_\infty = 7$, $\tau = 7$ ps, $\sigma_\Delta = 0.15$ S/m, tumor: $\epsilon_\Delta = 54$, $\epsilon_\infty = 4$, $\tau = 7$ ps, $\sigma_\Delta = 0.4$ S/m. For the skin: $\epsilon = 36$, and $\sigma = 4$ S/m.

The result is shown in Figure 10 where the effect of all the scattered/reflected signals is included. It indicates that as the signal propagates through the human body, the fidelity factor decreases. This indicates an increasing pulse distortion inside the human body. For the antenna presented in this paper, the fidelity factor is within reasonable values (more than 70%) even inside the human body.

4. CONCLUSION

The design of a directive ultrawideband antenna for use in a microwave imaging system has been presented. To mini-

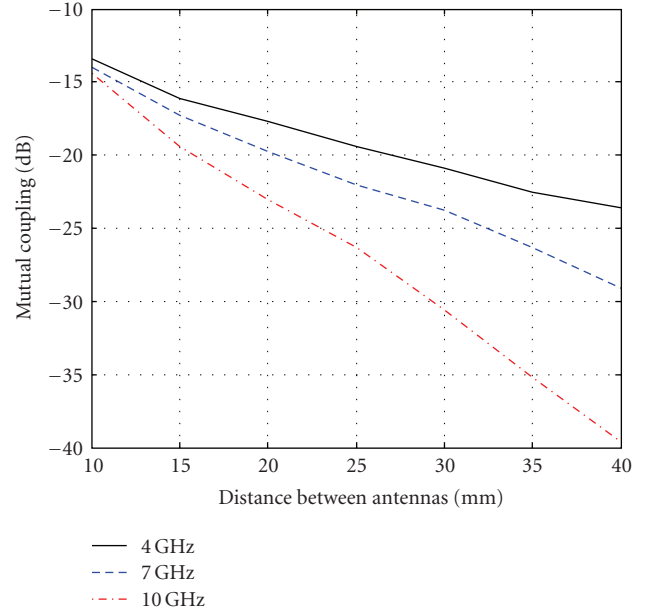


FIGURE 9: Variation of the simulated mutual coupling with the distance between the antennas at different frequencies.

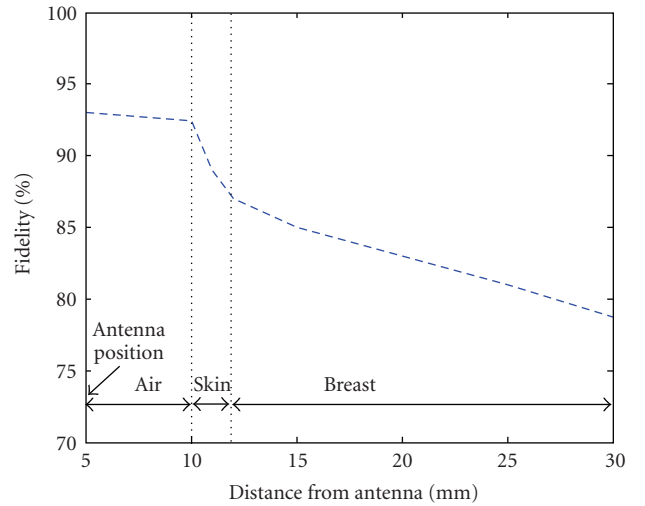


FIGURE 10: The simulated fidelity factor with the distance from the antenna in the presence of a human body.

mize the backward radiation, the antenna uses resistive layers behind its conductive radiation layers. The simulated and measured characteristics of the antenna have shown that it covers the band from 3.1 GHz to more than 11 GHz. It has a radiation efficiency of more than 80%, which is higher than the recently reported other UWB planar antennas employing resistive layers for microwave imaging applications. The characteristics of the antenna when operating near a human body have been investigated. The simulated results have shown that the antenna maintains its ultrawideband performance concerning the return loss even with the presence of the human body in proximity with the antenna.

The time-domain performance of the antenna has also been studied. It has been shown that the proposed antenna

has the ability to send and receive very short pulses in a distortionless manner. It has been shown that although the fidelity factor decreases as the signal propagates through the human body, the value of that factor is still within acceptable limits.

The mutual coupling between two identical antennas has been simulated as the antenna elements are used within an array in the microwave imaging systems. It has been shown that the mutual coupling is less than -20 dB when the distance between the neighboring antennas is more than half a wavelength.

REFERENCES

- [1] E. C. Fear, P. M. Meaney, and M. A. Stuchly, "Microwaves for breast cancer detection?" *IEEE Potentials*, vol. 22, no. 1, pp. 12–18, 2003.
- [2] J. Liang, C. C. Chiau, X. Chen, and C. G. Parini, "Printed circular disc monopole antenna for ultra-wideband applications," *Electronics Letters*, vol. 40, no. 20, pp. 1246–1247, 2004.
- [3] J. D. S. Langley, P. S. Hall, and P. Newham, "Balanced antipodal Vivaldi antenna for wide bandwidth phased arrays," *IEE Proceedings: Microwaves, Antennas and Propagation*, vol. 143, no. 2, pp. 97–102, 1996.
- [4] E. Guillaumont, J. Y. Dauvignac, Ch. Pichot, and J. Cashman, "A new design tapered slot antenna for ultra-wideband applications," *Microwave and Optical Technology Letters*, vol. 19, no. 4, pp. 286–289, 1998.
- [5] M. Chiappe and G. L. Gagnani, "Vivaldi antennas for microwave imaging: theoretical analysis and design considerations," *IEEE Transactions on Instrumentation and Measurement*, vol. 55, no. 6, pp. 1885–1891, 2006.
- [6] X. Yun, E. C. Fear, and R. Johnston, "Broadband cross-polarized bowtie antenna for breast cancer detection," in *Proceedings of IEEE Antennas and Propagation Society International Symposium*, vol. 3, pp. 1091–1094, Columbus, Ohio, USA, June 2003.
- [7] C. J. Shannon, E. C. Fear, and M. Okoniewski, "Dielectric-filled slotline bowtie antenna for breast cancer detection," *Electronics Letters*, vol. 41, no. 7, pp. 388–390, 2005.
- [8] H. Kanj and M. Popovic, "Miniaturized microstrip-fed "Dark Eyes" antenna for near-field microwave sensing," *IEEE Antennas and Wireless Propagation Letters*, vol. 4, pp. 397–401, 2005.
- [9] A. M. Abbosh, H. K. Kan, and M. E. Bialkowski, "Compact ultra-wideband planar tapered slot antenna for use in a microwave imaging system," *Microwave and Optical Technology Letters*, vol. 48, no. 11, pp. 2212–2216, 2006.
- [10] D. M. Pozar, *Microwave Engineering*, John Wiley & Sons, New York, NY, USA, 3rd edition, 2005.
- [11] S.-G. Kim and K. Chang, "Ultrawide-band transitions and new microwave components using double-sided parallel-strip lines," *IEEE Transactions on Microwave Theory and Techniques*, vol. 52, no. 9, part 1, pp. 2148–2152, 2004.
- [12] S. K. Davis, H. Tandradinata, S. C. Hagness, and B. D. Van Veen, "Ultrawideband microwave breast cancer detection: a detection-theoretic approach using the generalized likelihood ratio test," *IEEE Transactions on Biomedical Engineering*, vol. 52, no. 7, pp. 1237–1250, 2005.
- [13] D. Lamensdorf and L. Susman, "Baseband-pulse-antenna techniques," *IEEE Antennas and Propagation Magazine*, vol. 36, no. 1, pp. 20–30, 1994.
- [14] D. M. Sullivan, *Electromagnetic Simulation Using the FDTD Method*, John Wiley & Sons, New York, NY, USA, 2000.
- [15] J.-P. Berenger, "A perfectly matched layer for the absorption of electromagnetic waves," *Journal of Computational Physics*, vol. 114, no. 2, pp. 185–200, 1994.

Application Article

A 31.5 GHz Patch Antenna Design for Medical Implants

Yasir Ahmed,^{1,2} Yang Hao,¹ and Clive Parini¹

¹Antennas and Electromagnetics Group, Electrical Engineering Department, Queen Mary, University of London, London E14AH, UK

²Electrical Engineering Department, COMSATS Institute of Information Technology, Plot 30, Sector H8-1, Islamabad, Pakistan

Correspondence should be addressed to Yasir Ahmed, yasirahmed@comsats.edu.pk

Received 7 November 2007; Revised 29 March 2008; Accepted 17 July 2008

Recommended by Tamer Ibrahim

We have proposed a 31.5 GHz patch antenna for medical implants. The design is based on the transmission line model and is simulated in CST. The patch antenna performs reasonably well in terms of return loss and radiation efficiency. However, the most attractive feature of this design is its form factor. Typical antennas designed for the microwave range are quite large in size, which makes them unsuitable for implants. The proposed design is much smaller in size but still retains the essential characteristics for reliable communication.

Copyright © 2008 Yasir Ahmed et al. This is an open access article distributed under the Creative Commons Attribution License, which permits unrestricted use, distribution, and reproduction in any medium, provided the original work is properly cited.

1. INTRODUCTION

The design of antennas for communication with implants inside the human body has received considerable attention from the research community. The design of these antennas is quite challenging, as there is a limit on the amount of power that can be transmitted and also on the size of these devices. The limitation on the transmit power is due to the amount of battery power available as well as due to concerns about the exposure of the human body to electromagnetic radiation. Typically these devices are allowed to have a peak transmit power of 25 uW (−16 dBm), which is quite insufficient at higher frequencies especially when embedded deep into the tissue. Today these implants are being used to monitor as well as facilitate the working of various human organs, for example, as cardiac pacemakers.

2. SURVEY OF ANTENNAS FOR IMPLANTS

A number of different antenna designs have been considered for medical implants. In [1], spiral and serpentine antenna designs have been considered and the authors have simulated the performance of these antennas using a single block of muscle and a realistic human shoulder. The results are also verified experimentally using a tissue simulant material composed of TX-151, sugar, salt, and water. The effect of shape and size of the dielectric as well as the location of the feed point on the performance of the antenna is

studied. A similar analysis is performed in [2] for spiral and planar inverted-F (PIFA) antenna. However, the authors have primarily focused on the human brain using a six-layer model (brain, CSF, Dura, bone, fat, and skin). The results are again verified using a human tissue-simulating liquid made from deionized water, sugar, salt, and cellulose. In both these papers, the authors have considered a frequency of 402–405 MHz that has been recommended by the European Radiocommunications Committee (ERC) for ultra-low-power, active, medical implants. The simulations have been performed using finite difference time domain (FDTD) method. In addition, an analytic method using spherical dyadic Green's function (DGF) has also been considered [2].

In [3], the problem of antenna detuning and signal loss is studied for a subminiature loop antenna designed for the 900 MHz ISM and 402 MHz MICS radio bands. It is observed that with proper encapsulation of areas of high electric field strength antenna detuning can be considerably reduced. This is in contrast to a monopole that experiences considerable detuning (as high as 13%) and signal loss at the same frequencies.

The results of an actual implant operating in the 403 MHz MICS band are presented in [4]. The implant was placed inside a Perspex body (30 cm diameter cylinder), and the signal strength was measured as a function of the distance. The error rate of the link was also evaluated. It was observed that the communication link with the external device was maintained up to a distance of 3 m when the

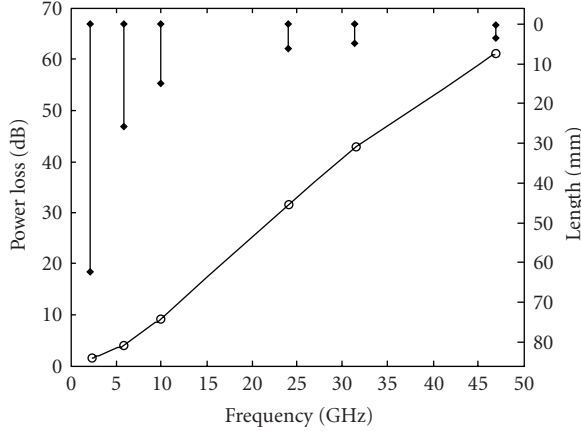


FIGURE 1: Power loss within 4 mm of skin. The corresponding half wavelengths are also shown.

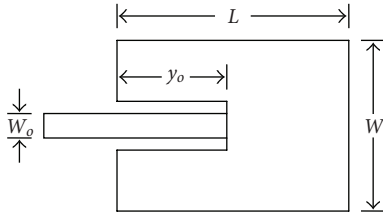


FIGURE 2: Patch antenna with a line feed.

TABLE 1: Dielectric properties of human tissues at 31.5 GHz.

Tissue	Permittivity	Conductivity (S/m)
Skin	14.7980	27.9710
Fat	3.5970	1.8636
Muscle	22.2700	36.8130

implant was placed at a depth of 10 cm. The implant used a sleep and wakeup sequence (2.4 GHz, 20 dBm wakeup signal) to prolong battery life.

3. LIMITATIONS IN THE DESIGN PROCESS

Microstrip antenna design is a fairly mature field, and several designs have been proposed over the years [5–7]. As with any other antenna design, the size of the microstrip is directly proportional to the wavelength at the operating frequency. At 402 MHz, the wavelength of an electromagnetic wave is approximately 0.75 m. It is obvious that any antenna with dimensions comparable to this wavelength cannot be used for an implant. The technique usually used to overcome this problem is to design a conducting surface that is spiraled along the surface of the substrate. The resonant frequency of the microstrip is then proportional to the total length of the spiral and not to the length of any individual element.

Although this results in a size reduction, it is still not quite suitable for an implant (see Table 2). We have investigated the idea of using a rectangular patch antenna designed to operate at the millimeter wave frequencies. It is well known that at these frequencies the electromagnetic wave experiences very high attenuation, however, the implant does not need to be placed deep into the tissue and with proper transmit receive combination it is still possible to maintain reliable communication. The penetration depth of a medium is defined as

$$\delta = \frac{1}{\alpha}, \quad (1)$$

where α is the attenuation constant. It is the distance at which the amplitude of an electromagnetic wave is reduced to $e^{-1} = 0.3679$ of its original value.

It has been observed that at millimeter wave most of the loss occurs within the first layer, that is, skin. There is a relatively less loss within fat and at the dielectric boundaries. Figure 1 shows the power loss within the layer of skin as a function of frequency. Also shown are corresponding half wavelengths which should serve as a guideline to the antenna size. The actual antenna size would also be dependant on the substrate material; however, any size reduction would be proportionate across the frequency range.

4. DESIGN PROCEDURE

A microstrip antenna can be designed using either the transmission line model or the cavity model (more complex models also exist that suit a particular design). We have used the transmission line model since it is fairly simple to implement and results in antenna designs with reasonably good performance in terms of return loss and efficiency. It is also quite well suited to the rectangular designs that we have considered (other popular designs include circular, elliptical, and disc like). The design starts with selecting the operating frequency f_r , selecting a substrate with the required permittivity ϵ_r , and defining the width of the substrate h (Figure 2). Thick substrates with low permittivity result in antenna designs with high efficiency and large bandwidths. Thin substrates with high permittivity lead to a smaller antenna size but with a lower bandwidth and a high-radiation loss [5]. The tradeoffs between substrate thickness and permittivity and antenna bandwidth and efficiency have been discussed in [8–10]. We have used Rogers RT6002 in our design with a permittivity of 2.94 and a loss tangent of 0.0012.

According to the transmission line model, the length L and width W of the patch are calculated as

$$W = \frac{v_0}{2f_r} \sqrt{\frac{2}{\epsilon_r + 1}}, \quad (2)$$

$$L = \frac{v_0}{2f_r \sqrt{\epsilon_{\text{reff}}}} - 2\Delta L,$$

TABLE 2: Comparison of five different antennas designed for medical implants. The size of our antenna is governed by the dimensions of the ground plane.

Antenna type	True antenna size	Characteristics
Spiral [1] 402 MHz	 26.6 mm × 16.8 mm	Return loss >25 dB Frequency detuning ~15% -21 dBW at 1 m (7 mm deep in 2/3 muscle, 1.6 W/kg)
Serpentine [1] 475 MHz	 26.6 mm × 16.8 mm	Return loss >10 dB Frequency detuning ~20% -25 dBW at 1 m (7 mm deep in 2/3 muscle, 1.6 W/kg) Higher resonant frequency than a spiral with the same physical length
Spiral [2] 402 MHz	 40 mm × 32 mm	Return loss >18 dB Return loss >5 dB (measurement) Frequency detuning ~5% (measurement) Front to back ratio ~5 dB Radiation efficiency ~0.16%
PIFA [2] 402 MHz	 32 mm × 24 mm	Return loss >16 dB Return loss >6 dB (measurement) Frequency detuning ~10% (measurement) Front to back ratio ~5 dB Radiation efficiency ~0.25% Higher efficiency than the spiral
New design 31.5 GHz	 5.68 mm × 6 mm W = 3.39 mm L = 2.66 mm h = 0.254	Return loss >30 dB Frequency detuning ~1% -57.49 dBW/m ² at 1 m (8 mm deep in skin and fat) Front to back ratio ~15 dB

where v_o is the speed of light in free space, ϵ_{reff} is the effective permittivity, and $2\Delta L$ is the extension in length due to fringing effects:

$$\epsilon_{\text{reff}} = \frac{\epsilon_r + 1}{2} + \frac{\epsilon_r - 1}{2} \left[1 + 12 \frac{h}{W} \right]^{-1/2}, \quad (3)$$

$$\Delta L = 0.412h \frac{(\epsilon_{\text{reff}} + 0.3)(W/h + 0.264)}{(\epsilon_{\text{reff}} - 0.258)(W/h + 0.8)}.$$

Although the design of the patch is quite simple, the design of the feeding mechanism is not that straightforward. There

are four possible methods that can be used:

- (1) microstrip-line feed;
- (2) probe feed;
- (3) aperture-coupled feed;
- (4) Proximity-coupled feed.

We have used a microstrip line feed since it is relatively easy to model, match, and fabricate. It results in low- antenna bandwidths (2–5%); however, this should be sufficient for our application. The calculation of the feed point is based on the principle that maximum power transfer would occur when the impedance of the line is matched to the patch. At the resonant frequency, the impedance of the patch is zero

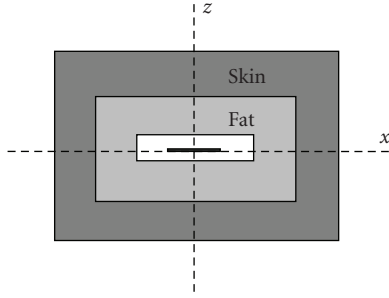


FIGURE 3: Patch implanted inside the model (4 mm Skin, 4 mm Fat, 1 mm cavity).

at the half point along its length. Therefore, the feed point is usually a little offset from the centre. We first calculate G_1 and G_{12} the self and mutual conductance of the patch terminals (also termed as the radiating slots), respectively:

$$G_1 = \int_0^\pi \left[\frac{\sin((k_o W/2) \cos \theta)}{\sqrt{120\pi \cos \theta}} \right]^2 \sin^3 \theta d\theta,$$

$$G_{12} = \int_0^\pi \left[\frac{\sin((k_o W/2) \cos \theta)}{\sqrt{120\pi \cos \theta}} \right]^2 J_0(k_o L \sin \theta) \sin^3 \theta d\theta,$$
(4)

where

$$k_o = \frac{2\pi\sqrt{\epsilon_{\text{reff}}}}{\lambda},$$
(5)

and J_0 is the modified Bessel function of the first kind and order zero. The length of the inset y_o can then be calculated based upon the following relationship:

$$R_{\text{in}}(y = y_o) = \frac{1}{2(G_1 \pm G_{12})} \cos\left(\frac{\pi y_o}{L}\right).$$
(6)

Here, R_{in} is the impedance value required for perfect matching. Since the inset creates a physical notch in the patch, it also changes its resonant frequency (due to junction capacitance); however, this shift is usually a small percentage of the actual frequency and can be ignored. Alternatively, the length or width of the patch would have to be modified, and the feed location would have to be recalculated. The width of the inset is somewhat arbitrary.

5. SIMULATION RESULTS

The designed patch antenna is then simulated in CST at a frequency of 31.5 GHz. The antenna is placed within a three-layer body consisting of skin, fat, and air (Figure 3) and energized by a waveguide port with a normalized power of 1 W^Φ (Φ denotes the 10 gm tissue that we have used. The transmit power should be less than 16 mW ($1.6 \text{ W/kg} \times 0.010 \text{ kg}$). This would reduce our link budget by approximately 18 dB). We used air as the cavity around the antenna; however, in practice, some other low permittivity medium might be used to provide a match between the antenna and the body. The dielectric data used in the simulation is given in Table 1.

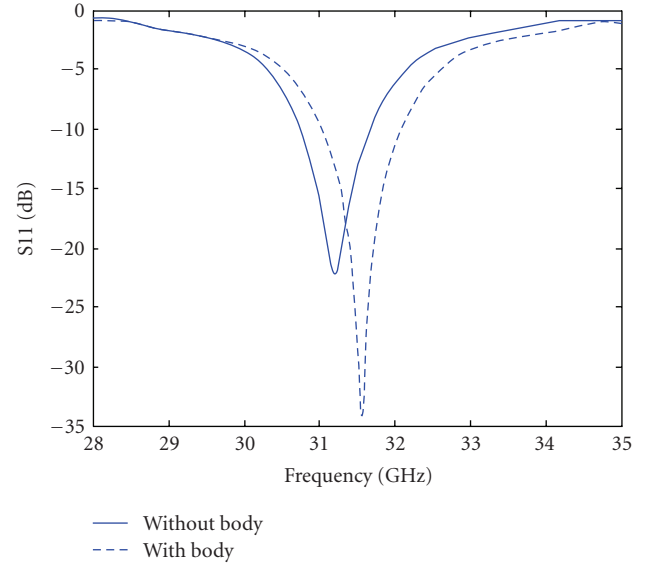


FIGURE 4: Return loss of the antenna with and without the body.

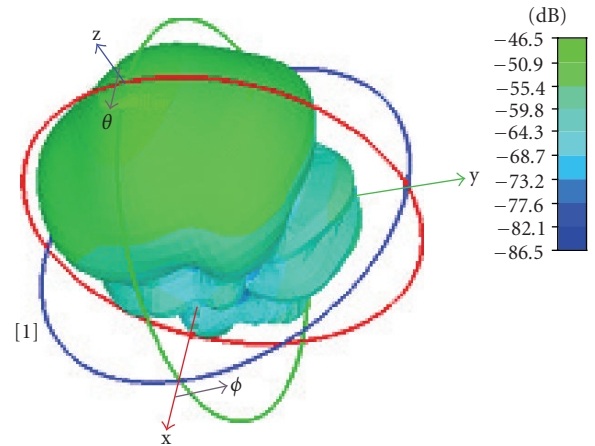


FIGURE 5: Gain of the antenna placed inside the cavity.

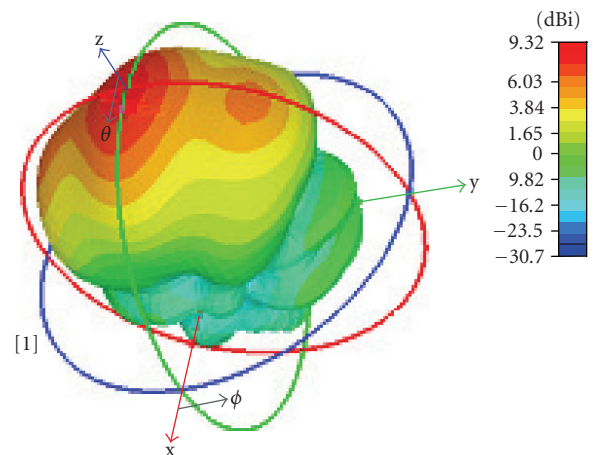
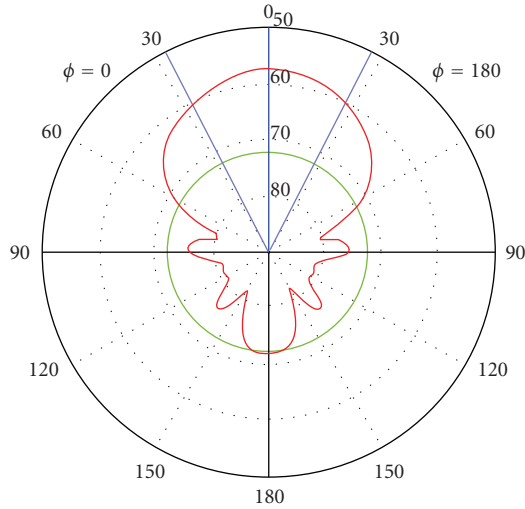
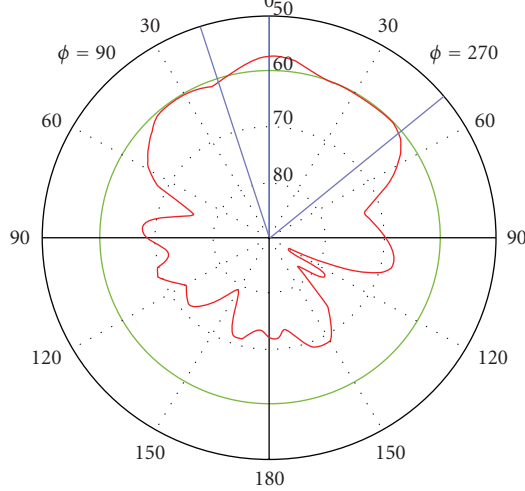


FIGURE 6: Directivity of the antenna placed inside the cavity.



Angular width (3 dB) = 54.8 deg
Side lobe level = -14.4 dB

(a)



Angular width (3 dB) = 68.2 deg
Side lobe level = -2.4 dB

(b)

FIGURE 7: P-field along (a) H-plane (b) E-plane.

The resulting S-parameters and 3D radiation patterns are shown below (Figures 4–6). The antenna has a return loss of more than 30 dB and max broadside directivity of 9.32 dBi. The antenna exhibits some detuning within the body which is removed by adjusting its dimensions. The P-field patterns in the E-plane and H-plane are shown in Figure 7. It is observed that the antenna has a very low efficiency due to the high loss within the body; however, it has a good front to back ratio. The embedded antenna has a peak broadside power density of -57.5 dBW/m^2 at a distance of 1 m.

For an isotropic radiator with a transmit power of 1 W, the power density at a distance of 1 m is

$$S = P_t/4\pi d^2 = 1/4\pi = -10.99 \text{ dBW/m}^2, \quad (7)$$

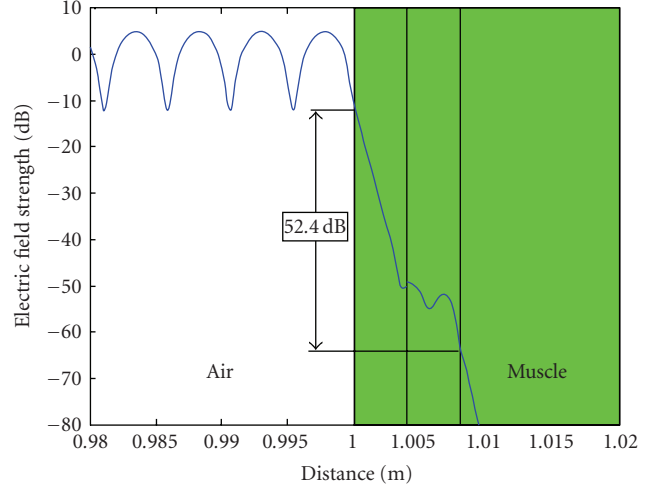


FIGURE 8: Relative electric field strength $20 \log_{10}(|E_t|/|E_o|)$. External device to implant communication.

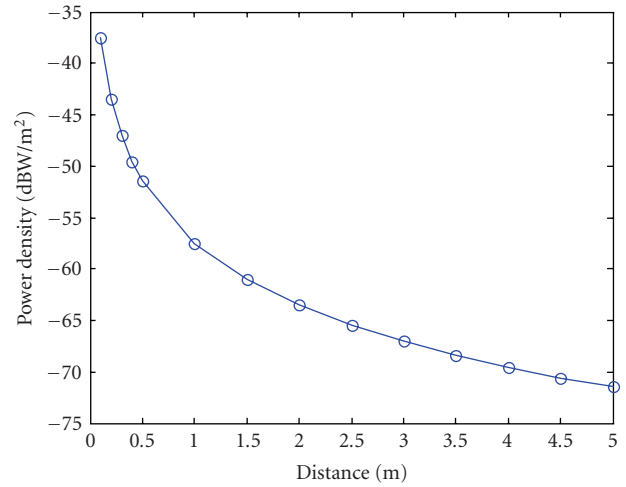


FIGURE 9: P-field from an implant as a function of distance.

and for the embedded patch with a gain of -46.5 dB^\dagger the power density would be

$$S = -10.99 - 46.50 = -57.49 \text{ dBW/m}^2, \quad (8)$$

which is equal to the result obtained through p-field simulation (\dagger denotes the computer simulation technology (CST) that considers the antenna and the body as the radiator. Therefore, the gain is the gain of the complete structure and not just the designed antenna).

Now, if the effective area A_e of the antenna is known then the received power P_r at a particular distance can be easily calculated. The effective area [11] of a half wave dipole is given as

$$A_e = \frac{G_r \lambda^2}{4\pi} = \frac{\lambda^2}{8} = -49.46 \text{ dBs}, \quad (9)$$

where G_r^Y is the receive antenna gain. This gives a received power of -106.95 dBW or -76.95 dBm (Y denotes the

formula given in the text that uses directivity instead of gain; however, this is only valid if there is no loss in radiation).

In the absence of the body, the antenna has a power density of -3.63 dBW/m² at a distance of 1 m. Therefore, there is a power loss of 53.87 dB within the body. Similar results are obtained for the reverse link using ray-tracing where a 52.40 dB loss is observed within the layers of skin and fat (Figure 8). It must be noted that the wireless communication channel between an implant and an external device is not symmetric and the link budget in one direction might be quite different from that in the other direction.

Finally, we have shown the p-field behaviour outside the body as a function of the distance (Figure 9). As expected, in the absence of any external body, the P-field follows the $1/d^2$ rule.

6. CONCLUSION

Although a signal level -76.95 dBm might be sufficient in theory, it would not be adequate in a realistic scenario where the signal would experience multipath fading and interference from other wireless equipment. However, it must be noted that we have considered a simple dipole antenna at the receiver with a nominal directional gain. Since there is no limitation on the size of the external equipment, we can make use of a large antenna with a very high gain along the direction of transmission. In some scenarios, it might also be possible to place the antenna close to the body (closer than 1 m) further improving the quality of the received signal.

Finally, it must be noted that the return loss of the antenna increases inside the body (+11.81 dB) and there is also some frequency detuning (1.14%). Higher return loss is a desirable characteristic but frequency detuning is not and can be removed by adjusting the dimensions of the antenna such that the null occurs at the desired frequency.

REFERENCES

- [1] P. Soontornpipit, C. M. Furse, and Y. C. Chung, "Design of implantable microstrip antenna for communication with medical implants," *IEEE Transactions on Microwave Theory and Techniques*, vol. 52, no. 8, part 2, pp. 1944–1951, 2004.
- [2] J. Kim and Y. Rahmat-Samii, "Implanted antennas inside a human body: simulations, designs, and characterizations," *IEEE Transactions on Microwave Theory and Techniques*, vol. 52, no. 8, part 2, pp. 1934–1943, 2004.
- [3] M. Norris and J.-D. Richard, "Sub-miniature antenna design for wireless implants," in *Proceedings of the IET Seminar on Antennas and Propagation for Body-Centric Wireless Communications*, pp. 57–62, London, UK, April 2007.
- [4] H. Higgins, "Body implant communications—is it a reality?" in *Proceedings of the IET Seminar on Antennas and Propagation for Body-Centric Wireless Communications*, pp. 33–36, London, UK, April 2007.
- [5] C. A. Balanis, *Antenna Theory: Analysis and Design*, John Wiley & Sons, New York, NY, USA, 2nd edition, 1997.
- [6] D. M. Pozar, "Microstrip antennas," *Proceedings of the IEEE*, vol. 80, no. 1, pp. 79–91, 1992.
- [7] K. Carver and J. Mink, "Microstrip antenna technology," *IEEE Transactions on Antennas and Propagation*, vol. 29, no. 1, pp. 2–24, 1981.
- [8] B. Pan, Y.-K. Yoon, G. E. Ponchak, M. G. Allen, J. Papapolymerou, and M. M. Tentzeris, "Analysis and characterization of a high-performance Ka-band surface micromachined elevated patch antenna," *IEEE Antennas and Wireless Propagation Letters*, vol. 5, no. 1, pp. 511–514, 2006.
- [9] A. Derneryd, "A theoretical investigation of the rectangular microstrip antenna element," *IEEE Transactions on Antennas and Propagation*, vol. 26, no. 4, pp. 532–535, 1978.
- [10] D. H. Schaubert, D. M. Pozar, and A. Adrian, "Effect of microstrip antenna substrate thickness and permittivity: comparison of theories with experiment," *IEEE Transactions on Antennas and Propagation*, vol. 37, no. 6, pp. 677–682, 1989.
- [11] J. D. Kraus, *Electromagnetics*, McGraw-Hill, New York, NY, USA, 3rd edition, 1984.

Research Article

An Antenna-Theory Method for Modeling High-Frequency RF Coils: A Segmented Birdcage Example

Xin Chen,¹ Victor Taracila,² Timothy Eagan,³ Hiroyuki Fujita,^{1,4,5} Xingxian Shou,¹ Tanvir Baig,⁶ and Robert Brown¹

¹Department of Physics, Case Western Reserve University, 10900 Euclid Avenue, Cleveland, OH 44106, USA

²GE Healthcare, Aurora, OH 44202, USA

³Philips Medical Systems, Highland Heights, OH 44143, USA

⁴Department of Radiology, University Hospitals of Cleveland, Cleveland, OH 44106, USA

⁵Quality Electrodynamics LLC, Mayfield Village, OH 44143-2336, USA

⁶Department of Physics, University of Dhaka, Dhaka 1000, Bangladesh

Correspondence should be addressed to Robert Brown, rwb@case.edu

Received 2 August 2007; Revised 4 December 2007; Accepted 12 February 2008

Recommended by Stuart Crozier

We suggest that center-fed dipole antenna analytics can be employed in the optimized design of high-frequency MRI RF coil applications. The method is illustrated in the design of a single-segmented birdcage model and a short multisegmented birdcage model. As a byproduct, it is shown that for a long single-segmented birdcage model, the RF field within it is essentially a TEM mode and has excellent planar uniformity. For a short shielded multisegmented birdcage model, the RF field is optimized with a target-field approach with an average SAR functional. The planar homogeneity of the optimized RF field is significantly improved compared with that of a single-segmented birdcage model with the same geometry. The accuracy of the antenna formulae is also verified with numerical simulations performed via commercial software. The model discussed herein provides evidence for the effectiveness of antenna methods in future RF coil analysis.

Copyright © 2008 Xin Chen et al. This is an open access article distributed under the Creative Commons Attribution License, which permits unrestricted use, distribution, and reproduction in any medium, provided the original work is properly cited.

1. INTRODUCTION

Radiofrequency (RF) field inhomogeneity has been a major challenge in today's high-field magnetic resonance imaging (MRI) mainly due to the shortened RF wavelength in human tissue at higher frequencies. It has been shown [1] that image quality can be significantly affected. Recently, both experimental and theoretical work have been presented to improve the RF field homogeneity, such as the *TEM resonator* [2, 3], closed-form analytical solutions [4–8], and numerical simulations [9–11]. Techniques such as RF shimming [11] and parallel transmission [12] are applied to improve the RF field homogeneity with a focus on the transmit coil array. Although theoretical progress has been made in analyzing the experimental results, and RF field homogeneity can be improved with various techniques, a better understanding of the relationship between the RF current sources and the RF fields is still needed. A modeling control of the source-field relationship can be used to optimize the RF

performance, much as has been done, for instance, in [13], for lower frequencies. Moreover, the specific absorption rate (SAR) is an important RF safety concern as more RF energy tends to be deposited into human tissue in high-field MRI experiments [14]. Although detailed numerical simulations have been presented to analyze the SAR distribution in the human head within volume and surface coils [15, 16], there is an absence of RF coil models that incorporate both RF field and SAR calculation and optimization. In this paper, we show that analytic formulae found in antenna theory can be applied with success in the optimized design of RF coils. It is well known that a static surface current distribution which is sinusoidal in the azimuthal direction on a surface of a cylinder produces a homogeneous static magnetic field everywhere in the cylinder [17]. We find that in a high frequency case, such sinusoidal current distribution can produce magnetic field which is uniform in transverse planes and oscillates in the direction perpendicular to the transverse plane; thus transverse electromagnetic (TEM) mode can be

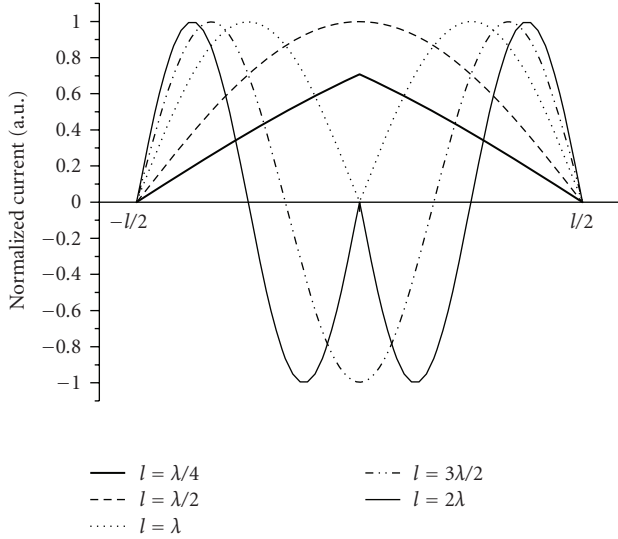


FIGURE 1: Current distribution on a center-fed dipole antenna for different antenna's lengths. λ is the wavelength of the oscillating current source.

supported. With our model we show that by restricting the oscillation of the field required by Maxwell equations to the longitudinal direction, homogeneity in transverse planes can be significantly improved, as demonstrated in [5].

2. METHODS

A good approximation of the oscillating current on a center-fed dipole antenna is a sinusoidal standing wave current with nodes at both ends [18] (Figure 1):

$$\mathbf{I}(x' = 0, y' = 0, z') = \begin{cases} \mathbf{e}_z I_0 \sin \left[k \left(\frac{l}{2} - z' \right) \right], & 0 \leq z' \leq \frac{l}{2}, \\ \mathbf{e}_z I_0 \sin \left[k \left(\frac{l}{2} + z' \right) \right], & -\frac{l}{2} \leq z' \leq 0. \end{cases} \quad (1)$$

Here I_0 is the current amplitude, k is the wave number (i.e., $2\pi/\text{wavelength}$), and l is the length of the antenna. It is assumed that the antenna has negligible cross section and is aligned along the z direction with its center at the origin, as shown in Figure 2. The vector potential and the magnetic field produced by this center-fed dipole antenna are therefore determined [18]:

$$\mathbf{A}(\rho, z) = \frac{\mu_0}{4\pi} \int_{-l/2}^{l/2} \mathbf{I}(z') \frac{e^{-ik\sqrt{\rho^2 + (z-z')^2}}}{\sqrt{\rho^2 + (z-z')^2}} dz', \quad (2)$$

$$\begin{aligned} \mathbf{B}(\rho, z) &= \nabla \times \mathbf{A}(\rho, z) \\ &= -\frac{\mu_0 I_0}{4\pi i} \frac{1}{\rho} \left[e^{-ik\sqrt{\rho^2 + (z-l/2)^2}} + e^{-ik\sqrt{\rho^2 + (z+l/2)^2}} \right. \\ &\quad \left. - 2 \cos \left(\frac{kl}{2} \right) e^{-ik\sqrt{\rho^2 + z^2}} \right] \mathbf{e}_\varphi. \end{aligned} \quad (3)$$

In (2) and (3), the current distribution is given in (1), (ρ, z) represents the cylindrical coordinates of the

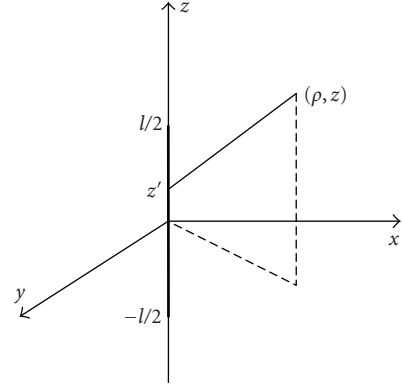


FIGURE 2: Schematic of an idealized center-fed dipole antenna with length l .

observation point in space, and z' determines the location of the source point on the antenna. Given a sinusoidal standing wave current distribution in (1), the magnetic field produced by this source can be calculated analytically at any point in the space with (3).

To model the shorter wavelength effects over relevant dimensions and the average dielectric properties of human head under an RF frequency of 400 MHz, we assume a conducting dielectric with constant permittivity 49.75 and conductivity 0.59 S/m [19] fills up all of space. Therefore, the wavelength for an RF field with frequency 400 MHz (corresponding to 9.4T main magnetic field in proton MRI) is approximately 10.6 cm. We choose this frequency in our modeling as a representative value of interest in today's very high-field MRI research. With the presence of a conducting dielectric and $e^{i\omega t}$ time dependence, the wave number k of the propagation in the dielectric will be complex and satisfy

$$k^2 = \omega^2 \mu_0 \epsilon \epsilon_0 - i\omega \mu_0 \sigma. \quad (4)$$

Although the magnetic field (3) is derived from a sinusoidal current distribution with a real wave number k , we will still use (3) with all the wave numbers k replaced by the complex value given in (4) as an approximate representation of the RF field in the conducting dielectric. With the presence of the conductivity, Maxwell equation gives

$$\nabla \times \mathbf{B} = \mu_0 \epsilon \epsilon_0 \frac{\partial \mathbf{E}}{\partial t} + \mu_0 \sigma \mathbf{E} = (i\omega \mu_0 \epsilon \epsilon_0 + \mu_0 \sigma) \mathbf{E}. \quad (5)$$

The electric field can then be determined as

$$\mathbf{E} = \frac{1}{i\omega \mu_0 \epsilon \epsilon_0 + \mu_0 \sigma} \nabla \times \mathbf{B}. \quad (6)$$

Once the electric field is known, the local SAR at a spatial point \mathbf{r} can be estimated as

$$\text{SAR}(\mathbf{r}) = \frac{\sigma}{2\rho} |\mathbf{E}(\mathbf{r})|^2, \quad (7)$$

and the average SAR in a region of interest is

$$\overline{\text{SAR}} = \frac{1}{N} \sum_{i=1}^N \text{SAR}(\mathbf{r}_i), \quad (8)$$

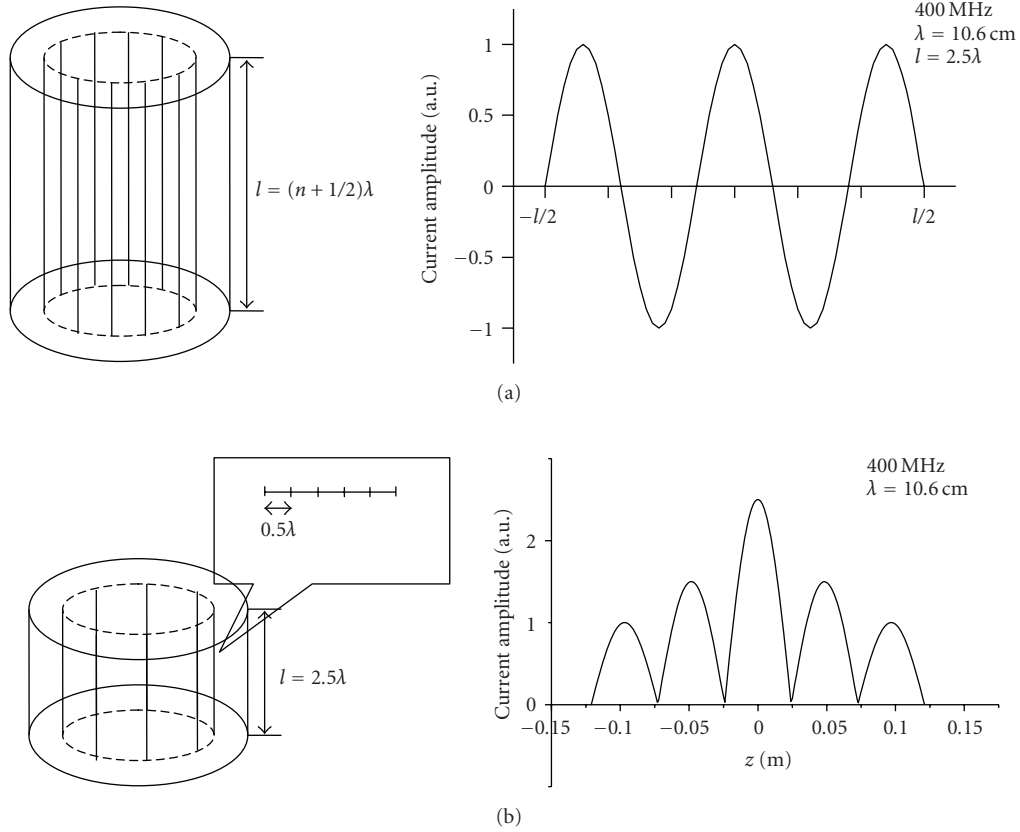


FIGURE 3: (a) Schematics of a shielded single-segmented birdcage model and a representative current distribution on an axial conductor. A model with 10 conductors is shown. The length l satisfies $l = (n + 1/2)\lambda$ where n is an even integer and λ is the wavelength of the source current. A representative current distribution on a 2.5λ -long center-fed dipole antenna is also shown. (b) Schematics of a shielded multisegmented birdcage model and a representative current distribution on an axial conductor consisting with five half-wavelength-long center-fed dipole antennas.

where the density of the dielectric ρ is 1030 kg/m^3 [19] representing an average human head value and \mathbf{r}_i ($i = 1, 2, 3, \dots, N$) are N spatial points specified in a region of interest.

A shielded single-segmented birdcage model and a new shielded multisegmented birdcage model are constructed with center-fed dipole antennas as building blocks respectively. The RF fields produced by the two models are separately calculated and compared, after the multisegmented model is optimized with respect to the axial field uniformity and the average SAR. The shielded single-segmented birdcage model (Figure 3(a)) has 16 evenly spaced axial conductors forming a birdcage structure (a model with 10 legs is shown in the picture for clarity) and a cylindrical shield. The inner diameter is 25 cm and the outer diameter is 29 cm, attempting to model a typical head RF coil. Each axial conductor is constructed as a center-fed dipole antenna and there are no end rings. The azimuthal current distribution among conductors is sinusoidal. Along the longitudinal (z) direction, the current has a simple sinusoidal standing wave z -profile as given in (1). It is noted that when the length of the center-fed dipole antenna satisfies $l = (n + 1/2)\lambda$ (where λ is the wavelength of the oscillating current source and n is any even integer), the current distribution (1) becomes

$\cos(kz)$. Thus, in order to avoid more complicated charge and current distributions, the length of the center-fed dipole antenna is always assumed to be $(n + 1/2)\lambda$ with n an even integer. Also, to focus on the wavelength effect due to the shortened electromagnetic wavelength by itself we neglect, for the moment, the conductivity of the dielectric for all the calculations related to the RF field distribution of the single-segmented birdcage model. The effect of the shield can be simulated with the image method [20], which states that the field produced by the currents induced on a shield is identical to the field produced by the image of the original current with respect to the shield. In the case of a cylindrical shield, the image of the current flowing in the axial conductor is a current flowing with opposite direction and located coaxially at a distance $R_{\text{sh}}(R_{\text{sh}} - R_0)/R_0$ from the shield, where R_{sh} and R_0 are the outer and inner radii of the birdcage model, respectively. The RF fields of the shielded birdcage model are then determined with (3).

For the shielded multisegmented birdcage model (Figure 3(b)), the length is chosen to be 2.5λ (approximately 26.6 cm). The inner and the outer diameters of the model are 25 cm and 29 cm, respectively, the same as the single-segmented birdcage. There are eight axial conductors and no end rings. Each axial conductor consists of five

half-wavelength-long center-fed dipole antennas. Three of them (the middle segment and the two on one side of the middle segment) are independently fed and the other two on the other side have current sources that are fixed by the axial symmetry around the central transverse plane. The image method described above is also applied here to incorporate the effect of the cylindrical shielding. Based on (3) and (6), the magnetic and the electric fields produced by each RF element (the half-wavelength-long center-fed dipole antenna) can be calculated. Therefore, the magnetic and the electric fields of the model are the superposition of the fields produced by all the individual RF elements and are functions of current amplitudes and phases on these elements. In order to obtain a uniform RF field profile with control over average SAR, a functional is constructed as

$$\begin{aligned}
W &= \overline{\text{SAR}} \\
&+ \sum_{j=1}^{N_r} \lambda_j \left[B_{1,x}(I_1, \phi_1, I_2, \phi_2, \dots, I_{N_0}, \phi_{N_0}; \mathbf{r}_j) - B_x^{(\text{target})}(\mathbf{r}_j) \right] \\
&+ \sum_{j=1}^{N_r} \mu_j \left[B_{1,y}(I_1, \phi_1, I_2, \phi_2, \dots, I_{N_0}, \phi_{N_0}; \mathbf{r}_j) - B_y^{(\text{target})}(\mathbf{r}_j) \right] \\
&= \frac{1}{N_{\text{SAR}}} \sum_{i=1}^{N_{\text{SAR}}} \frac{\sigma}{2\rho} |\mathbf{E}(\mathbf{r}_i)|^2 \\
&+ \sum_{j=1}^{N_r} \lambda_j \left[B_{1,x}(I_1, \phi_1, I_2, \phi_2, \dots, I_{N_0}, \phi_{N_0}; \mathbf{r}_j) - B_x^{(\text{target})}(\mathbf{r}_j) \right] \\
&+ \sum_{j=1}^{N_r} \mu_j \left[B_{1,y}(I_1, \phi_1, I_2, \phi_2, \dots, I_{N_0}, \phi_{N_0}; \mathbf{r}_j) - B_y^{(\text{target})}(\mathbf{r}_j) \right].
\end{aligned} \tag{9}$$

Here, I_i and ϕ_i are the unknown current amplitude and phase on the i th half-wavelength-long center-fed dipole antenna, N_0 is the total number of the antennas (which is equal to 40 in the present model), \mathbf{r}_j is the j th of the N_r total constraint points in the central axial plane where we calculate the x and y components of the RF field produced by the model ($B_{1,x}$ and $B_{1,y}$) and impose the desired target field with both uniform amplitude and phase ($B_x^{(\text{target})} = 0$ and $B_y^{(\text{target})} = \text{constant}$), and \mathbf{r}_i is the i th of the N_{SAR} total spatial points in a region of interest (ROI) where we determine the electric field $\mathbf{E}(\mathbf{r}_i)$ and the local SAR. A cylindrical ROI with a diameter of 16 cm and a length of 8 cm coaxially located within the multisegmented birdcage model, with their centers coincide, is selected for an illustrative SAR calculation. λ_j and μ_j are the familiar Lagrange multipliers. The functional W is minimized to obtain a uniform RF field using a functional approach to control SAR. The minimization is achieved by differentiating with respect to I_i , ϕ_i , λ_j , and μ_j , and solving the obtained $2N_0 + 2N_r$ equations to find $2N_0 + 2N_r$ unknowns I_i , ϕ_i , λ_j , and μ_j . Since the SAR term is a quadratic function of unknown current amplitudes and phases, the $2N_0 + 2N_r$ equations are all linear and can be solved with matrix inversion. Optimal current amplitudes and phases are found and can be employed as sources parameters to determine the corresponding RF field and SAR profiles.

3. RESULTS

The single-segmented birdcage model is assumed to be driven by a current that is sinusoidal in the azimuthal direction around any transverse plane

$$I_j = I_0 e^{i(\omega t + \phi_j)}, \tag{10}$$

where I_j and ϕ_j are the current amplitude and phase in the j th axial conductor, and the phase ϕ_j coincides with the azimuthal angle of the axial conductor. The RF fields produced by models with different lengths $l = (n + 1/2)\lambda$ are calculated with the analytical formula (3). It is shown that with fixed diameter, the longer model has increasingly better RF field uniformity. Figure 4 shows maps of the amplitude of the clockwise component of the circularly polarized RF field (the component contributing to the excitation of the nucleus spins) in the central transverse plane for single-segmented birdcage models with lengths (a) 2.5λ (approximately 26.6 cm), (b) 10.5λ (approximately 1.12 m), (c) 20.5λ (approximately 2.18 m), and (d) 100.5λ (approximately 10.7 m). The normalized RF field amplitude across the central transverse plane along the x -axis is also shown (Figure 4(e)). In terms of the maximum percentage deviation from the field at the center, the model with a length of 2.5λ has a nonuniformity of 60%, the one with a length of 10.5λ has a value of 32%, the 20.5λ -long model has a value of 10%, and the 100.5λ -long model only has a nonuniformity of 0.4%. The normalized amplitude of the RF field along the longitudinal direction (z direction) is shown in Figure 5. As the length of the model increases, the oscillation of the field in the z direction approaches the absolute value of $\cos(kz)$, where k is the wave number of propagation in the dielectric. In contrast to a low-frequency birdcage, the length of the coil has to be very long before excellent transverse uniformity is achieved.

The unknown current amplitudes and phases of a multisegmented birdcage model are found through the aforementioned optimization process. Table 1 shows current amplitudes and phases among the eight half-wavelength-long center-fed dipole antennas of three independent-fed sections (i.e., the middle section, the section to the right (left) of the middle section, and the rightmost (leftmost) section) for the B1 field strength $1.16 \mu\text{T}$ at the center of the model. The symmetry of the current amplitudes implies that among the eight antenna segments of any section only four of them are independent. The current phases, nevertheless, do not exhibit any specific symmetries or relations with the azimuthal angles of the RF elements. The RF field optimized for uniformity in the central transverse plane is calculated with the solved currents. Figure 6 shows the map of the amplitude of the clockwise component of the field along the x -axis in the central transverse plane of the optimized multisegmented birdcage model. It can be seen that in the central region, the RF field variation is below 20%, compared with a nearly 60% variation of a single-segmented birdcage model (Figure 4). Figure 7 shows the RF field variation along the longitudinal (z) direction for the optimized multisegmented birdcage. The field pattern

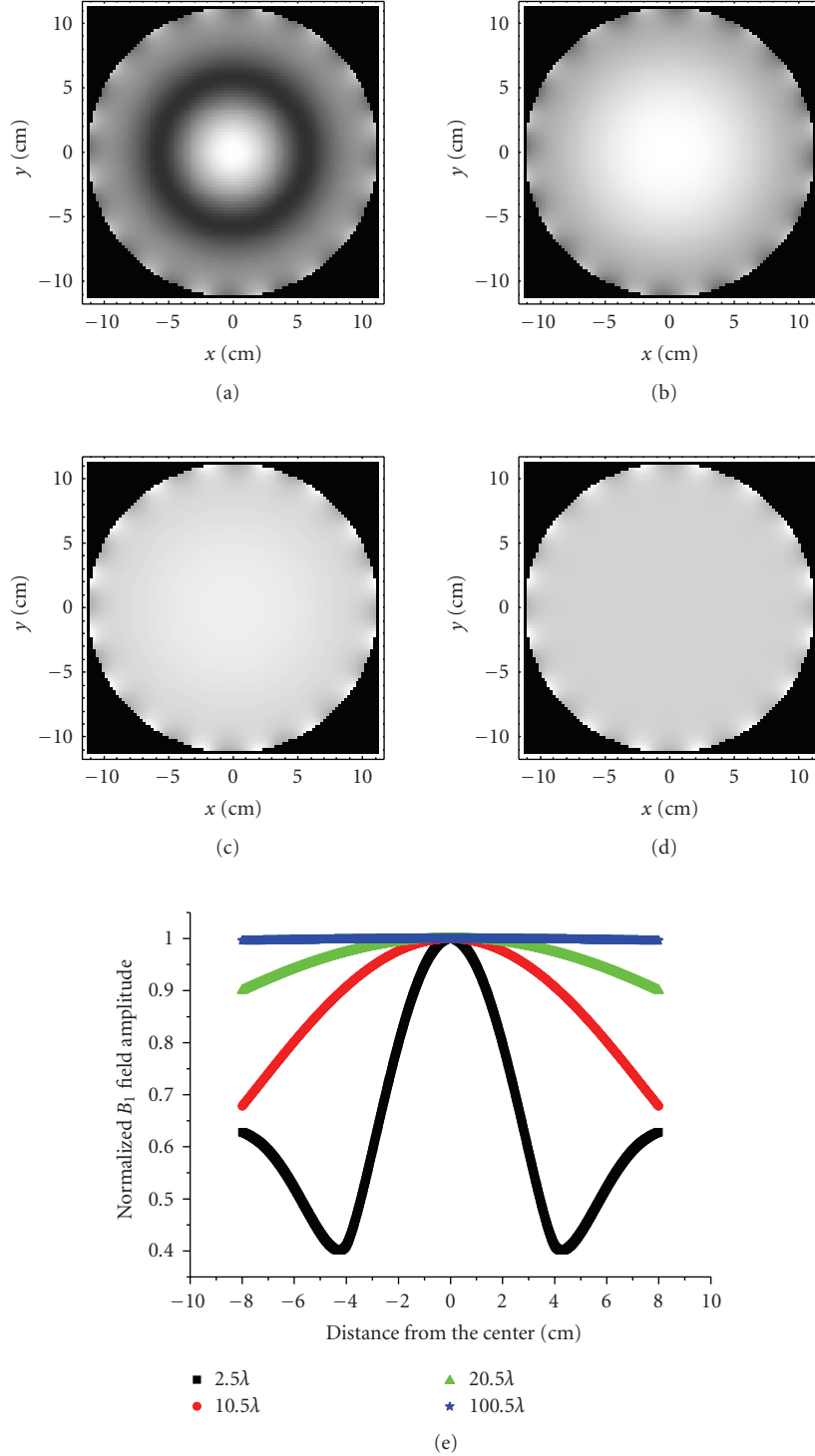


FIGURE 4: Amplitude of the clockwise component of the circularly polarized RF field in the central transverse planes for the single-segmented birdcage models with length (a) 2.5λ , (b) 10.5λ , (c) 20.5λ , and (d) 100.5λ . In (e), the normalized field variation across the central transverse plane along x -axis is shown.

coincides with the absolute value of $\cos(\alpha z)$ in the proximity of $z = 0$, where α is the real part of the complex wave number of the propagation in the dielectric. The average SAR within the aforementioned cylindrical ROI of this optimized model is 3.7 W/kg .

4. DISCUSSION

Due to the shortened RF field wavelength inside human tissue for high-field MRI, it is more difficult to use conventional RF coils to generate uniform RF field over the imaging

TABLE 1: Optimal current (a) amplitudes and (b) phases of the half-wavelength-long center-fed dipole antenna elements in the multi-segmented birdcage model.

(a) Current amplitudes/A								
Azimuthal angle of RF elements/degree	22.5	67.5	112.5	157.5	202.5	247.5	292.5	337.5
The rightmost (leftmost) section	10.95	7.45	3.47	12.38	10.95	7.45	3.47	12.38
The right (left) section	6.35	4.23	2.65	7.43	6.35	4.23	2.65	7.43
The middle section	4.02	2.88	2.26	5.32	4.02	2.88	2.26	5.32
(b) Current phases/degree								
Azimuthal angle of RF elements/degree	22.5	67.5	112.5	157.5	202.5	247.5	292.5	337.5
The rightmost (leftmost) section	158.59	216.59	264.86	317.69	338.59	36.59	84.86	137.69
The right (left) section	283.06	335.27	23.05	90.43	103.06	155.27	203.05	270.43
The middle section	95.49	145.82	196.06	268.50	275.49	325.82	16.06	88.5005

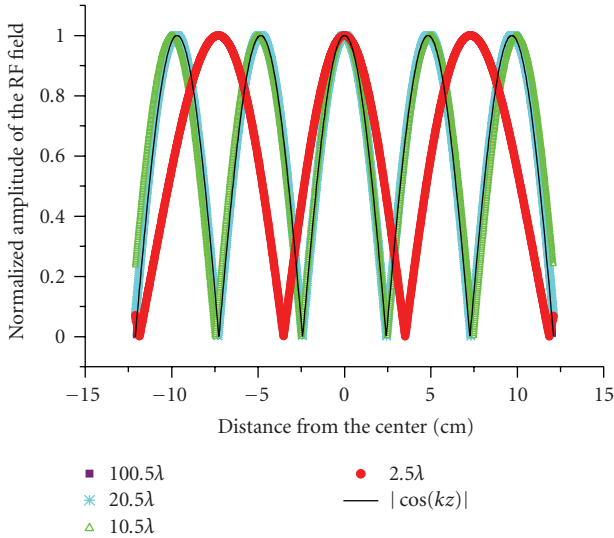


FIGURE 5: RF field variation along the longitudinal (z) direction for single-segmented birdcage models with different lengths. The results are all compared with the absolute value of the cosine function.

region of interest. In terms of theoretical considerations, the Biot-Savart law, which is widely applied to determine the RF field in the low-frequency regime, is unable to give accurate predictions for the RF field of high frequency. For high-field MRI, most of the theoretical calculations and simulations are performed with commercial software and iterative numerical algorithms. Whatever analytical solutions that have been found previously available are mathematically complicated and have rarely been used to simulate modern RF applications, such as RF shimming and parallel transmission. In this paper, we have applied new analytic formulae from antenna theory to calculate the RF fields for a representative class of RF coils, namely, head coils with a birdcage structure. For the single-segmented birdcage model (with single center-fed dipole antennas used for each axial conductor), at high frequency, increasing the length leads to improved central planar uniformity for the RF field.

In fact, if the length of the model is much larger than the fixed diameter, the oscillation of the RF field required by Maxwell equations will be restricted to the longitudinal direction and excellent uniformity of the RF field in any of the transverse slices can be achieved. (In the limit of infinite length, the uniformity is perfect.)

In the long-coil limit, the electromagnetic fields inside approach a TEM mode. In this limit, the current and charge distributions on the coils have the same sinusoidal azimuthal dependence, $\sin \varphi$ as found for the low-frequency birdcage, both yielding internal magnetic fields that are spatially uniform and pointing along the x -axis. Let us see how this sinusoidal azimuthal dependence arises from waveguide theory, where it is well known [17] that, for a TEM wave, Maxwell equations become

$$\nabla_t^2 \begin{Bmatrix} \mathbf{E} \\ \mathbf{B} \end{Bmatrix} = \left(\nabla^2 - \frac{\partial^2}{\partial z^2} \right) \begin{Bmatrix} \mathbf{E} \\ \mathbf{B} \end{Bmatrix} = 0. \quad (11)$$

This means that the electric field is a solution of a two-dimensional electrostatic-like problem in the transverse plane perpendicular to the wave propagation direction. Although the TEM mode cannot exist inside a single hollow (good) conductor, which generates an equipotential surface, it can be supported with two or more conductor surfaces such as a coaxial cable or transmission line, or a surface around which the potential is not constrained to be constant. Suppose a cylinder is formed by such surfaces, and a TEM electromagnetic wave (which can be either a standing wave or a traveling wave) exists in this cylinder such that the electric and magnetic fields in any transverse plane are uniform. For example, suppose a spatially uniform magnetic field points along the x -axis and a spatially uniform electric field points along the y -axis. At the surfaces, the electric and magnetic fields must satisfy the familiar boundary discontinuity conditions

$$\begin{aligned} (\mathbf{E}_{\text{out}} - \mathbf{E}_{\text{in}}) \cdot \mathbf{n} &= \frac{\sigma}{\epsilon_0}, \\ \mathbf{n} \times (\mathbf{B}_{\text{out}} - \mathbf{B}_{\text{in}}) &= \mu_0 \mathbf{K}, \end{aligned} \quad (12)$$

where \mathbf{E}_{in} and \mathbf{E}_{out} (\mathbf{B}_{in} and \mathbf{B}_{out}) represent the electric (magnetic) fields inside and outside the surface, respectively,

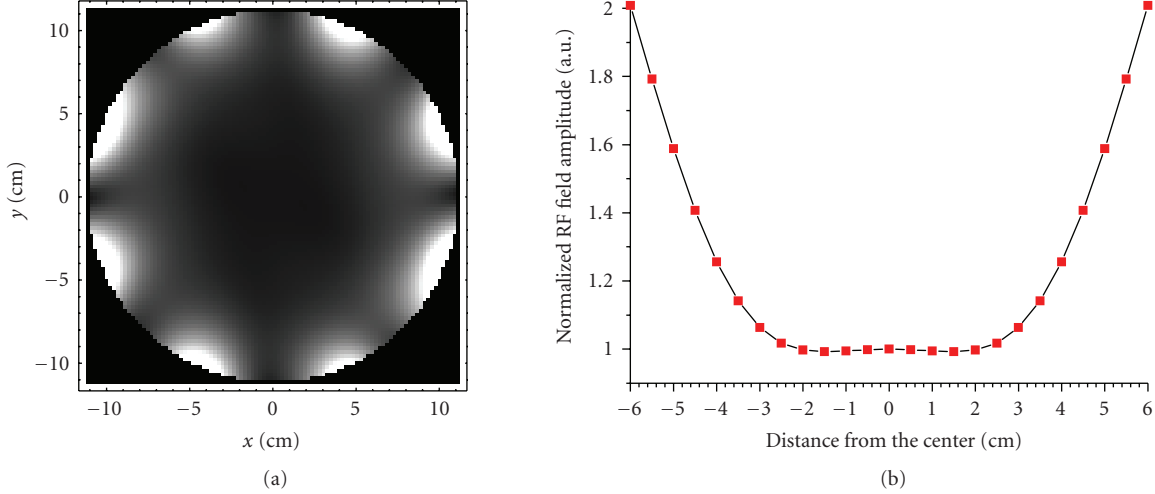


FIGURE 6: Amplitude of the RF field in the central axial plane (a) and across the diameter along the horizontal (x) direction (b) for the optimized multisegmented birdcage model.

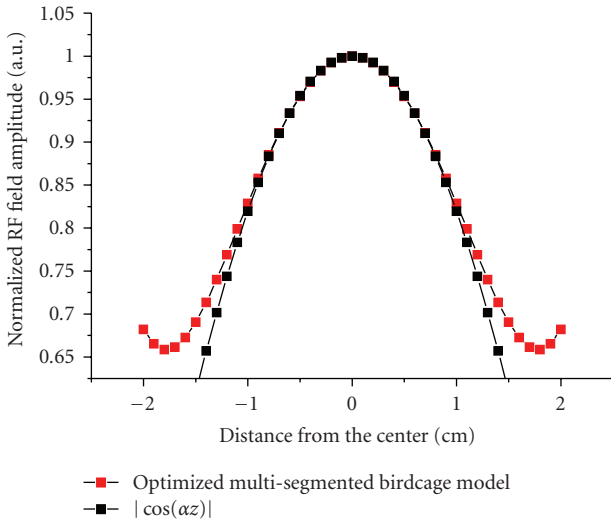


FIGURE 7: RF field variation along the longitudinal (z) direction of the optimized multisegmented birdcage model.

$\sigma(\mathbf{K})$ is the surface electric (current) density, and the normal (to the surface) vector \mathbf{n} points from the inside of the cylinder toward the outside of the cylinder. In the case where the electric and the magnetic fields outside the coil are zero, and the electric (magnetic) field is uniform inside the cylinder and along the y -axis (x -axis), we have

$$\begin{aligned} (0 - E_0 \mathbf{e}_y) \cdot (\cos \varphi \mathbf{e}_x + \sin \varphi \mathbf{e}_y) &= \frac{\sigma}{\epsilon_0}, \\ (\cos \varphi \mathbf{e}_x + \sin \varphi \mathbf{e}_y) \times (0 - B_0 \mathbf{e}_x) &= \mu_0 \mathbf{K}, \end{aligned} \quad (13)$$

where E_0 (B_0) is the magnitude of the spatially uniform electric (magnetic) field, \mathbf{e}_x and \mathbf{e}_y are unit vectors pointing, respectively, along the x and y directions, and φ is the azimuthal angle. It can be seen that the azimuthal distribution of the electric charge and the surface current density are

both proportional to $\sin \varphi$ where φ is the azimuthal angle, and the direction of the current flow points along the z direction. These results are consistent with our calculations.

Although an infinitely long birdcage model with conventional sinusoidal current distribution can support a perfectly uniform TEM mode, a short one with length comparable to a normal RF head coil can not. Therefore, we have constructed a multisegmented birdcage model with a large number of center-fed dipole antenna RF elements. Each of the original axial conductors in the single-segmented birdcage model is now replaced by five equal subsegments in our example. With our analytical tools the RF field can be calculated and optimized. The optimal RF field shows excellent central planar uniformity. In other words, a kind of RF shimming is achievable with our model and theory. Although excellent RF field planar homogeneity is achieved with our optimization process in the central transverse plane, the RF field uniformity degrades rapidly as the transverse plane moves away from the center of the model. It can be seen in Figure 7 that the oscillation of the field coincides with the absolute value of the cosine function only around $z = 0$. It implies that perfect sinusoidal longitudinal (along z) oscillation of the field is approximately restricted to the $z = 0$ region, and, as a result, the (transverse) field within the central transverse plane is approximately uniform. Although in the present solution the planar uniformity of the RF field degrades rapidly as the transverse plane moves away from the center, a similar optimization can be performed over other transverse planes to improve the field uniformity. Although the planar RF field homogeneity is improved, it is noted that the field strength significantly increases toward the periphery of the central axial plane. This is due to large current amplitudes in the antenna RF elements (Table 1). In fact, in our present solution, the uniform field in the central transverse plane is a result of partial cancellations among the fields produced by individual antenna elements. Therefore, the current amplitudes on the

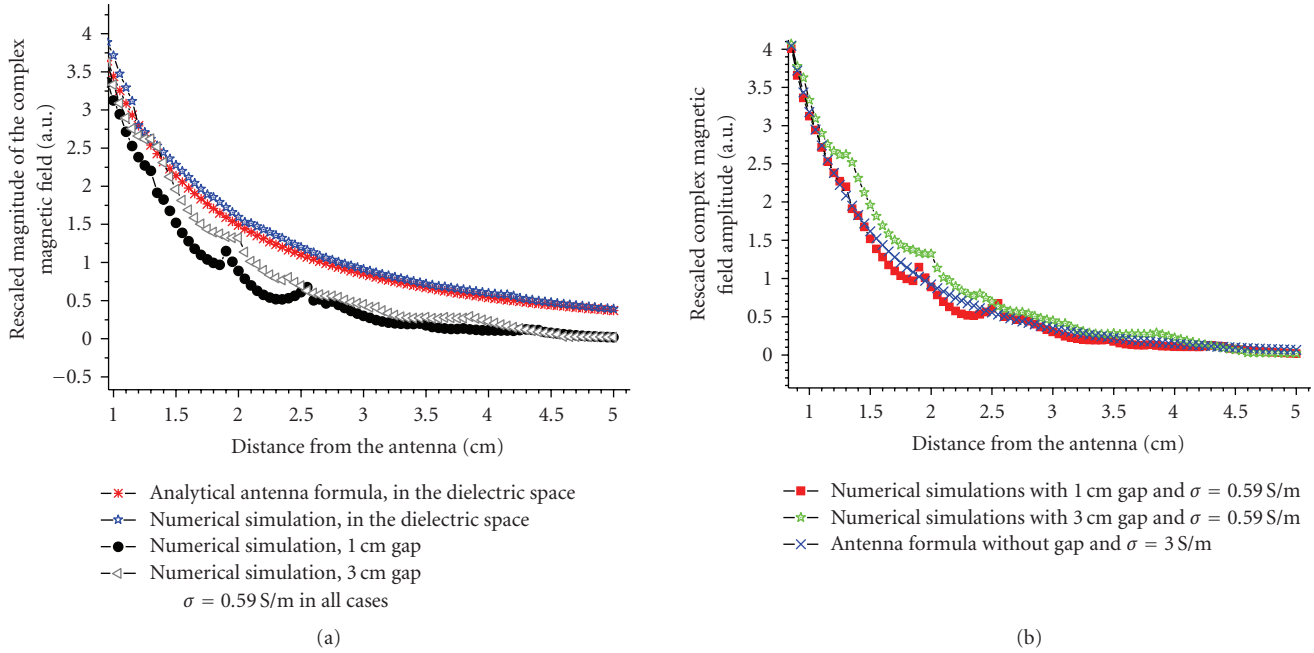


FIGURE 8: Complex magnetic field amplitude calculated with the analytic antenna formula and with the numerical simulation under different conditions. The field strength is rescaled for comparison.

antenna elements tend to increase to produce a reasonable RF field strength in the central region of the axial plane. The increased currents lead to stronger both magnetic and electric fields at the periphery. As a result, the average SAR is bigger than results presented in some other numerical simulations such as [21]. It is difficult to reduce the SAR under the constraints demanding uniform RF field. In order to address this problem, we may perform the optimization process in a smaller region of interest to balance the RF field homogeneity and the SAR. In our present model, we have assumed a current distribution that oscillates with a dielectric wavelength to make an analytic solution possible. In fact, with the more general endpoints for our sinusoidal current z -profile formula, by superposition treating different kinds of the current z -profiles, we can approximate, for example, a more uniform current z -profile.

In our modeling, we have assumed that the dielectric fills up the whole of space instead of assuming a layer of air between the coil and a cylindrical dielectric phantom [5–8] or using a heterogeneous head model [9–11]. We make this approximation mainly for simplifying our analytic calculations. To estimate the error of this approximation, we performed numerical simulations with HFSS (Ansoft Corporation) to study the RF field produced by our building blocks (half-wave-length-long center-fed dipole antennas) under several different conditions. Figure 8(a) shows the amplitude of the complex magnetic field at $z = 0$ as a function of the radial distance from a half-wavelength-long center-fed dipole antenna aligned along the z -axis with its center at the origin (as shown in Figure 2). The fields are rescaled such that they are identical 0.8 cm away from the antenna. Fields under the following conditions are plotted:

(i) fields calculated with our analytic antenna formula with a dielectric filling up the whole space, (ii) fields calculated with numerical simulations with a dielectric filling up the whole space, (iii) the antenna is located coaxially 12.5 cm from the central axis of a dielectric cylinder with radius 11.5 cm (i.e., there is a 1 cm air gap between the antenna and the surface of the cylinder), and (iv) the antenna is located coaxially 12.5 cm from the central axis of a dielectric cylinder with radius 9.5 cm (i.e., there is a 3 cm air gap between the antenna and the surface of the cylinder). It is shown that with the dielectric properties of an average human head, there is an excellent agreement between the analytic antenna formula and the numerical simulations without the presence of any air gap. The error introduced by the approximation that ignores the air gaps is an overall scaling difference of the field strength as long as the field is not estimated close to the antenna (typically, at least 2 cm away from the antenna). The very interesting point is that, by adjusting the conductivity to 3 S/m, the antenna formula and the “dielectric space” assumption can provide an excellent fit to the field distribution obtained with numerical simulation where there is an air gap between the antenna and the dielectric cylinder, as shown in Figure 8(b). These results suggest that the analytic antenna formulae are useful for modeling practical RF coils. Although further calculations can be performed to address the problem with different layers of dielectric, our present results illustrate how RF field inhomogeneity is caused by the so-called wavelength effect and the manner in which we can achieve a desired RF field pattern through RF shimming. In a more realistic, heterogeneous case, improved RF field homogeneity can be anticipated using the present antenna solution as input

followed by numerical algorithms in an iteration procedure, in order to converge to a better approximation.

Finally, the question arises about the construction of an RF coil based on our model and theory. Although our present model has a total number of 40 antenna RF elements, these elements are not independent. First of all, the aforementioned symmetry with respect to the central axial plane of the multisegmented birdcage model reduces the number of independent current sources from $5 \times 8 = 40$ to $3 \times 8 = 24$. Furthermore, the current amplitudes found with the optimization (as shown in Table 1) have certain symmetry such that the current amplitude of one antenna element is always identical to the current amplitude of the antenna element diagonal to it. Although current phases do not exhibit any specific symmetry, the optimal solution may lead to further reduction of independent current sources. While the purpose of the present work is to present a theoretical tool for an initial optimization, there are multiple solutions to the practical problems. For example, with respect to decoupling in transmit mode, we could start with overlapping the nearest neighbor coils and then add combinations of capacitive or inductive elements for the decoupling of the remaining (next nearest neighbor and beyond) interactions. In particular, the present multisegmented birdcage model, in any case, can be implemented as a “parallel transmit volume coil with independent control of currents on the array elements” [22]. The techniques presented in [22] can be applied to address the problems of decoupling and feeding for constructing a practical coil based on the present model.

5. CONCLUSION

Due to the shortened wavelength of the RF field, RF field inhomogeneity has become a major challenge for high-field MRI. We present an analytic tool to simulate the RF field in the appropriate high-frequency limit. It is shown that an analytic calculation based on antenna theory and an optimization on that modeling can be effectively carried out. RF shimming is achievable to produce RF field with excellent planar uniformity. Our model and analytical calculations can help understand the relationship between the current sources and the RF fields. The major advantage of the present analytic tools is efficiency; for instance, the calculations are much faster than numerical iterative algorithms (by orders of magnitude in comparisons with field calculations performed through numerical integrations). Important parameters such as SAR can also be incorporated into the calculation and optimization. We believe that the methods described here will be quite useful in future RF coil designs.

ACKNOWLEDGMENTS

The authors are grateful to Shmaryu Shvartsman for helpful discussions. They would like to thank Mark Griswold and Jeremy Heilman for discussing practical coil designs based on The authors model. This work is supported by the State of Ohio Third Frontier initiative.

REFERENCES

- [1] J. T. Vaughan, M. Garwood, C. M. Collins, et al., “7T vs. 4T: RF power, homogeneity, and signal-to-noise comparison in head images,” *Magnetic Resonance in Medicine*, vol. 46, no. 1, pp. 24–30, 2001.
- [2] J. T. Vaughan, H. P. Hetherington, J. O. Otu, J. W. Pan, and G. M. Pohost, “High frequency volume coils for clinical NMR imaging and spectroscopy,” *Magnetic Resonance in Medicine*, vol. 32, no. 2, pp. 206–218, 1994.
- [3] J. T. Vaughan, G. Adriany, C. J. Snyder, et al., “Efficient high-frequency body coil for high-field MRI,” *Magnetic Resonance in Medicine*, vol. 52, no. 4, pp. 851–859, 2004.
- [4] J. Tropp, “Image brightening in samples of high dielectric constant,” *Journal of Magnetic Resonance*, vol. 167, no. 1, pp. 12–24, 2004.
- [5] T. K. F. Foo, C. E. Hayes, and Y.-W. Kang, “Reduction of RF penetration effects in high field imaging,” *Magnetic Resonance in Medicine*, vol. 23, no. 2, pp. 287–301, 1992.
- [6] T. K. F. Foo, C. E. Hayes, and Y.-W. Kang, “An analytical model for the design of RF resonators for MR body imaging,” *Magnetic Resonance in Medicine*, vol. 21, no. 2, pp. 165–177, 1991.
- [7] D. K. Spence and S. M. Wright, “2-D full wave solution for the analysis and design of birdcage coils,” *Concepts in Magnetic Resonance Part B*, vol. 18B, no. 1, pp. 15–23, 2003.
- [8] V. Taracila, L. S. Petropoulos, T. P. Eagan, and R. W. Brown, “Image uniformity improvement for birdcage-like volume coils at 400 MHz using multichannel excitations,” *Concepts in Magnetic Resonance Part B*, vol. 29B, no. 3, pp. 153–160, 2006.
- [9] T. S. Ibrahim, R. Lee, B. A. Baertlein, A. M. Abduljalil, H. Zhua, and P.-M. L. Robitaille, “Effect of RF coil excitation on field inhomogeneity at ultra high fields: a field optimized TEM resonator,” *Magnetic Resonance Imaging*, vol. 19, no. 10, pp. 1339–1347, 2001.
- [10] F. Liu, B. L. Beck, J. R. Fitzsimmons, S. J. Blackband, and S. Crozier, “A theoretical comparison of two optimization methods for radiofrequency drive schemes in high frequency MRI resonators,” *Physics in Medicine and Biology*, vol. 50, pp. 5281–5291, 2005.
- [11] W. Mao, M. B. Smith, and C. M. Collins, “Exploring the limits of RF shimming for high-field MRI of the human head,” *Magnetic Resonance in Medicine*, vol. 56, no. 4, pp. 918–922, 2006.
- [12] P. Ullmann, S. Junge, M. Wick, F. Seifert, W. Ruhm, and J. Hennig, “Experimental analysis of parallel excitation using dedicated coil setups and simultaneous RF transmission on multiple channels,” *Magnetic Resonance in Medicine*, vol. 54, no. 4, pp. 994–1001, 2005.
- [13] H. Fujita, L. S. Petropoulos, M. A. Morich, S. M. Shvartsman, and R. W. Brown, “A hybrid inverse approach applied to the design of lumped-element RF coils,” *IEEE Transactions on Biomedical Engineering*, vol. 46, no. 3, pp. 353–361, 1999.
- [14] H. Fujita, “New horizons in MR technology: RF coil designs and trends,” *Magnetic Resonance in Medical Sciences*, vol. 6, no. 1, pp. 29–42, 2007.
- [15] C. M. Collins, W. Liu, J. Wang, et al., “Temperature and SAR calculations for a human head within volume and surface coils at 64 and 300 MHz,” *Journal of Magnetic Resonance Imaging*, vol. 19, no. 5, pp. 650–656, 2004.
- [16] Z. Wang, J. C. Lin, W. Mao, W. Liu, M. B. Smith, and C. M. Collins, “SAR and temperature: simulations and comparison to regulatory limits for MRI,” *Journal of Magnetic Resonance Imaging*, vol. 26, no. 2, pp. 437–441, 2007.

- [17] J. D. Jackson, *Classical Electrodynamics*, John Wiley & Sons, New York, NY, USA, 3rd edition, 1999.
- [18] C. A. Balanis, *Antenna Theory: Analysis and Design*, Harper & Row, New York, NY, USA, 1982.
- [19] <http://www.fcc.gov/cgi-bin/dielec.sh>.
- [20] J. Jin, *Electromagnetic Analysis and Design in Magnetic Resonance Imaging*, CRC Press, Boca Raton, Fla, USA, 1999.
- [21] C. Wang and G. X. Shen, " B_1 field, SAR, and SNR comparisons for birdcage, TEM, and microstrip coils at 7T," *Journal of Magnetic Resonance Imaging*, vol. 24, no. 2, pp. 439–443, 2006.
- [22] K. N. Kurpad and S. M. Wright, "A parallel transmit volume coil with independent control of currents on the array elements," in *Proceedings of the 13th International Society for Magnetic Resonance in Medicine (ISMRM '05)*, p. 16, Miami, Fla, USA, May 2005.

Research Article

Parallel Solvers for Finite-Difference Modeling of Large-Scale, High-Resolution Electromagnetic Problems in MRI

Hua Wang, Adnan Trakic, Feng Liu, Bing Keong Li, Ewald Weber, and Stuart Crozier

School of Information Technology and Electric Engineering, The University of Queensland, Brisbane, Qld 4072, Australia

Correspondence should be addressed to Stuart Crozier, stuart@itee.uq.edu.au

Received 29 August 2007; Revised 23 January 2008; Accepted 10 April 2008

Recommended by Tamer Ibrahim

With the movement of magnetic resonance imaging (MRI) technology towards higher field (and therefore frequency) systems, the interaction of the fields generated by the system with patients, healthcare workers, and internally within the system is attracting more attention. Due to the complexity of the interactions, computational modeling plays an essential role in the analysis, design, and development of modern MRI systems. As a result of the large computational scale associated with most of the MRI models, numerical schemes that rely on a single computer processing unit often require a significant amount of memory and long computational times, which makes modeling of these problems quite inefficient. This paper presents dedicated message passing interface (MPI), OPENMP parallel computing solvers for finite-difference time-domain (FDTD), and quasistatic finite-difference (QSFD) schemes. The FDTD and QSFD methods have been widely used to model/analyze the induction of electric fields/currents in voxel phantoms and MRI system components at high and low frequencies, respectively. The power of the optimized parallel computing architectures is illustrated by distinct, large-scale field calculation problems and shows significant computational advantages over conventional single processing platforms.

Copyright © 2008 Hua Wang et al. This is an open access article distributed under the Creative Commons Attribution License, which permits unrestricted use, distribution, and reproduction in any medium, provided the original work is properly cited.

1. INTRODUCTION

Recent progress in MRI superconducting technology has lead to a considerable increase in human exposure to very large static magnetic fields of up to several Tesla. A typical commercial MRI scanner has a main field strength between 0.5 Tesla and 4 Tesla (in the region of uniformity). However, MRI systems above 4 Tesla, such as 7 Tesla and 9.4 Tesla, are currently used for research [1–3]. Motion of patients and occupational workers through these fields can cause the induction of currents in the body [4, 5]. In addition, new imaging sequences demand larger amplitudes and switching rates in magnetic field gradients, thus increasing the likelihood of peripheral nerve stimulation (PNS) [6–9]. When radiofrequency fields are transmitted to excite a spin ensemble during imaging, electromagnetic energy is coupled to the tissue and deposited within, which can cause regional temperature elevations within the patient, thus leading to possible tissue/cell injury [10, 11]. Apart from interacting with the patient, electromagnetic fields produced by the system also couple to the conducting materials

in the MRI system to induce eddy currents that degrade image quality [12]. In practice, it is difficult to measure the unperturbed fields/currents in the human numerical prediction of the induced fields, can then be very useful for the evaluation/design of electromagnetic devices. The aim of this study is to improve the performance of the conventional (quasistatic) finite-difference method, which has been extensively used to model the induction of electric fields/currents in inhomogeneous voxel phantoms of man and animal when exposed to oscillating or static magnetic field sources. The method has the advantages of simplicity and can model any shaped object and various excitation sources.

Numerical computational techniques are indispensable components for analyzing, predicting, and obtaining approximate solutions to the real world problems. The finite-difference time-domain (FDTD) method is well suited to high-frequency electromagnetic analyses due to its simplicity and efficiency in wave modeling and the ability to handle field-material interactions and nonlinear phenomena [13]. In contrast, the quasistatic finite-difference (QSFD)

method is ideal for linear low-frequency problems with time-harmonic dependency. One example of this is the modeling of the interaction of magnetic fields due to MRI gradients and main superconducting coils with the patient or occupational worker [14–16].

In recent years, we have developed a series of single processor-based finite-difference schemes [14–24], which can be used to simulate a wide range of problems related to MRI and other environments. Our long term aim is to generate a complete temporal model of an MRI system including all the field generating units, passive system components, and an electrical, voxel model of the patient. A better understanding of the complex temporal interaction of the fields within the patient and the system itself can provide useful insight into system design.

Often, numerical modeling of electromagnetic field—material interactions in MRI requires high-spatial resolution, which imposes a significant computational burden. In solving large-scale-high-resolution (LSHR) models, single processor-based methods are limited and often incapable of managing the required large memory and computational time requirements. Therefore, to improve the performance of these finite difference solvers, it is necessary to further explore computational strategies such as parallelization. Parallel environments such as the message passing interface (MPI), OPENMP, and LAM/MPI have been used in large-scale computational problems [25–27]. Due to the geometrical topology of these problems, finite-difference methods and related hybrid algorithms are very adaptable to parallel computing frameworks, in which the computing task is divided and assigned to many processors with distributed or shared memory allocations. This paper outlines MPI and OPENMP parallel computing solvers dedicated to the FDTD and QSPD method, respectively. In the case of the QSPD scheme, a parallelized conjugate gradient technique is applied to solve the sparse matrix equations typical in these situations. A variety of LSHR problems has been investigated using parallel schemes. Compared to previous single processing algorithms, the proposed parallel platforms offer significant advantages in terms of improved numerical convergence and reduced computing time/memory usage. Some of the problems have been solved at high-spatial resolution, which is beyond the capability of single processing methods.

2. METHODOLOGY

2.1. Parallel Cartesian and cylindrical FDTD methods

Maxwell's equations can be expressed in Cartesian or cylindrical coordinate systems with components of the magnetic \vec{H} and electric field \vec{E} intensity formulated in a general form [28], as given by the following expressions:

$$H_A \Big|_{i,j+1/2,k+1/2}^{n+1/2} = C_{h1} H_A \Big|_{i,j+1/2,k+1/2}^n + C_{h2} \left(\frac{E_B \Big|_{i,j+1/2,k+1}^n - E_B \Big|_{i,j+1/2,k}^n}{\Delta C} - \frac{E_C \Big|_{i,j+1,k+1/2}^n - E_C \Big|_{i,j,k+1/2}^n}{r_i \Delta B} \right),$$

$$\begin{aligned} H_B \Big|_{i+1/2,j,k+1/2}^{n+1/2} &= C_{h1} H_B \Big|_{i+1/2,j,k+1/2}^n + C_{h2} \left(\frac{E_C \Big|_{i+1,j,k+1/2}^n - E_C \Big|_{i,j,k+1/2}^n}{\Delta A} - \frac{E_A \Big|_{i+1/2,j,k+1}^n - E_A \Big|_{i+1/2,j,k}^n}{\Delta C} \right), \\ H_C \Big|_{i+1/2,j+1/2,k}^{n+1/2} &= C_{h1} H_C \Big|_{i+1/2,j+1/2,k}^n + \frac{C_{h2}}{r_{i+1/2}} \left(\frac{E_A \Big|_{i+1/2,j+1,k}^n - E_A \Big|_{i+1/2,j,k}^n}{\Delta B} - \frac{r_{i+1} E_B \Big|_{i+1,j+1/2,k}^n - r_i E_B \Big|_{i,j+1/2,k}^n}{\Delta A} \right), \\ E_A \Big|_{i+1/2,j,k}^{n+1} &= C_{e1} E_A \Big|_{i+1/2,j,k}^n + \frac{\Delta t}{\epsilon} J_A \Big|_{i+1/2,j,k}^{n+1/2} + C_{e2} \left(\frac{H_C \Big|_{i+1/2,j+1/2,k}^{n+1/2} - H_C \Big|_{i+1/2,j-1/2,k}^{n+1/2}}{r_{i+1/2} \Delta B} - \frac{H_B \Big|_{i+1/2,j,k+1/2}^{n+1/2} - H_B \Big|_{i+1/2,j,k-1/2}^{n+1/2}}{\Delta C} \right), \\ E_B \Big|_{i,j+1/2,k}^{n+1} &= C_{e1} E_B \Big|_{i,j+1/2,k}^n + \frac{\Delta t}{\epsilon} J_B \Big|_{i,j+1/2,k}^{n+1/2} + C_{e2} \left(\frac{H_A \Big|_{i,j+1/2,k+1/2}^{n+1/2} - H_A \Big|_{i,j+1/2,k-1/2}^{n+1/2}}{\Delta C} - \frac{H_C \Big|_{i+1/2,j+1/2,k}^{n+1/2} - H_C \Big|_{i-1/2,j+1/2,k}^{n+1/2}}{\Delta A} \right), \\ E_C \Big|_{i,j,k+1/2}^{n+1} &= C_{e1} E_C \Big|_{i,j,k+1/2}^n + \frac{\Delta t}{\epsilon} J_C \Big|_{i,j,k+1/2}^{n+1/2} + \frac{C_{e2}}{r_i} \left(\frac{r_{i+1/2} H_B \Big|_{i+1/2,j,k+1/2}^{n+1/2} - r_{i-1/2} H_B \Big|_{i-1/2,j,k+1/2}^{n+1/2}}{\Delta A} - \frac{H_A \Big|_{i,j+1/2,k+1/2}^{n+1/2} - H_A \Big|_{i,j-1/2,k+1/2}^{n+1/2}}{\Delta B} \right), \end{aligned} \quad (1)$$

where $A = x(r)$, $B = y(\varphi)$, and $C = z$ for Cartesian (cylindrical) coordinates $\Xi = (A, B, C)$. The variable r_ξ ($\xi \in \{i, i + 1/2, i - 1/2, i + 1, i - 1\}$) is the radial displacement [in meters] employed in the cylindrical FDTD method. For the Cartesian FDTD method, $r_\xi = 1$ for all values of ξ . In the discrete FDTD computational domain, the dimensions

of the Yee cell are defined by ΔA , ΔB , and ΔC . The relative permeability $\mu(\Xi)$, relative permittivity $\epsilon(\Xi)$, and material conductivity $\sigma(\Xi)$ are assigned at the center of the Yee cell. Parameter J_{Ξ} signifies the impressed current density [in Am^{-2}]. The FDTD update coefficients are space-dependent and can be written as follows:

$$\begin{aligned} C_{h1} &= 1, & C_{h2} &= \frac{\Delta t}{\mu}, \\ C_{e1} &= \begin{cases} \frac{2\epsilon - \sigma\Delta t}{2\epsilon + \sigma\Delta t}, & \omega \in \text{RF}, \\ \exp\left(\frac{-\sigma\Delta t}{\epsilon}\right), & \omega \in \text{LF}, \end{cases} \\ C_{e2} &= \begin{cases} \frac{2\Delta t}{2\epsilon + \sigma\Delta t}, & \omega \in \text{RF}, \\ \frac{1 - \exp(-\sigma\Delta t/\epsilon)}{\sigma}, & \omega \in \text{LF}, \end{cases} \end{aligned} \quad (2)$$

where ω is the angular frequency. The abbreviations RF and LF denote radiofrequency and low frequency, respectively. The parameter Δt is the FDTD time step, which in general coordinate notation, is limited by the Courant-Friedrich-Levy (CFL) stability condition

$$\Delta t < \frac{k_t \sqrt{\mu_0 \epsilon}}{\sqrt{(1/\Delta A)^2 + (1/r_{\text{MIN}} \Delta B)^2 + (1/\Delta C)^2}}, \quad (3)$$

where μ_0 and ϵ are the permeability and permittivity of free space, respectively, k_t is the safety coefficient that ensures numerical stability, and r_{MIN} is the minimal radial component to be studied (here: $r_{\text{MIN}} = 0.5\Delta r$). In the Cartesian coordinate system, $r_{\text{MIN}} = 1$. During the updating of the E-field components, the coefficients are linear for the RF case and nonlinear for modeling exponential decay of propagating waves inside good conductors at LF. In LF applications, the conventional FDTD method suffers from prohibitively long computational time [20]. The weakly coupled-Maxwell's equations can be adapted to the low-frequency regime by downscaling the speed of light constant, which permits the use of larger time steps while maintaining the validity of the CFL stability condition. In our recent study, this modification was accomplished by scaling up the permittivity of free space ϵ_0 by a scaling factor α : $\epsilon = \epsilon_r(\alpha\epsilon_0)$. It is clear that when $\alpha = 1$, the conventional FDTD methodology for RF applications is obtained. In the cylindrical formulations, the numerical singularity associated with the polar axis ($r = 0$) needs to be considered. A series expansion provides an approximation in the radial direction that satisfies regularity conditions. The combination of cylindrical and Cartesian FDTD methods for both LF and HF applications can be particularly powerful. For instance, the cylindrical FDTD method is particularly suitable for modeling of problems with cylindrical symmetry such as the generation of eddy currents in a conducting cryostat vessel during magnetic field gradient pulsing or the interaction of EM fields produced by radiofrequency resonators and surrounding system materials. The Cartesian

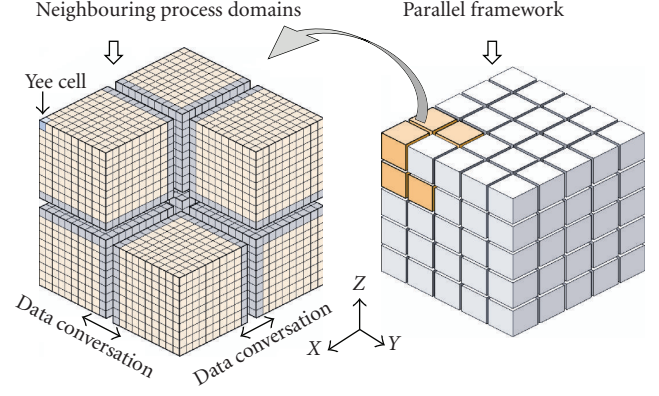


FIGURE 1: Schematic representation of a parallel network with 125 process domains; transmission of field data between neighbouring processes is indicated.

FDTD method allows one to evaluate the electromagnetic wave propagation through tissue-equivalent body models. These FDTD algorithms can be easily adapted to a parallel architecture with the MPI library. With its reputed stability, optional communication routines, and robust compatibility, MPI is considered to be one of the prominent environments to support parallel computing.

In FDTD, the problem space has to be specifically defined before the field calculations commence. In the parallel framework, the computational space is divided into several domains of approximately equal size (see Figure 1) and each domain is managed by one process. All processes run on several processors and execute the same program, while each process operates on memory (computational) domain that is specifically allocated to it. Therefore, mutual access to the memory among the parallel processors is often not straightforward and requires management. With FDTD, additional memory can be assigned to boundary regions of computational subdomains to maintain a smooth transition between neighbouring EM fields on these interfaces. In addition, communication routines can be applied between the neighbouring processes to transmit the E- and H-field components with the consideration of the half time-step difference of these two fields to maintain unified electromagnetic field propagation throughout the entire computational space. Within the MPI frame, a load-balancing scheme is often desired to manage the task distribution in the processing network to improve the computational efficiency.

2.2. Parallel BiCG method for QSFD scheme

At low-source frequencies, where the dimensions of the material medium are small compared to the wavelength, the induced fields can be treated quasistatically. According to Faraday's law, the electric field \vec{E} in a conducting sample is induced by a time varying magnetic field \vec{H} due to a source. In terms of electric and magnetic potentials, the total electric field inside the body model can be split into primary field \vec{E}_1

coefficients are also assigned to air elements that neighbor elements of the problem space (i.e., those that have nonzero conductivities), thus resulting in sparsity of matrix A in this linear system. BICG requires computing a matrix-vector product and a transpose product. In certain applications, the latter product may be impossible to perform, for example, if the matrix is not formed explicitly and the regular product is only given in operation form, as a function call evaluation. In a parallel computing environment, the two matrix-vector products can be performed simultaneously. However, in a distributed memory environment, there will be extra communication costs associated with one of the two matrix-vector products, depending upon the storage scheme for A . A duplicate copy of the matrix alleviates this problem, at the cost of doubling the storage requirements for the matrix. A shared memory parallel scheme OPENMP is applied in this case. Without having duplicates on each subprocess, multiple threads compute on one allocated memory. In that way, one can control the number of processing threads to maximize efficiency.

2.3. Practical applications

2.3.1. The RF FDTD application examples

(a) Rotary phased array head coil—spherical phantom

To demonstrate the performance of the parallel FDTD method, we investigate a new type of receive-only, 4-element rotary phased array (RPA) head coil that is designed to improve the sensitivity profile at the center of the sample. Shown in Figure 2(a) is the modeled RPA head coil loaded with a spherical phantom. To mimic a simple head model, it was assumed that the FDTD-modeled spherical phantom has a conductivity of 0.616 Sm^{-1} and permittivity of 48.8 Fm^{-1} [31]. Each coil element has a “paddle-like” structure consisting of two main conductors. The main conductors of each coil element will carry equal currents but in opposite directions, as a result, each coil element will produce a plane of maximum sensitivity along the axis of the cylindrical space. That is, the plane of sensitivity of each coil element will cut radially or diametrically through the cylindrical space thus improving the sensitivity at the center of the head coil. The method of moments (MoM) available from a commercial software package FEKO is firstly used to model the RPA head coil and also to ensure that coil elements are decoupled, tuned, and matched to 85 MHz. In addition, MoM is used to calculate the initial Huygens equivalent surface sources. Once the initial Huygens equivalent surface sources are obtained and mapped onto FDTD discrete domain, the iteration process commences and is carried out until convergence is achieved. B_1 fields at the mid-section of the spherical phantom, corresponding to each individual decoupled coil element of the RPA head coil, are calculated and thereafter used for calculating the signal intensity (SI) profiles. The calculated SI profiles are used for comparison with the MR images obtained from the prototype RPA head coil. After obtaining positive simulation results, a prototype RPA head coil was constructed. Shown in Figure 2(b) is the

constructed prototype RPA head coil loaded with a spherical phantom. The prototype RPA head coil was tested in a Bruker S200 2T whole-body MRI system, equipped with four receiver channels. Using a MSME pulse sequence with $\text{TR} = 1000 \text{ msec}$, $\text{TE} = 19.3 \text{ msec}$, and $\text{NEX} = 1, 4$ axial slices located at the mid-section of the spherical phantom were acquired in parallel by each coil element of the RPA head coil. For cylindrical FDTD modeling, both the conventional single processing and the new parallel FDTD methods were employed and their computational performances compared.

The parallel cylindrical FDTD method was implemented on a 3-server cluster network, each with 2 XEON 3.6 GHz processors and 4 GB of memory, using an MPI library and managed by a MPICH parallel computing platform. In contrast, the single processing FDTD framework was evaluated on a 3 GHz/1 GB RAM single-CPU machine, which presents identical computing performance on servers. Due to multiuser stimulation, it is very hard to find the best environment to test the single processor FDTD simulation in our server, so we reported the comparison in this way.

(b) Birdcage resonator—human body model

To further demonstrate the enhanced computing power, we have subjected the parallel Cartesian FDTD algorithm to a very high-spatial resolution of 1 mm. For this purpose, the tissue-equivalent male whole-body models from the Brooks Air force Database [32] at spatial resolutions of 1 mm and 4 mm were chosen. The models were subjected to radiofrequency fields generated by a 16-rung whole-body birdcage (volume) resonator operating at 340 MHz (8 Tesla). The dielectric properties of all body-identified tissue types are frequency scaled and kept constant at the designated frequency [33]. At high frequencies, it is impossible to have a global uniform flip angle in the whole imaging slice, field focusing scheme is therefore implemented. The input power of the birdcage resonator is numerically adjusted (a scaling is done to the fields) to provide an averaged 90-degree flip angle in the subregion of the abdomen and chest, such as the heart. The space domain enclosing the birdcage resonator, perfectly matched layers (PML) and the human phantom was modeled with $626 \times 380 \times 1918$ cells at 1 mm and $186 \times 135 \times 510$ cells at 4 mm resolution. After the steady-state is obtained, the specific absorption rate (SAR) is computed using the following equation:

$$\text{SAR}(\Xi) = \frac{\sigma(\Xi) |E(\Xi)|^2}{2\rho(\Xi)}, \quad (11)$$

where $\Xi = (A, B, C)$ is the coordinate of the voxel in designated coordinate system, σ is the conductivity of tissue (Sm^{-1}), E is the peak recorded electric field intensity (Vm^{-1}), and ρ is the specific mass density of tissue (kgm^{-3}).

The models were implemented on an SGI high-performance computer (HPC) with 10 computing nodes, where each node is equipped with 2 Itanium 2nd CPU 1.5 GHz and 4 GB of memory. The 1 mm- and 4 mm-resolution cases were performed using 10 and 5 computing nodes, respectively.

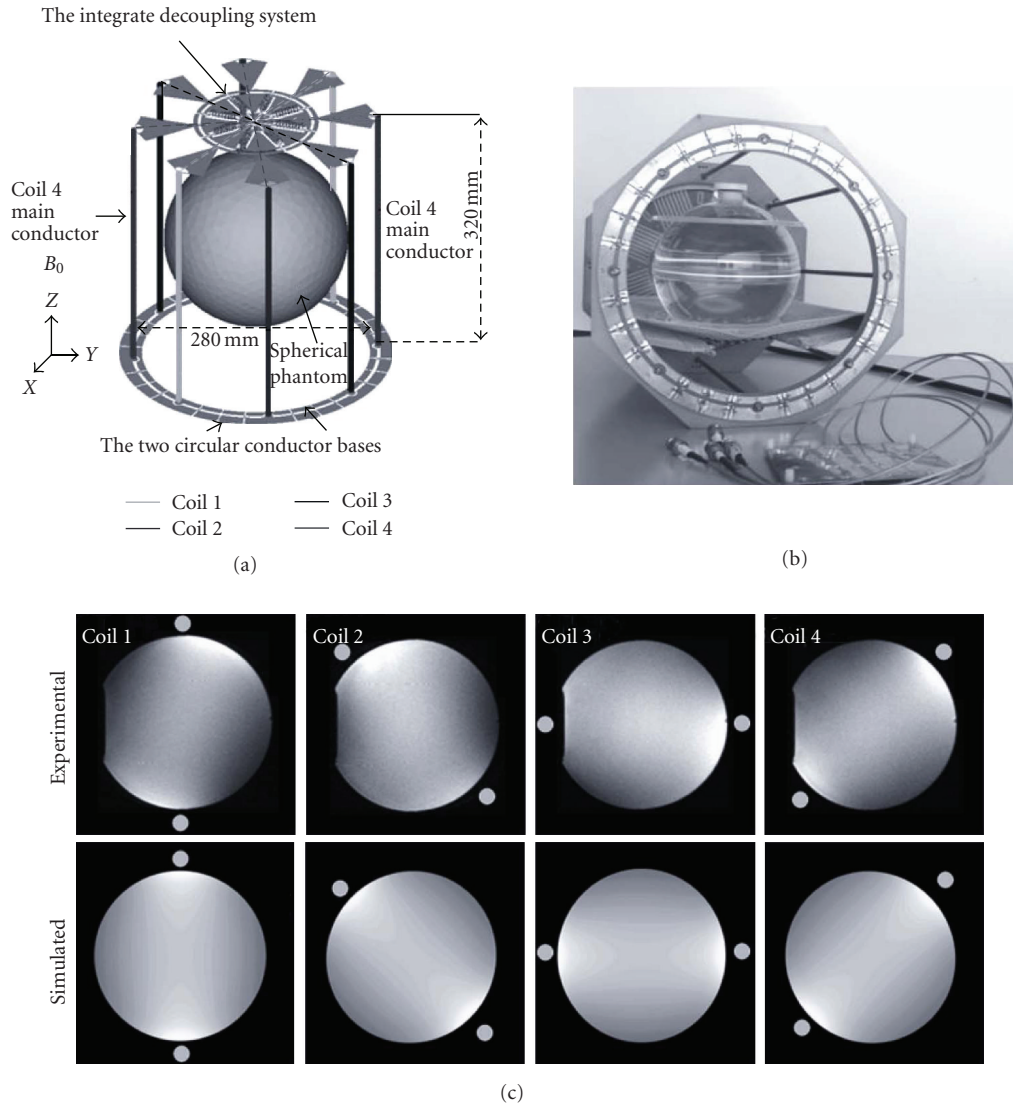


FIGURE 2: (a) FDTD model setup of the RPA head coil and spherical phantom, (b) prototype RPA coil and (c) Signal intensities corresponding to each coil element evaluated with the FDTD method and obtained experimentally during MR imaging.

2.3.2. The QSFD application example

When MRI operators (radiographers or MR technicians) attend anxious, sedated, or intubated patients during an MRI exam, they can be repeatedly exposed to switched magnetic field gradients near the bore entrance at the imager end [5]. In this study, we use the QSFD-BiCG method to evaluate the exposure of an MRI occupational worker in the vicinity of the MRI machine. In particular, the computational performance of the single processing versus parallel QSFD method is assessed.

(a) Body models

Anatomically, accurate whole-body voxel models of male (BROOK) and female (NAOMI, [33]) are used to represent the occupational workers. The female model was engaged at different voxel resolutions to study the computational

performances of the single processing and parallel QSFD method. The scales of the female model in Cartesian dimensions were $277 \times 148 \times 871$, $147 \times 62 \times 396$, $98 \times 42 \times 264$, and $74 \times 31 \times 198$ (in x, z , and y) at model resolutions of 2 mm, 4 mm, 6 mm, and 8 mm, respectively. In a computationally extreme case, the male model was studied at an ultra-high resolution of only 1 mm, whereby the scales of the model in Cartesian dimensions were $586 \times 340 \times 1878$. The experimentally-determined conductivity values by Gabriel et al. [34] of some forty body-identified tissue types were aptly scaled to the frequency of interest and assigned to the appropriate body voxels.

(b) Gradient coils

An actively-shielded whole-body assembly, consisting of the x -, y -, and z -axis gradient coil is used to evaluate the

electric fields and current densities induced in the worker during gradient switching [12, 35]. For mere demonstration purposes, all three gradient coils have been designed to have approximately same axial length of ~ 1.4 m, yet to remain radially separated, that is, the six coil layers (primary and secondary) are allocated to different radii assuming a layer thickness (including former, etc.) of 5 mm. The length of the gradient set is assumed to be of the same length as the imager including the cryostat vessel. Table 1 lists some important parameters while Figure 3(a) illustrates the geometries of the three gradient coils (note that the y -gradient coil is identical to the x -gradient coil when rotated by 90 degrees). It is assumed that each gradient coil generates a normalized gradient field strength of 1 mT/m in the working volume, and that the gradient coil currents are pulsed trapezoidally at the frequency of 1 kHz and 100 microseconds rise time.

(c) Computational setup

Figure 4(a) illustrates a sketch of the position and orientation for both body models near the gradient set end outside the MRI machine. An iterative method based on the SOR algorithm [14–16] and a new parallel BiCG method developed in this study are engaged to compare the numerical convergence and computing performance. All numerical modeling with the parallel QSFD-BiCG method were performed on the aforementioned SGI HPC with 10 computing nodes. Ten subthreads are assigned by the OPENMP scheme. The single processor simulations were performed on the same computing platform with only one computing node assigned.

3. RESULTS AND DISCUSSION

In our experience, numerical studies that involve high-resolution (~ 1 mm) models of human head, pelvis, or other parts of the body have been published. There is, however, no (or lack of) work that involves high-resolution whole-body models, such as 1 mm. This work reports interesting results involving a 1 mm resolution whole-body model, which previously was not possible on single CPU platforms.

3.1. Example RF FDTD applications

(a) Current carrying loop—spherical phantom

Shown in Figure 2(c) are the SI profiles obtained using the MoM/FDTD method and experimentally acquired MR images of the spherical phantom using the prototype RPA head coil. It can be observed that both numerical and experimental results agree well and that the sensitivity at the center of the spherical phantom, as anticipated, has been improved using the RPA head coil. Both the single processing and parallel FDTD methods require around 100 MB RAM and yield identical results. The computing time using the nonparallelized FDTD method was around 182 seconds. In contrast, the parallel FDTD method is around six times faster than the conventional scheme.

(b) Birdcage resonator—human body model

Figure 5(a) shows the model setup involving body and the birdcage resonator. Figure 5(b) compares the specific absorption rate (SAR) at the body-model resolution of 1 mm and 4 mm. Based on the current hardware settings, the whole-body model at 1 mm spatial resolution required approximately 28 GB of memory and 20 hours of computing time for 6000 FDTD iterations to get converged results. The low-resolution simulation (4 mm) required around 500 MB of memory and 1.8 hours of computing time. Compared to spatial SAR distribution at 4 mm, the 1 mm resolution model provides us with clearly more detail and better tissue specificity.

In terms of problem scale, the 1 mm resolution case is around $4^3 = 64$ times larger than the 4 mm simulation. To each processing node involved, the time consumption for 1 mm processing is only about 11 times larger than for the lower-resolution case, which illustrates the higher-computational efficiency of the parallel scheme.

The single processing FDTD routine at 1 mm resolution could not be implemented due to the very large amount of memory required. In this sense, the parallelism cannot only improve the computational efficiency of FDTD, but enable it to solve those problems that conventional FDTD cannot. In the parallel FDTD computing framework, data communication occupies much less time than the computation of E-H field components. Thus, implementations with extensive task distribution can improve computational efficiency, but the additional communication overhead may affect the overall performance. In theory, the time complexity is inversely proportional to the number of parallel threads, provided there is enough random access memory (RAM) and CPU processing resources. With the inevitable communication overhead imposed on the individual processes, however, execution efficiency is often significantly diminished. A load-balancing scheme is applied in the parallelization to reduce the latency time between subprocesses which eventually alleviates both the data conflicts and iterative latency in the data transmission. This parallel FDTD scheme has remarkable computing advantages over conventional single processing methods, which could be also seen in many other parallel computing scenarios though in different applications [25–27].

3.2. Example QSFD application

Figure 4(a) depicts the typical posture of the radiographer on the side of the patient bed, which was used in the QSFD computation. Figure 4(b) represents the spatial distributions of the in situ electric field and current density-induced in the female model during the exposure to the combination of switched gradient coils. Figure 4(c) shows a comparison of the induced average current density versus superior-inferior axis obtained using the parallel BiCG and SOR.

Although the large-scale model used is very inhomogeneous and the source field varies dramatically in the spatial domain, both methods provided remarkably similar simulation results in terms of resulting field magnitudes and

TABLE 1: Geometrical properties of gradient coils.

Parameters	X-gradient	Y-gradient	Z-gradient
1st layer -Z[m]	1.18	1.20	1.29
2nd layer -Z[m]	1.37	1.40	1.40
1st layer -R[m]	0.31	0.32	0.33
2nd layer -R[m]	0.36	0.37	0.39
DSV: $r[\text{m}] \times z[\text{m}]$	0.42×0.42	0.42×0.42	0.50×0.56

Note: Z denotes axial length and R denotes the radius of the primary and secondary gradient coil layers. The DSV size is given as the region where the gradient field is uniform to 5% peak-peak and is expressed as diameter by length in meters.

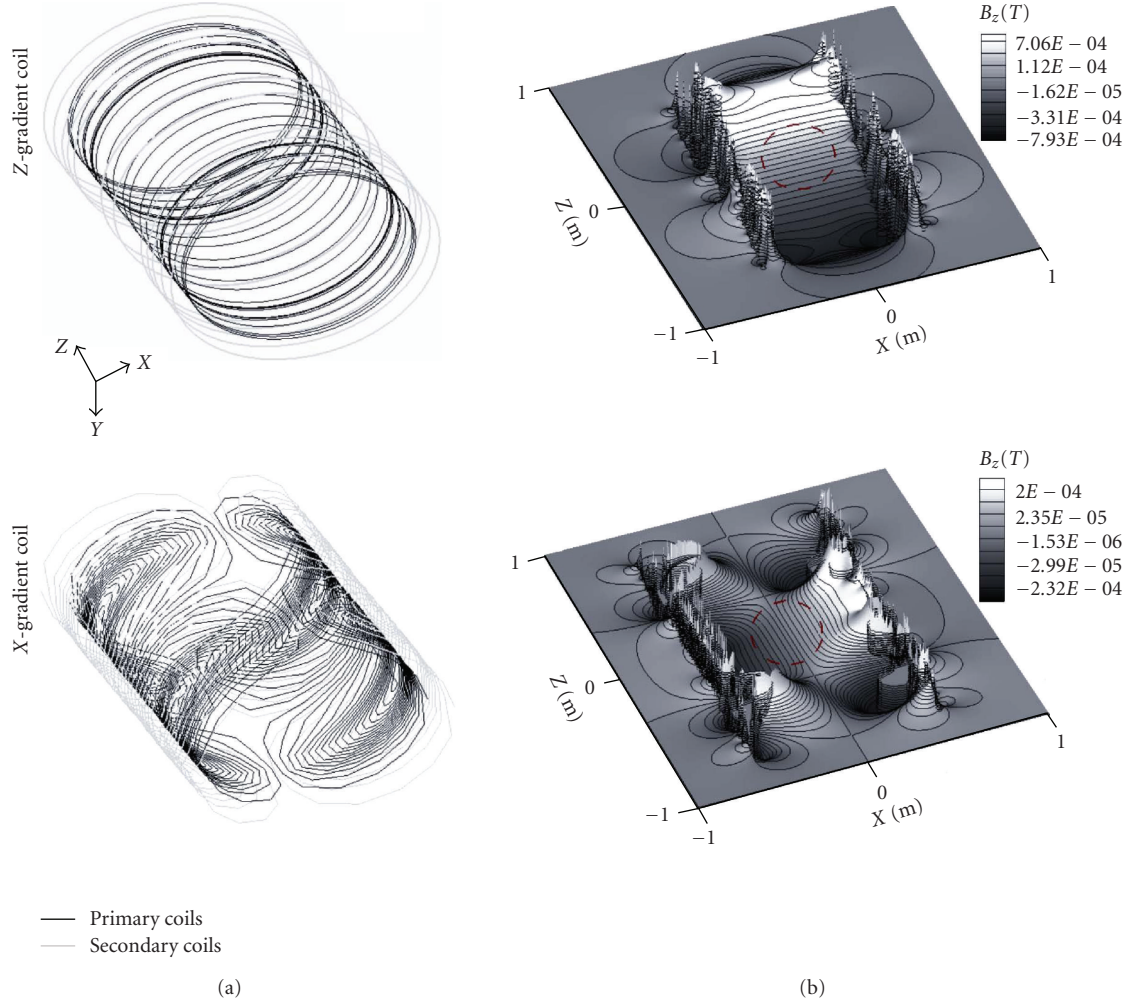


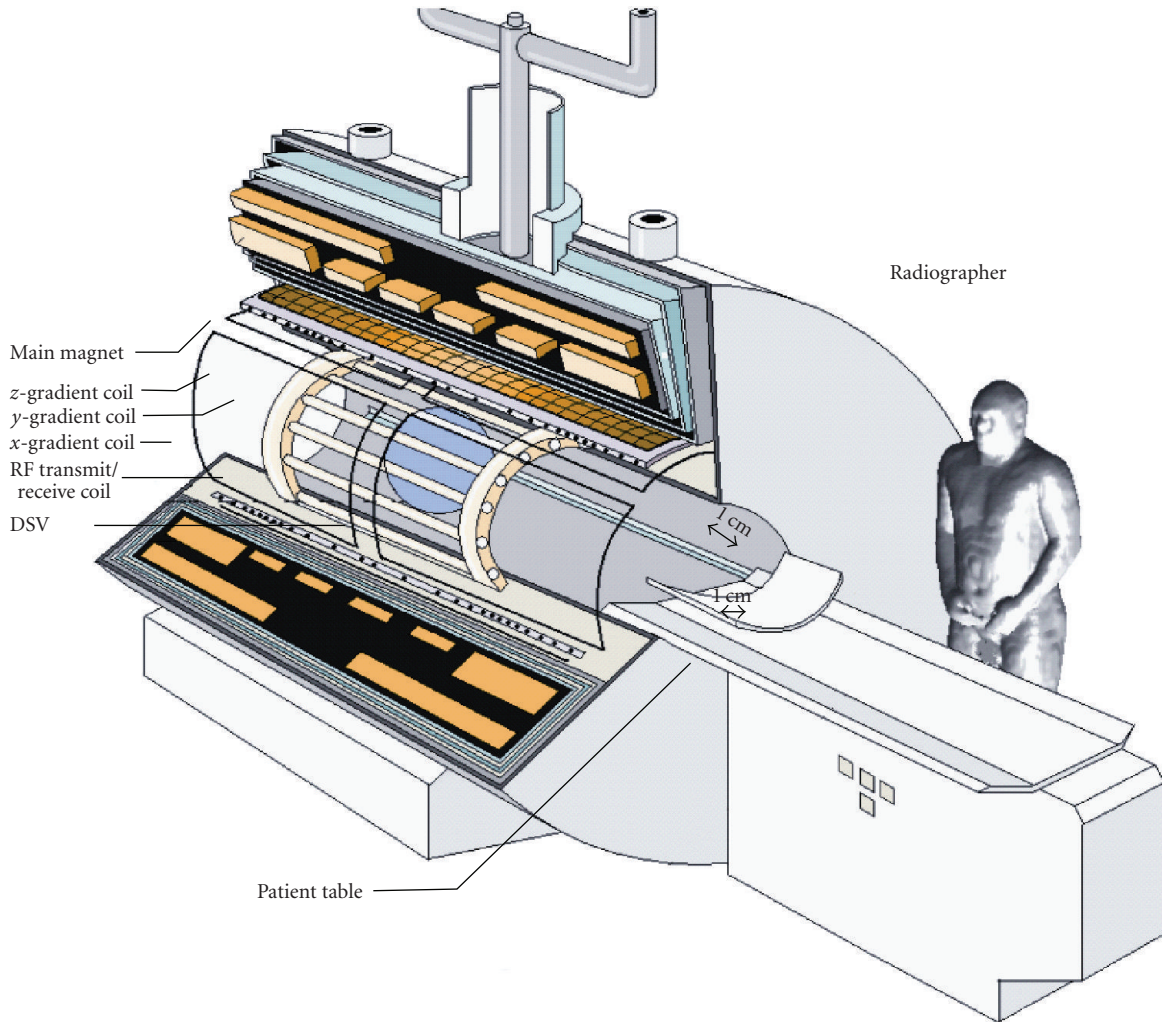
FIGURE 3: (a) Three-dimensional plot of transverse and longitudinal gradient coil geometry (the primary and secondary windings are indicated in black and grey, resp.) and (b) corresponding spatial gradients of B_z . DSV is the diameter spherical volume.

spatial distributions, with less than 1% relative difference. According to the convergence performance results detailed in Table 2, the QSFD-BiCG method clearly outperforms the SOR-based QSFD technique at all nominated resolutions of the female body model.

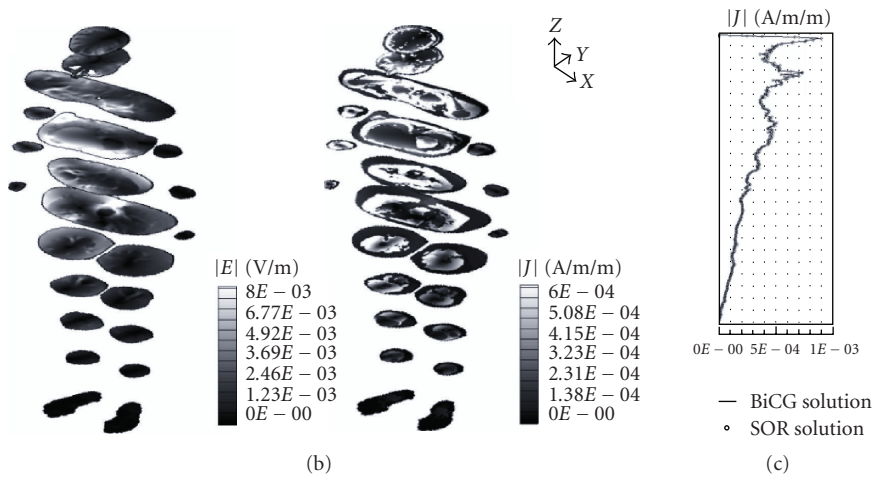
According to Table 2, the coefficient matrix dimension grows dramatically up to 8 million elements with 2 mm resolution, which brings about tremendous computational burdens. Via the computing parallelization, both SOR and

BiCG methods have been improved, while the latter shows better convergence performance.

Using the 1 mm resolution male body model, the parallel QSFD-BiCG method took around 23 hours and 28 GB of RAM to evaluate in situ electric fields/currents. The number of elements in matrix A was $\sim 1.4 \cdot 10^{17}$. In contrast, the single processing equivalent was unable to perform this particular simulation due to immense memory requirements. This example demonstrates one of the clear advantages of the



(a)



(b)

(c)

FIGURE 4: (a) Typical body posture near the imager where gradient coils are assumed to be pulsed as described in the text, (b) axial slices illustrating the spatial distributions of induced electric field and current density and (c) comparison of the average current density along the superior-inferior axis between the QSF-D-BiCG and QSF-D-SOR methods indicating less than 1% of relative deviation.

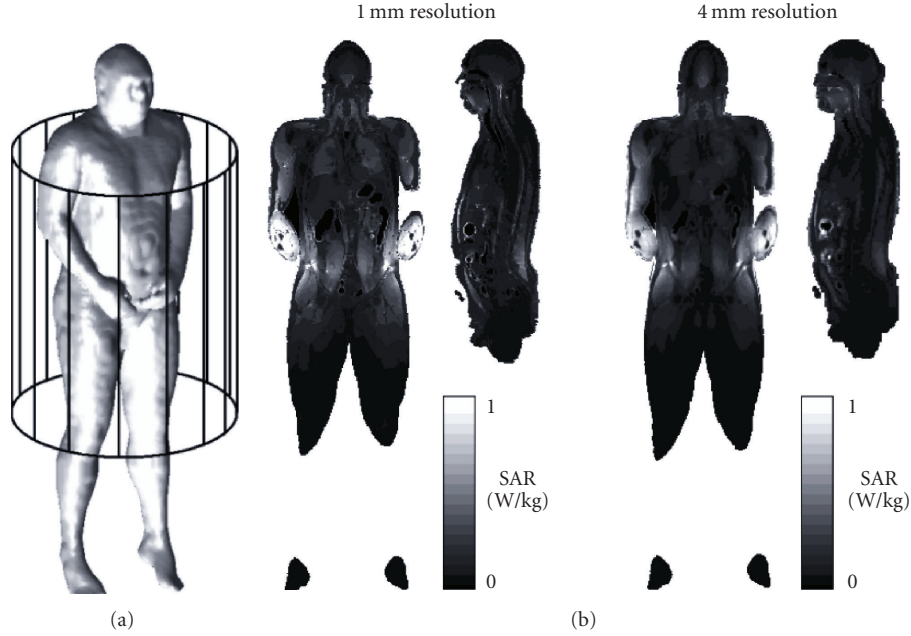


FIGURE 5: (a) Model setup involving the whole-body birdcage resonator and the body model, (b) coronal and sagittal profiles of in situ SAR spatial distributions in the male Brooks Airforce model (BROOK) at 1 mm and 4 mm voxel resolution.

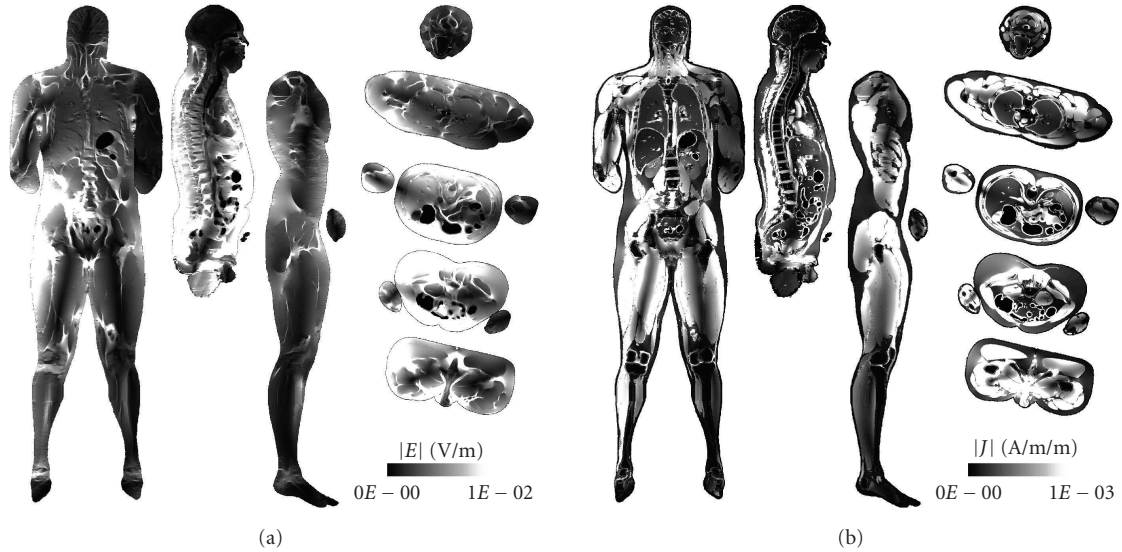


FIGURE 6: Coronal, sagittal and axial distributions of (a) electric field and (b) current density induced in the 1mm-resolution male body model during gradient pulsing. Figure 5(a) illustrates the body posture of the model relative to the gradient set.

TABLE 2: Computing performance.

Property of coefficient matrix A	Problem resolution			
	8 mm	6 mm	4 mm	2 mm
Scale ($n \times n$)	153699×153699	350786×350786	1134416×1134416	8670828×8670828
Nonzero elements	884439	2109038	7150900	57488850
Convergence performance				
Parallelized SOR	2.5 minutes	14 minutes	36 minutes	31 hours
Single-CPU BiCG	10 seconds	39 seconds	3 minutes	1.8 hours
Parallelized BiCG	7 seconds	23 seconds	1.5 minutes	50 minutes

parallel QSGD computing platform over its conventional single processor-based counterpart. Figures 6(a) and 6(b) illustrate very fine details of induced electric field and current density distributions for the male body model, respectively. According to the simulation results, the largest electric fields and current densities are located in the frontal left region of the body, as this is the part of the body that is closest to the gradient coil conductors. With well-conditioned band diagonal sparse coefficient matrices, the proposed parallel QSGD-BiCG scheme demonstrates robust performance in the handling of low-frequency electromagnetic fields problems. The BiCG method also shows efficient memory usage, as it only consumes about 1/3 of memory compared to the standard SOR scheme.

This level of high-resolution analyses is imperative and significant for those interested in a variety of numerical problems such as but not limited to: thermodynamic modeling involving a fine vascular structure, cardiac electric field propagation, hyperthermia, eddy current modeling, occupational exposure of workers to electromagnetic fields, and so forth. Most of these and other related problems would benefit from employing the whole body in the computational process, as this represents a more realistic physical scenario.

4. CONCLUSION

Computationally intensive numerical software has become necessary to handle the increasing complexity of electromagnetic field problems in MRI, particularly at high-field strengths. In this work, high-performance finite-difference solvers architected within a parallel framework have been presented. The potential of the optimized parallel scheme has been demonstrated in typical MRI applications. The case studies indicate that the power of the software can enable straightforward adaptation to applications involving optimization of system components.

ACKNOWLEDGMENTS

The financial support for this project from the Australian Research Council and The Health and Safety Executive (UK) (the project managed by MCL, UK) is gratefully acknowledged.

REFERENCES

- [1] A. K. Andriola Silva, É. L. Silva, E. S. T. Egito, and A. S. Carriço, "Safety concerns related to magnetic field exposure," *Radiation and Environmental Biophysics*, vol. 45, no. 4, pp. 245–252, 2006.
- [2] J. F. Schenck, "Safety of strong, static magnetic fields," *Journal of Magnetic Resonance Imaging*, vol. 12, no. 1, pp. 2–19, 2000.
- [3] P. A. Gowland, "Present and future magnetic resonance sources of exposure to static fields," *Progress in Biophysics and Molecular Biology*, vol. 87, no. 2–3, pp. 175–183, 2005.
- [4] S. Crozier and F. Liu, "Numerical evaluation of the fields caused by body motion in or near high-field MRI scanners," *Progress in Biophysics and Molecular Biology*, vol. 87, no. 2–3, pp. 267–278, 2005.
- [5] "Assessment of electromagnetic fields around magnetic resonance imaging (MRI) equipment," Tech. Rep. RR570, Health and Safety Executive, London, UK, 2007.
- [6] F. X. Hebrank, "SAFE model—a new method for predicting peripheral nerve stimulation in MRI," in *Proceedings of the 8th Annual Meeting of the International Society for Magnetic Resonance in Medicine (ISMRM '00)*, vol. 8, pp. 2007–2013, Denver, Colo, USA, April 2000.
- [7] D. J. Schaefer, J. D. Bourland, and J. A. Nyenhuis, "Review of patient safety in time-varying gradient fields," *Journal of Magnetic Resonance Imaging*, vol. 12, no. 1, pp. 20–29, 2000.
- [8] S. C. Faber, A. Hoffmann, C. Ruedig, and M. Reiser, "MRI-induced stimulation of peripheral nerves: dependency of stimulation threshold on patient positioning," *Magnetic Resonance Imaging*, vol. 21, no. 7, pp. 715–724, 2003.
- [9] J. D. Bourland, J. A. Nyenhuis, and D. J. Schaefer, "Physiologic effects of intense MR imaging gradient fields," *Neuroimaging Clinics of North America*, vol. 9, no. 2, pp. 363–377, 1999.
- [10] C. M. Collins, S. Li, and M. B. Smith, "SAR and B₁ field distributions in a heterogeneous human head model within a birdcage coil," *Magnetic Resonance in Medicine*, vol. 40, no. 6, pp. 847–856, 1998.
- [11] T. S. Ibrahim, R. Lee, B. A. Baertlein, Y. Yu, and P.-M. L. Robitaille, "Computational analysis of the high pass birdcage resonator: finite difference time domain solutions for high-field MRI," *Magnetic Resonance Imaging*, vol. 18, no. 7, pp. 835–856, 2000.
- [12] A. Trakic, F. Liu, H. Sanchez Lopez, H. Wang, and S. Crozier, "Longitudinal gradient coil optimization in the presence of transient eddy currents," *Magnetic Resonance in Medicine*, vol. 57, no. 6, pp. 1119–1130, 2007.
- [13] A. Taflové, *Computational Electrodynamics: The Finite-Difference Time-Domain Method*, Artech House, Boston, Mass, USA, 1995.
- [14] F. Liu, H. W. Zhao, and S. Crozier, "On the induced electric field gradients in the human body for magnetic stimulation by gradient coils in MRI," *IEEE Transactions on Biomedical Engineering*, vol. 50, no. 7, pp. 804–815, 2003.
- [15] S. Crozier and F. Liu, "Numerical evaluation of the fields caused by body motion in or near high-field MRI scanners," *Progress in Biophysics and Molecular Biology*, vol. 87, no. 2–3, pp. 267–278, 2005.
- [16] F. Liu, H. Zhao, and S. Crozier, "Calculation of electric fields induced by body and head motion in high-field MRI," *Journal of Magnetic Resonance*, vol. 161, no. 1, pp. 99–107, 2003.
- [17] F. Liu, S. Crozier, H. Zhao, and B. Lawrence, "Finite-difference time-domain-based studies of MRI pulsed field gradient-induced eddy currents inside the human body," *Concepts in Magnetic Resonance Part B*, vol. 15, no. 1, pp. 26–36, 2002.
- [18] H. Zhao, S. Crozier, and F. Liu, "Finite difference time domain (FDTD) method for modeling the effect of switched gradients on the human body in MRI," *Magnetic Resonance in Medicine*, vol. 48, no. 6, pp. 1037–1042, 2002.
- [19] H. Zhao, S. Crozier, and F. Liu, "A high definition, finite difference time domain method," *Applied Mathematical Modelling*, vol. 27, no. 5, pp. 409–419, 2003.
- [20] F. Liu and S. Crozier, "A distributed equivalent magnetic current based FDTD method for the calculation of E-fields induced by gradient coils," *Journal of Magnetic Resonance*, vol. 169, no. 2, pp. 323–327, 2004.
- [21] Q. Wei, F. Liu, L. Xia, and S. Crozier, "An object-oriented designed finite-difference time-domain simulator for

- electromagnetic analysis and design in MRI-applications to high field analyses,” *Journal of Magnetic Resonance*, vol. 172, no. 2, pp. 222–230, 2005.
- [22] F. Liu and S. Crozier, “An FDTD model for calculation of gradient-induced eddy currents in MRI system,” *IEEE Transactions on Applied Superconductivity*, vol. 14, no. 3, pp. 1883–1889, 2004.
- [23] A. Trakic, H. Wang, F. Liu, H. S. López, and S. Crozier, “Analysis of transient eddy currents in MRI using a cylindrical FDTD method,” *IEEE Transactions on Applied Superconductivity*, vol. 16, no. 3, pp. 1924–1936, 2006.
- [24] F. Liu, B. L. Beck, B. Xu, J. R. Fitzsimmons, S. J. Blackband, and S. Crozier, “Numerical modeling of 11.1T MRI of a human head using a MoM/FDTD method,” *Concepts in Magnetic Resonance Part B*, vol. 24, no. 1, pp. 28–38, 2005.
- [25] C. Guiffaut and K. Mahdjoubi, “A parallel FDTD algorithm using the MPI library,” *IEEE Antennas and Propagation Magazine*, vol. 43, no. 2, pp. 94–103, 2001.
- [26] S. D. Gedney, “Finite-difference time-domain analysis of microwave circuit devices on high performance vector/parallel computers,” *IEEE Transactions on Microwave Theory and Techniques*, vol. 43, no. 10, pp. 2510–2514, 1995.
- [27] K. Taguchi, M. Uchiya, T. Kashiwa, K. Hirayama, H. Kuribayashi, and S. Komatsu, “FDTD large-scale parallel supercomputing and its application to the analysis of radiation characteristics of an antenna mounted on a vehicle,” *International Journal of RF and Microwave Computer-Aided Engineering*, vol. 14, no. 3, pp. 253–261, 2004.
- [28] K. S. Yee, “Numerical solution of initial boundary value problems involving Maxwell’s equations in isotropic media,” *IEEE Transactions on Antennas and Propagation*, vol. 14, no. 5, pp. 302–307, 1996.
- [29] W. H. Press, S. A. Teukolsky, W. T. Vetterling, and B. P. Flannery, *Numerical Recipes in C: The Art of Scientific Computing*, Cambridge University Press, Cambridge, UK, 1992.
- [30] PCGPAK User’s Guide, Scientific Computing Associates, New Haven, Conn, USA.
- [31] F. Liu and S. Crozier, “Electromagnetic fields inside a lossy, multilayered spherical head phantom excited by MRI coils: models and methods,” *Physics in Medicine and Biology*, vol. 49, no. 10, pp. 1835–1851, 2004.
- [32] Human male voxel phantom BROOK, “Brooks Air force Database,” 2004, <http://www.brooks.af.mil/>.
- [33] P. Dimbylow, “Development of the female voxel phantom, NAOMI, and its application to calculations of induced current densities and electric fields from applied low frequency magnetic and electric fields,” *Physics in Medicine and Biology*, vol. 50, no. 6, pp. 1047–1070, 2005.
- [34] C. Gabriel, S. Gabriel, and E. Corthout, “The dielectric properties of biological tissues—I: literature survey,” *Physics in Medicine and Biology*, vol. 41, no. 11, pp. 2231–2249, 1996.
- [35] S. Crozier, L. K. Forbes, and D. M. Doddrell, “The design of transverse gradient coils of restricted length by simulated annealing,” *Journal of Magnetic Resonance A*, vol. 107, no. 1, pp. 126–128, 1994.

Research Article

Assessment of a PML Boundary Condition for Simulating an MRI Radio Frequency Coil

Yunsuo Duan,¹ Tamer S. Ibrahim,^{2,3} Bradley S. Peterson,¹ Feng Liu,¹ and Alayar Kangarlu¹

¹ Columbia University and New York State Psychiatric Institute, New York, NY 10032, USA

² University of Pittsburgh, Pittsburgh, PA 15260, USA

³ University of Oklahoma, Norman, OK 73019-0390, USA

Correspondence should be addressed to Alayar Kangarlu, ak2334@columbia.edu

Received 16 October 2007; Revised 9 April 2008; Accepted 5 June 2008

Recommended by Stuart Crozier

Computational methods such as the finite difference time domain (FDTD) play an important role in simulating radiofrequency (RF) coils used in magnetic resonance imaging (MRI). The choice of absorbing boundary conditions affects the final outcome of such studies. We have used FDTD to assess the Berenger's perfectly matched layer (PML) as an absorbing boundary condition for computation of the resonance patterns and electromagnetic fields of RF coils. We first experimentally constructed a high-pass birdcage head coil, measured its resonance pattern, and used it to acquire proton (¹H) phantom MRI images. We then computed the resonance pattern and B₁ field of the coil using FDTD with a PML as an absorbing boundary condition. We assessed the accuracy and efficiency of PML by adjusting the parameters of the PML and comparing the calculated results with measured ones. The optimal PML parameters that produce accurate (comparable to the experimental findings) FDTD calculations are then provided for the birdcage head coil operating at 127.72 MHz, the Larmor frequency of ¹H at 3 Tesla (T).

Copyright © 2008 Yunsuo Duan et al. This is an open access article distributed under the Creative Commons Attribution License, which permits unrestricted use, distribution, and reproduction in any medium, provided the original work is properly cited.

1. INTRODUCTION

The dimensions and resolutions of a discretized domain for calculating electromagnetic fields can be restrained by the memory and computational capacity of the computer. As a result, the computational domain must utilize efficient and accurate boundary conditions in order to truncate outward waves and therefore simulate infinite radiation boundary conditions of the computational domain. One of the most useable and efficient absorbing boundary conditions that have been reported for the finite difference time domain (FDTD) [1] is the perfect matched layer (PML) [2].

Since its introduction to FDTD, PML has been extended by a number of researchers. Among these PMLs, Berenger's PML [2, 3], anisotropic PML (APML) [4, 5], complex frequency shifted PML (CFS PML) [6], and higher-order PML [7, 8] represent the most usual types of PML. The significant distinction between Berenger's PML and APML, which together are designated regular PML, is that the former uses Maxwellian isotropic absorbing materials and splits each component of electromagnetic fields into two

components, whereas the latter uses anisotropic absorbing materials and keeps the components of electromagnetic fields unsplit. Thus, the implementation of Berenger's PML requires more computer RAM than does APML. CFS PML is more efficient in annihilating the evanescent waves than are the regular PMLs [9], although it sacrifices good absorption of the propagation waves at low frequencies [7]. Higher-order PML is a new attempt to combine the advantages of both regular PML and CFS PML [7, 8].

PMLs have been widely used with FDTD to compute electromagnetic fields, including those of magnetic resonance imaging (MRI) [10–13]. Thus far, however, the assessment of the accuracy and efficiency of PML when applied to MRI radiofrequency (RF) simulations has not been reported. In fact, the required grid sizes conflict with the required resolutions of the calculated frequency when using FDTD to compute the resonance pattern and electromagnetic fields of RF coils. On the one hand, the small dimensions of copper strips (~30 μm thick) used to construct RF coils require small grids matched to the thickness of the copper strips so as to improve the accuracy of the simulations. On the other hand,

the frequency resolution of the calculated resonance patterns and the requisite computing time are inversely proportional to the size of the grids. Thus, the grid sizes should be sufficiently large to improve the frequency resolution of the calculated resonance pattern of the coil and to reduce computing time. Moreover, because the dimensions of PML together with the coil geometry are enormous relative to the size of the copper strips, a vast number of Yee cells are needed to simulate the coil fully. Satisfying these conflicting requirements requires both a vast computer RAM and an enormous number of iterated time steps, which produces an unacceptable accumulation of numerical phase errors as well as an unrealistic computational time. A PC with 3.39 GHz dual processors and 2 GB RAM, for example, requires about 116 hours to compute the resonance pattern of an adult RF head coil using FDTD with a grid size of $2 \times 2 \times 2 \text{ mm}^3$ and frequency resolution of 0.5 MHz. If the calculated resonance pattern does not match the desired one (the coil is off tuned), this computation must be repeated using modified coil parameters until the desired resonance pattern is achieved.

Furthermore, the increasing strength of the static magnetic fields (B_0) in MRI applications has reduced the RF wavelength inside human tissue close to or below the dimensions of the subject to be scanned. For example, at 3 Tesla (T), the wavelength of an RF field inside the human head is about 280 mm, which is close to the average diameter of an adult RF head coil. Therefore, the geometric structure of RF coils and the sizes of the biological load (head or body) are no longer negligible in relation to the wavelength of the operational frequency when B_0 is 3 T or higher. Thus, conventional lumped-element methods such as transmission line and circuit theories become inadequate for analyzing and designing RF coils. As an alternative, the FDTD method, a full-wave numerical technique that is capable of accounting for the geometry of a coil as well as the intricacies of the sample, has emerged as the tool of choice for analyzing RF coils at high fields [10–13]. Consequently, the need for a good computationally efficient boundary condition has become more pressing.

We present a systematic evaluation of the effect of the parameters of Berenger's PML on the accuracy and efficiency of the calculated resonance pattern and the electromagnetic fields of RF coils. Because the Larmor frequency of ^1H at 3 T (127.72 MHz) is much lower than the frequencies at which the CFS PML works well, we have omitted the use of CFS PML for simulation of RF coils. Furthermore, because the additional RAM required for Berenger's PML compared to APML is not an excessive burden for modern computers, and because implementation of Berenger's PML is easier than that of APML, we selected Berenger's PML as the absorbing boundary condition for assessment of simulated RF coils. This choice does not limit the generality of our assessments for other PMLs, because the influence trends of the parameters of other PMLs are similar to those of Berenger's [9].

We first constructed an actual high-pass birdcage head coil [14], measured its resonance pattern, and acquired proton images from a phantom. We then computationally modeled the resonance pattern and B_1 fields of the coil

(i.e., the circularly polarized component of the transverse magnetic field that is responsible for excitation) using an FDTD code developed in-house that uses Berenger's PML as an absorbing boundary condition. To assess the accuracy and efficiency of PML for this purpose, we investigated the criteria for optimizing PML parameters by comparing the numerically calculated results with the experimentally measured ones until the best agreement between them was achieved. Thus, we identified the optimal PML parameters that achieved both high accuracy and at least moderate computational efficiency for analyzing the essential performance characteristics of RF coils.

2. MATERIAL AND METHODS

Our method for assessing PML differed from the approaches used in the design of RF coils. Typically, those approaches first evaluate the B_1 field of a modeled coil and then optimize it by changing the geometry and lumped components of the coil's design before constructing it. Here, our goal was not to design a coil, but to assess the performance of the PML in accurately and efficiently simulating an RF coil. Therefore, we first designed, constructed, and tuned a birdcage head coil to the proper operational mode. We measured the coil's resonance pattern and used it to acquire ^1H images of a phantom in a 3 T MRI scanner. Next, this actual coil was modeled using an FDTD scheme that used PML as an absorbing boundary condition. We calculated the resonance pattern and B_1 field of the coil. We compared the calculated and measured results to adjust the parameters of the PML and to assess the accuracy of the PML according to the criteria defined in the following sections. We further assessed computational efficiency of the PML by comparing the computational demands for each set of PML parameters, while assuming that greater efficiency was associated with less computational time.

2.1. Experimental measurements

Our experimental head coil was constructed based on the high-pass birdcage design [14] for a typical adult head. The coil had 16 rungs connected by 2 end-rings, 32 capacitors of 13.6 pF, a diameter of 292 mm, and a length of 356 mm. The rungs and rings were made of copper strips having a width of 8 mm and a thickness of 30 μm (see Figure 1).

We obtained the resonance pattern of the coil by measuring the S-parameters using an Agilent 4395A network/spectrum/impedance analyzer. The coil worked in quadrature mode [14] with a 90° hybrid coupler connected between the analyzer and the coil's excitation ports. We acquired ^1H images from a phantom loaded in the coil using a GE 3 T Signa scanner and a gradient echo pulse sequence having a 90° flip angle, 500 milliseconds repetition time (RT), and 10 milliseconds echo time (ET).

The phantom consisted of a spherical plastic container filled with purified water and NaCl in order to approximately simulate the average dielectric constant ($70\epsilon_0$) and conductivity (0.57 S/m) of the human brain at 128 MHz [9, 15]. The corresponding wavelength inside the phantom was 280 mm,

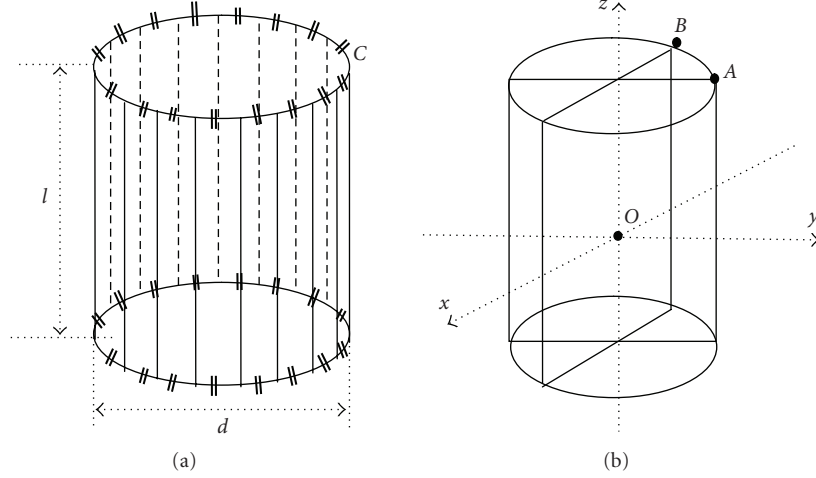


FIGURE 1: (a) Structure of a high-pass birdcage head coil showing a schematic view of the coil and (b) coronal and sagittal planes of the coil, where “ l ”: length of the coil; “ d ”: diameter of the coil; “ C ”: capacitor; “ A ” and “ B ”: RF feeding points; “ O ”: center of the coil.

which was 95.6% of the diameter and 78.6% of the length of the actual coil.

2.2. Computational model

In simulating the RF coil, we first used FDTD with Berenger’s PML as the boundary condition to model the actual coil loaded with the phantom. We then computed the resonance pattern and B_1 field of the actual coil using the modeled coil. We finally evaluated performance of the PML by comparing the calculated results with the experimental ones. Our FDTD model and computing procedures are described below.

2.2.1. FDTD model

Our computer code for FDTD was developed in-house. The FDTD model had 3D grids of 2 mm definition in each of the x -, y -, and z -directions. The z -axis of the simulation was parallel to the longitudinal axis of the coil. Although the actual coil and the phantom were modeled according to their specific physical sizes, some of the modeled dimensions deviated from those of the real coil because the dimensions of some of the real components were smaller than the definition of our grid. For example, the copper strips were represented by one voxel (2 mm) in thickness rather than by their actual thickness of 30 microns. Similarly, the lumped capacitors were represented by one voxel and modeled by the following equation [16]:

$$I_x^{n+1/2} = C\Delta x \frac{E_{x_{i,j,k}}^{n+1} - E_{x_{i,j,k}}^{n-1}}{2\Delta t}, \quad (1)$$

where I_x was the current flowing through the capacitor, C was the capacitance of the capacitor, and x was the direction along which the capacitor aligned. Note that “ x ” was substituted with “ y ” or “ z ” when the capacitor aligned along the respective directions.

For stable time marching, the time step length, Δt must satisfy the Courant-Friedrichs-Lewy (CFL) stability criterion [1]:

$$\Delta t < \frac{c_{\max}}{\sqrt{1/\Delta x^2 + 1/\Delta y^2 + 1/\Delta z^2}}, \quad (2)$$

where c_{\max} is the maximum propagation velocity of the electromagnetic waves within the simulated region. In this case, $\Delta x = \Delta y = \Delta z = 2$ mm, and c_{\max} was the velocity of light. The corresponding maximum Δt was 3.789 picoseconds. According to the Nyquist criterion for sampling, the associated frequency resolution (Δf) was given as

$$\Delta f = \frac{1}{(N\Delta t)}, \quad (3)$$

where N was the number of time steps (iterations). For a frequency resolution of 1 MHz or less, N should be greater than 263922. We selected N as 262144 ($= 2^{18}$) for convenience of calculating the fast Fourier transformation (FFT).

2.2.2. Computation of resonance pattern

We computed the resonance pattern of the coil by applying the FFT to its calculated magnetic field. In so doing, we first excited the coil with an excitation signal that contained a sufficient number of frequencies such that the calculated electromagnetic fields of the coil contained all frequencies within its bandwidth. Typically, the resonance frequency of the highest mode of the birdcage coil for ^1H at 3 T is < 500 MHz. We, therefore, chose a Gaussian function as the excitation signal having a -3 dB frequency of 500 MHz:

$$s(t) = e^{-(t/2T_0-3)^2}, \quad (4)$$

where $T_0 = 1/\omega_{-3\text{dB}} = 1/(10^9\pi)$.

We then applied this excitation signal to a capacitor of the coil and iteratively computed the electromagnetic field of the coil. We saved the calculated B_1 field for every time step at sampling points on the surface and at the center of the coil (see Figure 1(b)). We then applied FFT to the saved B_1 field to obtain the frequency spectra (i.e., the resonance pattern) of the coil at the related sampling points.

A correctly calculated resonance pattern should agree with the real coil's actual resonance pattern provided that the frequency deviations between the calculated and measured patterns are below the resolution of the calculated resonance pattern and therefore are considered negligible. Otherwise, we must adjust the parameters of the PML or the parameters of the modeled coil and recompute the resonance pattern.

2.2.3. Computation of the B_1 field

After calculating the coil's resonance pattern, we then computed the B_1 field of the coil at the Larmor frequency of ^1H at 3 T. To achieve quadrature excitation, we, respectively, applied two sine waves centered at the Larmor frequency to feed two capacitors 90° azimuthally apart from each other (points A and B in Figure 1(b)). The two sine wave excitations having a 90° difference in their phases were presented as

$$s_1(t) = (1 - e^{-(\omega_0 t/5)^2}) \sin(2\pi f_0 t), \quad (5a)$$

$$s_2(t) = (1 - e^{-(\omega_0 t/5)^2}) \sin(2\pi f_0 t - \pi/2), \quad (5b)$$

where f_0 is the Larmor frequency (127.72 MHz for ^1H at 3 T). The introduction of the coefficient $(1 - e^{-(\omega_0 t/5)^2})$ in the excitation signal accelerated stabilization of the calculated B_1 field [10].

2.3. PML

2.3.1. PML parameters

When implementing Berenger's PML [2, 3], layers of artificial perfect electric conductor (PEC) were introduced at the boundaries of the computational domain to absorb the waves traveling outwards (i.e., to satisfy the radiation condition). The conductivity of each layer increased gradually from inside (near the coil's geometry) to outside (away from the coil's geometry). Thus, the outgoing waves attenuated to negligible levels as they traveled through the PML, then reflected at the PEC walls located at the outer boundaries of the computational domain, and then traveled through the PML back to the geometry of the coil.

To compute the fields in the presence of Berenger's PML, each component of the electromagnetic fields must be divided into two subcomponents. For example, the electric field component E_x was divided into E_{xy} and E_{xz} :

$$E_x = E_{xy} + E_{xz}, \quad (6)$$

where

$$\begin{aligned} E_{xy}^{n+1}\left(i + \frac{1}{2}, j, k\right) &= e^{-(\sigma_y/\epsilon_0)\Delta t} E_{xy}^n\left(i + \frac{1}{2}, j, k\right) + \frac{1}{\sigma_y \Delta y} \left(1 - e^{-(\sigma_y/\epsilon_0)\Delta t}\right) \\ &\times \left\{ \left[H_{zx}^{n+1/2}\left(i + \frac{1}{2}, j + \frac{1}{2}, k\right) - H_{zx}^{n+1/2}\left(i + \frac{1}{2}, j - \frac{1}{2}, k\right) \right] \right. \\ &\quad \left. - \left[H_{zy}^{n+1/2}\left(i + \frac{1}{2}, j, k + \frac{1}{2}\right) - H_{zy}^{n+1/2}\left(i + \frac{1}{2}, j, k - \frac{1}{2}\right) \right] \right\}, \end{aligned} \quad (7a)$$

$$\begin{aligned} E_{xz}^{n+1}\left(i + \frac{1}{2}, j, k\right) &= e^{-(\sigma_z/\epsilon_0)\Delta t} E_{xz}^n\left(i + \frac{1}{2}, j, k\right) + \frac{1}{\sigma_z \Delta z} \left(1 - e^{-(\sigma_z/\epsilon_0)\Delta t}\right) \\ &\times \left\{ \left[H_{yx}^{n+1/2}\left(i + \frac{1}{2}, j + \frac{1}{2}, k\right) - H_{yx}^{n+1/2}\left(i + \frac{1}{2}, j - \frac{1}{2}, k\right) \right] \right. \\ &\quad \left. - \left[H_{yz}^{n+1/2}\left(i + \frac{1}{2}, j, k + \frac{1}{2}\right) - H_{yz}^{n+1/2}\left(i + \frac{1}{2}, j, k - \frac{1}{2}\right) \right] \right\}. \end{aligned} \quad (7b)$$

Similarly, the magnetic field component H_x was divided into H_{xy} and H_{xz} :

$$H_x = H_{xy} + H_{xz}, \quad (8)$$

where

$$\begin{aligned} H_{xy}^{n+1/2}\left(i, j + \frac{1}{2}, k + \frac{1}{2}\right) &= e^{-(\sigma_y^*/\mu_0)\Delta t} H_{xy}^{n-1/2}\left(i, j + \frac{1}{2}, k + \frac{1}{2}\right) + \frac{1}{\sigma_y^* \Delta y} \left(1 - e^{-(\sigma_y^*/\mu_0)\Delta t}\right) \\ &\times \left\{ \left[E_{zx}^n\left(i, j + 1, k + \frac{1}{2}\right) - E_{zx}^n\left(i, j, k + \frac{1}{2}\right) \right] \right. \\ &\quad \left. - \left[E_{zy}^n\left(i, j + 1, k + \frac{1}{2}\right) - E_{zy}^n\left(i, j, k + \frac{1}{2}\right) \right] \right\}, \end{aligned} \quad (9a)$$

$$\begin{aligned} H_{xz}^{n+1/2}\left(i, j + \frac{1}{2}, k + \frac{1}{2}\right) &= e^{-(\sigma_y^*/\mu_0)\Delta t} H_{xz}^{n-1/2}\left(i, j + \frac{1}{2}, k + \frac{1}{2}\right) + \frac{1}{\sigma_y^* \Delta z} \left(1 - e^{-(\sigma_y^*/\mu_0)\Delta t}\right) \\ &\times \left\{ \left[E_{yx}^n\left(i, j + 1, k + \frac{1}{2}\right) - E_{yx}^n\left(i, j, k + \frac{1}{2}\right) \right] \right. \\ &\quad \left. - \left[E_{yz}^n\left(i, j + 1, k + \frac{1}{2}\right) - E_{yz}^n\left(i, j, k + \frac{1}{2}\right) \right] \right\}. \end{aligned} \quad (9b)$$

The reflection of the electromagnetic wave by the PML depended on the conductivity of each PML layer, the number of PML layers, and the angle of incidence (with respect to the PML interface) of the incident wave. Thus, to apply a specific PML algorithm into FDTD computations, the electric conductivity of each layer, σ_i , the fictitious magnetic

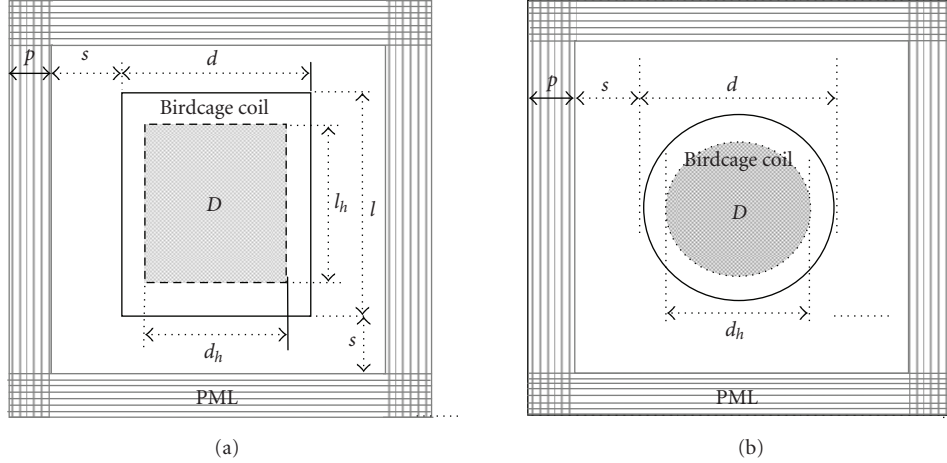


FIGURE 2: The schematic view of the computational domain. (a) Longitudinal plane (xoz -plane in Figure 1(b)). (b) Transverse plane (xoy -plane in Figure 1(b)). “ D ” homogenous region of B_1 -field (shaded); “ p ”: the thickness of the PML; “ s ”: the distance from PML to the closest point on the coil geometry; “ d ”: the diameter of the coil; “ l ”: the length of the coil; “ d_h ”: the diameter of region D ; “ l_h ”: the length of region D . The dark solid rectangle and circle denote the outline of the coil in the longitudinal plane and transverse plane, respectively.

conductivity of each layer, σ_i^* , and the number of layers, N_{PML} , must be determined before the computations. Usually, given a required reflection coefficient at the outer layer with normal incidence (0° incidence angle), $R(0)$, σ_i , and σ_i^* are obtained by [2, 3]

$$\begin{aligned}\sigma_i &= \left(\frac{p_i}{p}\right)^m \sigma_{\max}, \\ \sigma_i^* &= \left(\frac{p_i}{p}\right)^m \sigma_{\max}^*,\end{aligned}\quad (10)$$

where p is the thickness of the PML, p_i is the distance from the inner side (towards the coil) of the boundary to i th layer of PML, m is a coefficient in the range of 1 to 5, σ_{\max} and σ_{\max}^* are the electric conductivity and magnetic conductivity of the outer layer of PML respectively, which are given by

$$\begin{aligned}\sigma_{\max} &= \frac{(m+1)\epsilon_0 c_0}{2p} \ln\left(\frac{1}{R(0)}\right), \\ \sigma_{\max}^* &= \frac{\epsilon_0}{\mu_0} \sigma_{\max},\end{aligned}\quad (11)$$

where ϵ_0 and μ_0 are the permittivity and permeability in free space, respectively.

According to Berenger [2, 3], an $m = 2$ and an $R(0) = 10^{-4}$ are optimal for computations using the PML algorithm. We therefore used these values for our calculations. Generally, the reflection at the PML interface increased with the incident angle (i.e., with deviation away from a normal incidence). The PML was designed to absorb (with infinitesimal spatial and temporal steps) nearly all of the electromagnetic waves having a normal incidence (0°). However, the angle of incidence on the PML interface for RF coil calculations is difficult to define, as radiations and reflections from the coil or load occur at all possible angles. For practical purposes, we assumed that the incident angle was a function of the thickness of the PML, “ p ,”

and the distance from the coil structure to the PML, “ s ” (see Figure 2). We therefore use “ p ” and “ s ” to assess the reflection of the PML. For quantitative measurements, we used “ N_p ,” the layers of the PML, to denote the thickness of the PML, “ p .” Each layer was modeled by one grid. The distance “ s ” was also measured in grids “ N_s .”

Usually, the B_1 field of a well-tuned empty birdcage coil is homogenous within a cylindrical region located in the center of the coil. This cylindrical region, denoted by “ D ,” together with the diameter “ d_h ” and the length “ l_h ,” is illustrated in Figure 2.

2.3.2. PML assessment criteria

While varying the parameters of the PML, we evaluated its cumulative error by comparing the measured and calculated B_1 field in their resonance patterns, homogeneity, and stability. We deem a PML satisfactory if the results of calculation met all of the following criteria.

1. Resonance pattern

For the comparison of resonance patterns, the number of calculated modes should be equal to the number of measured modes, and the maximum difference of the frequencies at each mode should be less than the frequency resolution of the calculated resonance pattern (here, 0.5 MHz). That is

$$N_c = N_m, \quad (\text{C1.a})$$

$$df_{i\max} = (f_{ci} - f_{mi})_{\max} < 0.5 \text{ MHz}, \quad \{i = 0, 1, \dots, N_m\}, \quad (\text{C1.b})$$

where

N_c is the number of the calculated modes;

N_m is the number of the measured modes;

df_i is the difference between the calculated and measured frequency at i th mode;

f_{ci} is the calculated resonance frequency at i th mode;
 f_{mi} is the measured resonance frequency at i th mode.

2. B_1 field homogeneity

We identified a region as homogenous region if the maximum relative deviation of the B_1 field there was $<10\%$. This criterion, when applied to the birdcage coil, yielded

$$D_{r\max} = \frac{(B_{1c} - \overline{B_{1c}})_{\max}}{\overline{B_{1c}}} < 10\%, \quad \{B_{1c} \in D\}, \quad (C2)$$

where

$D_{r\max}$ is the maximum relative deviation;
 B_{1c} is the calculated B_1 field;
 $\overline{B_{1c}}$ is the calculated mean B_1 field;
 D is the cylindrical region (see Figure 2).

3. B_1 field stability

The calculated B_1 field should be stable after implementation of a certain number of time steps. We formulated the following criterion for this requirement:

$$\frac{(B_{1cpj} - B_{1cpk})_{\max}}{B_{1cp}} < 10\%, \quad \{B_{1c} \in D; N_b < j, k < N_t\}, \quad (C3)$$

where

B_{1cpj} and B_{1cpk} are the j th and k th peak value of the calculated B_1 -field, respectively;
 $\overline{B_{1cp}}$ is the mean of the peak value of the calculated B_1 -field;
 N_b is the time steps at which the calculated B_1 -field starts to be stable;
 N_t is the total time steps of calculation.

3. RESULTS AND DISCUSSION

We found that both the resonance pattern and homogeneity of the calculated B_1 -field agreed with the measurements of the real coil when using an optimal PML but not when using nonoptimal PMLs.

3.1. Resonance pattern

The measured resonance pattern had eight distinct resonance modes (see Figure 3(a)). Mode 0 had the highest frequency at 180.2 MHz. Mode 1 (the operational mode, marked as H_1) had a frequency of 127.72 MHz, which is the Larmor frequency of ^1H at 3 T. The other modes had frequencies ranging between 57.8 and 96.4 MHz.

Intuitively, a good PML should be sufficiently thick to attenuate outgoing waves without contaminating the actual electromagnetic fields within the coil. A good PML also should be sufficiently distant from the coil's geometry to yield the smallest possible incidence angles of the outgoing waves at the PML interface. By varying the thickness of the PML, N_p and the distance from the PML to the closest

surface of the coil, N_s , we obtained the calculated resonance pattern in which frequencies agreed with the measured resonance pattern (see Figure 3(c)). Because the resolution of the calculated resonance pattern was 0.5 MHz after 262144 time steps, the frequency of each calculated and measured modes inevitably deviated. However, the maximum deviation between the calculated and measured frequencies did not exceed the resolution of the calculated frequency, indicating that this model provided highly accurate estimates of the measured frequencies.

We found that to obtain the correct resonance pattern for this particular coil, the number of layers of the PML, N_p , must be greater than 8 and the number of grids between the closest point on the coil's geometry and the PML interface, N_s , must be greater than 5. Any PML having an $N_p < 8$ or an $N_s < 5$ produced a resonance at a single frequency (see Figure 3(b)) or a split of the resonance modes (see Figure 3(d)). Based on these results for the computation of the coil's resonance pattern, we advise use of a PML having a thickness of at least 10 layers and a distance of at least 8 grids between the closest point on the coil's geometry and the PML interface. Note that these observations obviously are valid for the particular spatial and temporal steps that we examined. Nonetheless, splitting of the resonance modes of an RF coil in simulations but not in the bench testing could be caused by a poor choice of PML parameters.

3.2. B_1 homogeneity and stability

To evaluate B_1 homogeneity and stability, we first computed the B_1 field of the coil using a PML with higher N_p and N_s values and then we repeated the computations using a PML with lower N_p and N_s values. Comparing the two computed results demonstrated that when the PML with higher N_p and N_s values increased the amplitude of the calculated B_1 -field gradually during the first 40 000 time steps (corresponding to about 40 cycles of the B_1 field at 127.72 MHz) and then stabilized thereafter (see Figure 4(a)). Using the PML with lower N_p and N_s values, however, increased the amplitude of the calculated B_1 -field monotonically and without bound (see Figure 4(b)).

These findings indicate that we obtained an optimal PML by iteratively calculating and evaluating the B_1 field of the coil for either 40 or 120 cycles and by simultaneously varying the thickness of the PML and the distance between the PML interface and the closest point on the coil's geometry. We let N_p equal 5, 8, 10, or 12 while increasing N_s from 1 to 20 for each value of N_p . While performing these numerical studies of the effects of varying N_p and N_s , we calculated the coil's B_1 field and evaluated its homogeneity according to our previously stated criterion C2 and C3 for each PML setting. These assessments revealed that the homogeneity of the calculated B_1 field improved with increases of both N_p and N_s (see Figure 5). We noted that the calculated deviations were especially sensitive to values of N_p and N_s that were below 8 and 5, respectively, for 40-cycle computations, whereas increasing N_p and N_s beyond 8 and 6, respectively, did not noticeably improve homogeneity of the calculated B_1 field (see Figure 5(a)). When using 120 cycles, the minimum

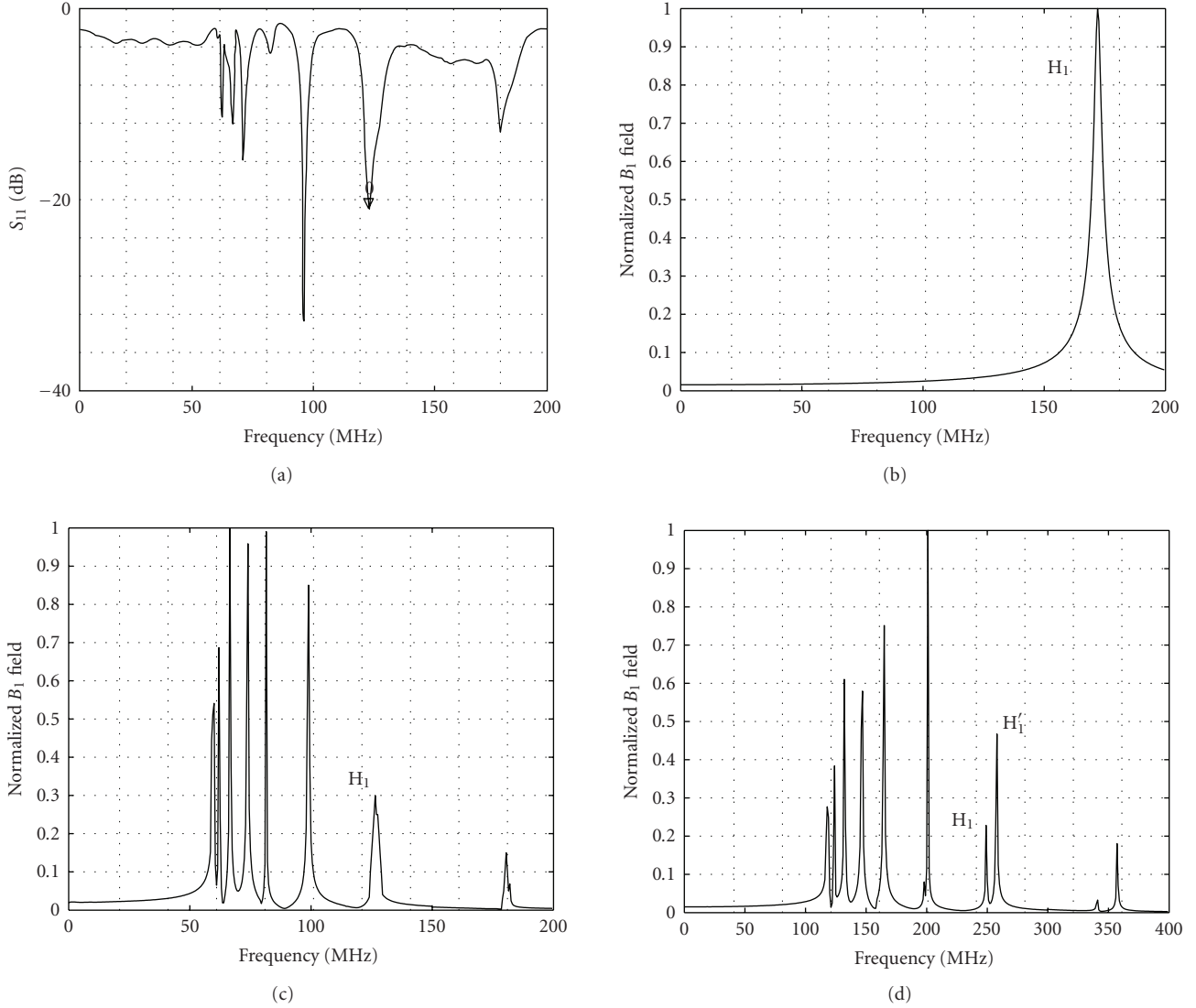


FIGURE 3: (a) Measured S_{11} of the coil (obtained with a network analyzer). H_1 is the mode of interest (mode 1); (b) calculated resonance pattern with $N_p = 5$ and $N_s = 5$ grids. Only one mode resonated at 174 MHz; (c) calculated resonance pattern with $N_p = 10$ and $N_s = 8$ grids. The number of modes and resonance frequencies is in excellent agreement with the measured S_{11} ; (d) calculated resonance pattern with $N_p = 10$ and $N_s = 1$ grids. Mode 0 and mode 1 are split (e.g., mode 1 split into two peaks: H_1 and H_1' .)

optimal N_p and N_s increased to 10 layers and 12 grids (see Figure 5(b)).

Because computational time is proportional to the number of grids, which in turn is directly related to the sum of N_p and N_s to the third power, N_p and N_s should be minimized to reduce the computational time, but only so far as to retain the required degree of computational accuracy. Thus for the calculation of a 40-cycle B_1 field, an optimal PML should be 8 layers thick and at a distance of 5 grids from the closest point on the coil's geometry (see Figure 5(a)). For the calculation of a 120-cycle B_1 field, an optimal PML should be at least 10 layers thick and at a distance of 12 grids from the coil's geometry (see Figure 5(b)).

Additionally, we found that a well-optimized PML yielded a homogeneous calculated B_1 field (see Figure 6(b)) that agreed well with the measured field (see Figure 6(a)). A

poorly optimized PML, however, yielded an inhomogeneous calculated B_1 field both inside and outside the coil (see Figure 6(c)). Furthermore, a PML that satisfied the homogeneity criterion after 40 000 time steps can deteriorate when using a larger number of time steps (see Figure 6(d)), because the reflections on the PML can accumulate to unacceptable levels with the increasing number of iterations.

3.3. Simulation with a heterogeneous phantom

The above findings were based on tests using a homogenous phantom. A human head, however, consists of various tissues, each of which differs in their dielectric and conductivity properties (see Table 1) [10, 13, 15]. To assess the influences of these heterogeneous tissues on the accuracy of the PML, we simulated a realistic human head using a heterogeneous

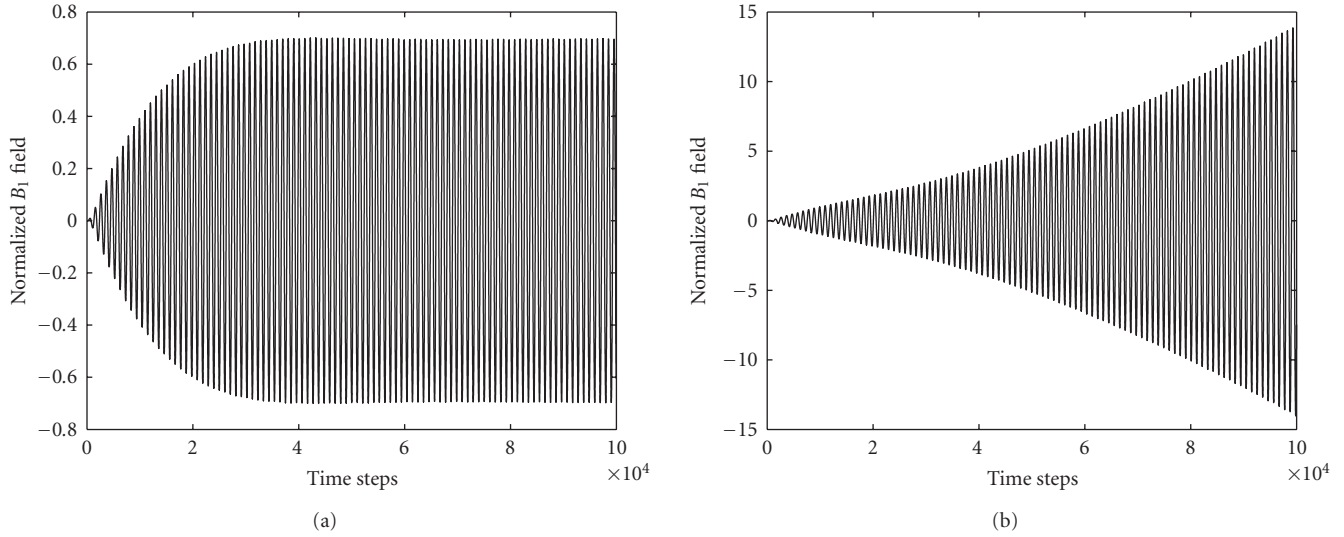


FIGURE 4: Calculated B_1 -field at the center of the coil. (a) PML with $N_p = 10$ and $N_s = 10$. The B_1 -field is stable after 40 000 time steps; (b) PML with $N_p = 5$ and $N_s = 5$. The B_1 -field increases monotonically even after 100 000 time steps.

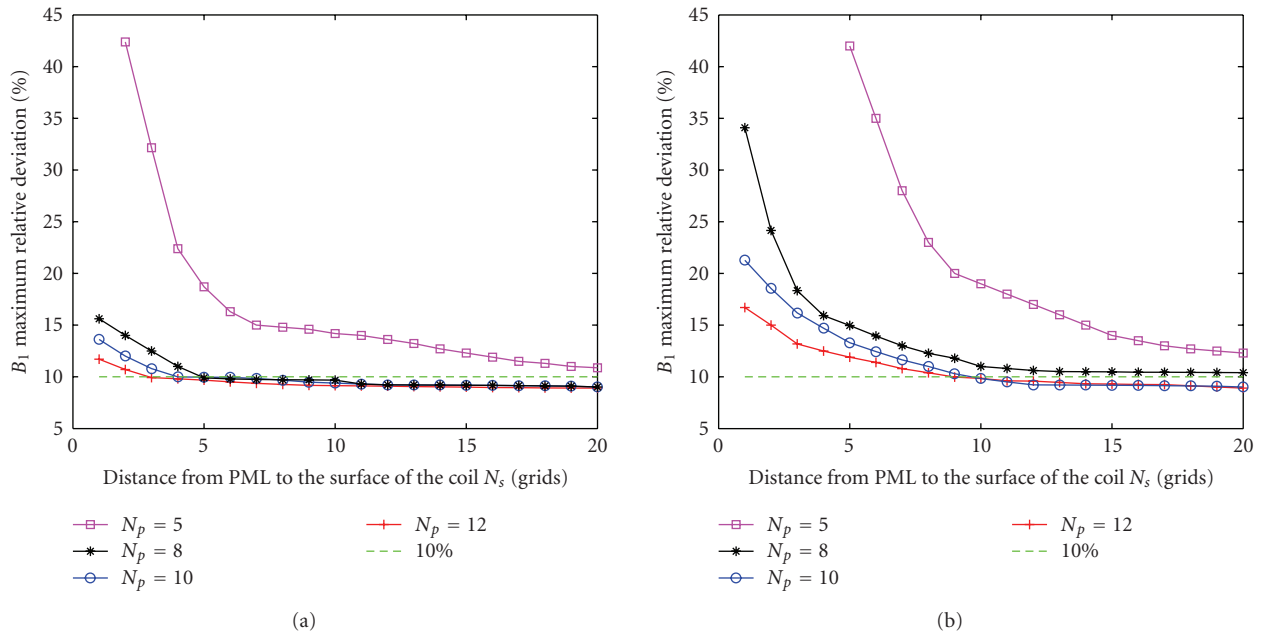


FIGURE 5: Maximum deviations of the calculated B_1 -field within a circular region positioned in axial plane at the center of the coil. This region has a diameter that is 80% of the coil's diameter. The results are presented at 127.72 MHz, the (a) Larmor frequency of ^1H at 3 T after iterations of 40 cycles and (b) after iterations of 120 cycles.

phantom and then computed the resonance pattern and B_1 fields of the coil in which it was placed. The outer layer of grids of the heterogeneous phantom was modeled as skin (2 mm thick), three layers of grids inside the skin layer were modeled as skull (6 mm thick), and another three layers next to skull were modeled as cerebrospinal fluid (CSF). The remaining center portion of the phantom was modeled as brain.

The calculated results showed that when using the same PML parameters, (a) the resonance frequency at each mode of the calculated resonance pattern kept unchanged, even though the calculated Q -factor of the coil loaded with the heterogeneous phantom compared with that of the homogeneous phantom decreased by 4.6% at the operating frequency of 128 MHz; (b) the deviation of the calculated B_1 field of the coil loaded with the heterogeneous phantom

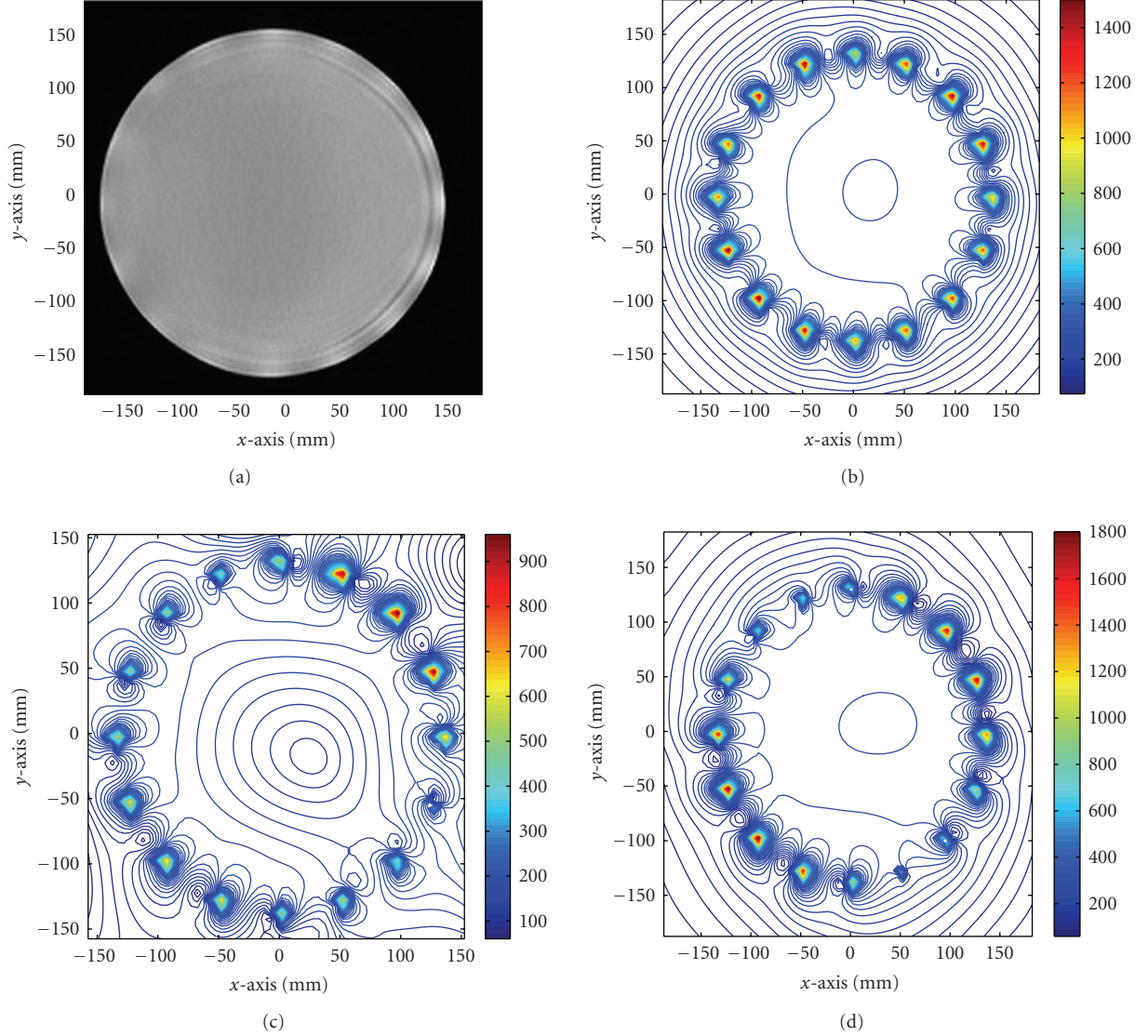


FIGURE 6: Measurement of homogeneity of B_1 field. (a) Acquired MR image of an oil phantom loaded within the coil. (b) Calculated B_1 -map after 40-cycle iterations with $N_p = 10$ and $N_s = 10$. The homogeneity of B_1 -map is good inside, on the surface of, and outside of the coil. (c) Calculated B_1 -map after 40-cycle iterations with $N_p = 10$ and $N_s = 1$. The homogeneity of B_1 -map is unacceptable. (d) Calculated B_1 -map after 120-cycle iterations with $N_p = 10$ and $N_s = 10$. The intensities of the B_1 field at the left-bottom corner and right-top corner are higher than those at other corners.

TABLE 1: The dielectric and conductivity of tissues inside a human head at 128 MHz.

Tissue type	ϵ_r	σ (s/m)
Skin	63	0.86
Skull	25	0.05
CSF	103	0.7
Brain	70	0.57

compared with that loaded with homogeneous phantom increased by 1.4%. These changes in both the Q-factor and deviation of the B_1 field were caused by differences in heterogeneity of the phantom rather than by the PML used in the computations. Thus, we believe that the parameters of

a PML optimized for homogeneous phantoms also apply to heterogeneous phantoms.

4. CONCLUSION

We have explored the role of Berenger's PML as an absorbing boundary condition in the computational characterization of RF coils for MRI at 3 T. We presented a method that evaluates the accuracy and efficiency of the PML for computing the resonance patterns and B_1 fields of RF coils using FDTD. We defined three criteria to evaluate the PML: (1) the deviation of the frequencies of the resonance mode for the calculated and the measured data, (2) the maximum relative deviation of the calculated B_1 field inside the coil, and (3) the numerical

stability of the calculated B_1 field of the coil. The results demonstrated that the accuracy and efficiency of the PML as an absorbing boundary condition closely depend on both the thickness of the PML and the space between the PML and the coil surface. For computation of the coil's resonance patterns, a poor choice of PML parameters can produce either a split in the resonance modes or a resonance that occurs only at a single mode. For the computation of B_1 field, a poor choice of PML parameters can produce a large fluctuation of the B_1 field. Additionally, PML parameters that yield good computational accuracy for a specified number of time steps can also yield inaccurate results with an excessive number of time steps, implying the excess accumulation of reflections of the RF wave on the PML. Taking into account both accuracy and efficiency for specified spatial and temporal steps, we found that an optimal PML for both the computation of the resonance pattern and the 40-cycle B_1 field of a 3 T head coil loaded with a phantom has a thickness of at least 8 layers and a distance of 5 grids from the PML to the closest point on the coil's geometry. Furthermore, the thickness will increase to at least 10 layers and the distance to at least 12 grids for computations of more than 40 cycles of the B_1 fields.

REFERENCES

- [1] K. S. Yee, "Numerical solution of initial boundary value problem involving Maxwell's equations in isotropic media," *IEEE Transaction on Antennas and Propagation*, vol. 14, no. 3, pp. 302–307, 1966.
- [2] J.-P. Berenger, "A perfectly matched layer for the absorption of electromagnetic waves," *Journal of Computational Physics*, vol. 114, no. 2, pp. 185–200, 1994.
- [3] J.-P. Berenger, "Three-dimensional perfectly matched layer for the absorption of electromagnetic waves," *Journal of Computational Physics*, vol. 127, no. 2, pp. 363–379, 1996.
- [4] Z. S. Sacks, D. M. Kingsland, R. Lee, and J.-F. Lee, "A perfectly matched anisotropic absorber for use as an absorbing boundary condition," *IEEE Transactions on Antennas and Propagation*, vol. 43, no. 12, pp. 1460–1463, 1995.
- [5] S. D. Gedney, "An anisotropic perfectly matched layer-absorbing medium for the truncation of FDTD lattices," *IEEE Transactions on Antennas and Propagation*, vol. 44, no. 12, pp. 1630–1639, 1996.
- [6] M. Kuzuoglu and R. Mittra, "Frequency dependence of the constitutive parameters of causal perfectly matched anisotropic absorbers," *IEEE Microwave and Guided Wave Letters*, vol. 6, no. 12, pp. 447–449, 1996.
- [7] D. Correia and J.-M. Jin, "On the development of a higher-order PML," *IEEE Transactions on Antennas and Propagation*, vol. 53, no. 12, pp. 4157–4163, 2005.
- [8] B. Sjögreen and N. A. Peterson, "Perfectly matched layers for Maxwell's equations in second order formulation," *Journal of Computational Physics*, vol. 209, no. 1, pp. 19–46, 2005.
- [9] J.-P. Bérenger, "Numerical reflection from FDTD-PMLS: a comparison of the split PML with the unsplit and CFS PMLS," *IEEE Transactions on Antennas and Propagation*, vol. 50, no. 3, pp. 258–265, 2002.
- [10] J. Chen, Z. Feng, and J.-M. Jin, "Numerical simulation of SAR and B_1 -field inhomogeneity of shielded RF coils loaded with the human head," *IEEE Transactions on Biomedical Engineering*, vol. 45, no. 5, pp. 650–659, 1998.
- [11] T. S. Ibrahim, R. Lee, B. A. Baertlein, and P.-M. L. Robitaille, " B_1 field homogeneity and SAR calculations for the birdcage coil," *Physics in Medicine and Biology*, vol. 46, no. 2, pp. 609–619, 2001.
- [12] T. S. Ibrahim, R. Lee, B. A. Baertlein, Y. Yu, and P.-M. L. Robitaille, "Computational analysis of the high pass birdcage resonator: finite difference time domain simulations for high-field MRI," *Magnetic Resonance Imaging*, vol. 18, no. 7, pp. 835–843, 2000.
- [13] U. D. Nguyen, J. S. Brown, I. A. Chang, J. Krycia, and M. S. Mirotznik, "Numerical evaluation of heating of the human head due to magnetic resonance imaging," *IEEE Transactions on Biomedical Engineering*, vol. 51, no. 8, pp. 1301–1309, 2004.
- [14] C. E. Hayes, W. A. Edelstein, J. F. Schenck, O.M. Mueller, and M. Eash, "An efficient, highly homogeneous radiofrequency coil for whole-body imaging at 1.5T," *Journal of Magnetic Resonance*, vol. 63, pp. 622–628, 1985.
- [15] M. A. Stuchly and S. S. Stuchly, "Dielectric properties of biological substances—tabulated," *Journal of Microwave Power*, vol. 15, no. 1, pp. 19–26, 1980.
- [16] Y.-S. Tsuei, A. C. Cangellaris, and J. L. Prince, "Rigorous electromagnetic modeling of chip-to-package (first-level) interconnections," *IEEE Transactions on Components, Hybrids, and Manufacturing Technology*, vol. 16, no. 8, pp. 876–883, 1993.